UNIVERSITY OF BIRMINGHAM

Microwave Filters based on Advanced Manufacture Techniques Towards High-Power Applications

by

Lu Qian

A thesis submitted to the University of Birmingham for the degree of
DOCTOR OF PHILOSOPHY

School of Engineering
College of Engineering and Physical Sciences
University of Birmingham
January 2024

ABSTRACT

This PhD thesis focuses on the application of advanced manufacturing techniques in high-power microwave filters. Additive manufacturing (AM) technology and novel materials are combined to address the issue of thermally-induced frequency detuning among high-power microwave components. Several innovative resonator structures and filter topologies are proposed. The main contributions of the thesis are: (1) A narrowband 3D-printed Invar spherical dual-mode channel filter with enhanced thermal stability is demonstrated. An alternative end-to-end fabrication route for all-Invar high-power microwave components is established to overcome the complex manufacturability issues associated with Invar alloy. (2) 3D printing technology is combined with several novel materials to expand design possibilities for high-power microwave components in terms of RF, mechanical, and thermal properties. Multiphysics analysis and detailed evaluations of high-power behaviour are conducted for the designed microwave filters. (3) A 3D-printed monolithic wideband waveguide filter based on a novel pole-generating resonant iris structure is proposed. The flexibility of AM processes is leveraged to manufacture the resonant iris structure, enabling a more compact filter configuration and wider bandwidth. (4) A spherical high-Q resonator is demonstrated, for the first time, based on carbon-fibre-reinforced silicon carbide ceramic composite (HB-Cesic®). The resonator achieves a quality factor of over 10,000 at X-band, and the measured thermal stability is comparable to that of all-Invar components, while its weight is similar to common aluminum components. (5) A 3D-printed monolithic dielectric waveguide filter is presented. The lithography-based ceramic manufacturing (LCM) technique is employed to facilitate the fabrication of the monolithic dielectric filter. Compared to conventional fabrication methods, the need for special moulds is eliminated, and higher design freedom is achieved. Detailed manufacturing parameters and post-processing methods are introduced.

ACKNOWLEDGEMENT

I would like to express my deepest gratitude to my supervisor, Prof. Yi Wang, for his patient guidance, constant encouragement, and tremendous support throughout my journey towards obtaining a Ph.D. His expertise and knowledge have been invaluable to me in my research work. More importantly, Prof. Wang is a humble and approachable individual. He readily admits when he doesn't have all the answers and encourages me to explore new ideas and approaches that may challenge his own thinking. His modesty and genuine care for me make him not only an exceptional supervisor but also a role model to me. I have benefited immensely from these past four years, and it has been a great honour and privilege to be his Ph.D. student. I sincerely appreciate all the time and effort he has contributed during my Ph.D. journey.

I would also like to extend my sincerest gratitude to my former supervisor, Professor Michael Lancaster. His enlightening ideas and inspiring suggestions have been of great value to my Ph.D. research. Although Prof. Lancaster retired due to Covid-19 after supervising my first-year research, his influence on me was profound. He encouraged me to question his ideas and emphasized that good research should critically examine the pros and cons of every approach. I took his advice seriously and applied it to my subsequent research.

Working with my friends in the Emerging Device Technology research group has been a great privilege and a stroke of luck. I am grateful to them for generously sharing their thoughts and experiences, both in research activities and in life in the UK. Our Friday dinners and weekend hikes made me feel at home and enriched my research life. Their companionship made my Ph.D. journey truly worthwhile.

I would like to acknowledge the School of Engineering at the University of Birmingham for their financial support.

Finally, my heartfelt gratitude goes to my family. Their endless support has made my success possible, and their love has made my life truly meaningful.

PUBLICATIONS

Journals

1. Lu. Qian, Yi Wang, Sheng Li, Abd El-Moez A. Mohamed, Moataz M. Attallah, Talal Skaik, Paul Booth, Laurent Pambaguian, César Miquel España, and Petronilo Martín-Iglesias, "A Narrowband 3-D Printed Invar Spherical Dual-Mode Filter With High Thermal Stability for OMUXs," IEEE Trans. Microw. Theory Tech., vol. 70, no. 4, pp. 2165–2173, Apr. 2022.

2. Lu Qian, Rafael Martinez, Milan Salek, Talal Skaik, Moataz Attallah, Yi Wang, "Compact Monolithic 3D-Printed Wideband Filters Using Pole-Generating Resonant Irises," IEEE J. Microwaves, vol. PP, no. April, pp. 1–12, 2023.

3. Lu. Qian, Yeshodhara Baskaran, Matthias Krödel, César Miquel España, Laurent Pambaguian, Talal Skaik, and Yi Wang, "Lightweight, High-Q and High Temperature Stability Microwave Cavity Resonators Using Carbon-Fiber Reinforced Silicon-Carbide Ceramic Composite," IEEE J. Microwaves, no. August, pp. 1–7, 2023.

Conferences

1. Lu Qian, Sheng Li, Moataz Attallah, Talal Skaik, Paul Booth, Laurent Pambaguian, César Miquel España, Petronilo Martín-Iglesias, and Yi Wang, "Thermal Stability Analysis of 3D Printed Resonators Using Novel Materials," in 2021 51st European Microwave Conference (EuMC), 2022, no. April, pp. 334–337.

2. Lu. Qian, Rafael Martinez, Milan Salek, Talal Skaik, Moataz Attallah, Yi Wang, and Michael. J. Lancaster, "Compact Monolithic SLM 3D-Printed Filters using Pole-Generating Resonant Irises," in 2021 51st European Microwave Conference (EuMC), 2022, no. April, pp. 118–121.

3. Lu. Qian, Emelia Hayward, Milan Salek, Zhifu Liu, Jorma Vihinen, and Yi Wang, "3-D Printed Monolithic Dielectric Waveguide Filter Using LCM Technique," in 2022 IEEE MTT-S International Microwave Workshop Series on Advanced Materials and Processes for RF and THz Applications (IMWS-AMP), 2022, pp. 1–3.

4. Lu Qian, Abd El-Moez A. Mohamed, Moataz M. Attallah, Talal Skaik, Paul Booth, César Miquel España, and Yi Wang, "Multiphysics Analysis of High Power 3-D Printed Invar Spherical Dual-mode Filters," in 2023 1st Space Microwave Week, May 2023, ESA/ESTEC, Noordwijk, Netherlands.

Table of Contents

CHAPTER 1: INTRODUCTION

1.1 Background and Motivation

Microwave filters are essential passive components extensively used in various applications, such as wireless communication, sensing, and measurement systems. Their primary purpose is to manipulate signals of different frequencies by providing transmission at frequencies within the passband and attenuation in the stopband. This frequency selectivity is achieved using energy storage elements, namely resonators. Microwave resonators can broadly fall into three categories: (1) Integrated Passive Devices (IPD) comprising integrated lumped inductors and capacitors; (2) Radio Frequency Micro-Electromechanical Systems (RF MEMS) resonators, including electric field-driven or piezoelectric MEMS resonators, and (3) Distributed microwave resonators, which are based on the commensurate line element and offer distinct advantages in terms of low loss and high power-handling capability compared to IPD and RF MEMS resonators. Common distributed microwave resonator technologies include microstrip, coaxial, dielectric, and waveguide resonators. Figure 1.1 presents a comparison of these resonator technologies with respect to their power-handling capability, loss, volume, and mass.

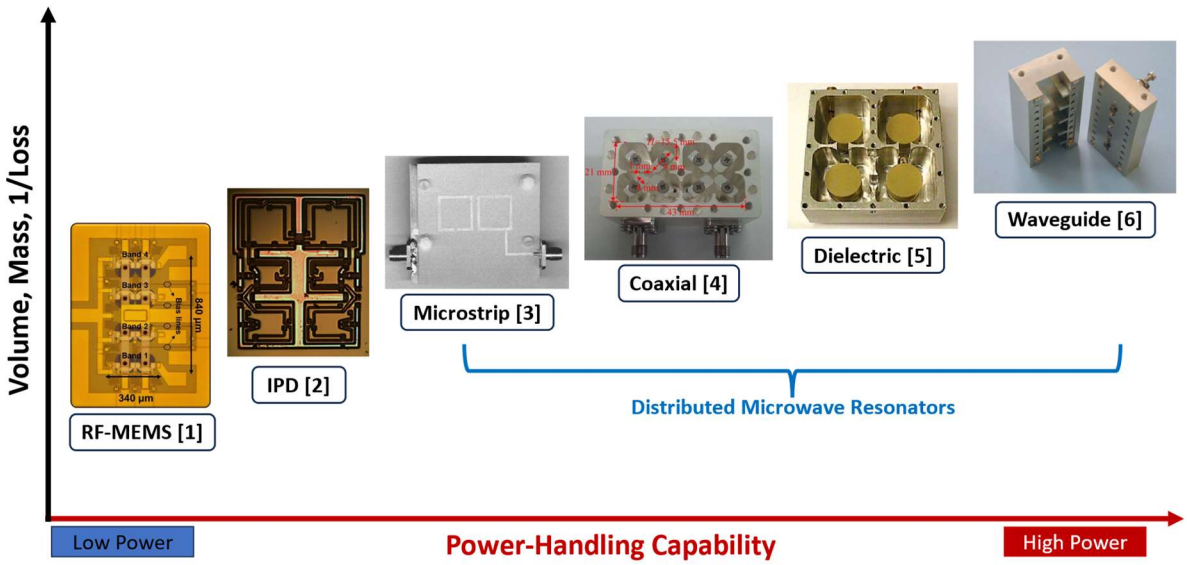

Figure 1.1 Comparison between common resonator technologies for microwave filter in terms of the power-handling capability, loss, volume and mass, with inset showing an example of each technology [1]–[6].

Satellite communication stands as one of the most prevalent application scenarios demanding high-power microwave filters. Within satellite payloads, microwave filters typically use dielectric resonators or waveguide resonators. The block diagram in Figure 1.2 illustrates a transponder, a crucial communication subsystem in many satellite payloads. In the transponder, a radio signal received by the Rx antenna undergoes initial filtering with a wideband filter (IFA - Input Filter Assembly) to eliminate out-of-band interference. The filtered signal then enters a low-noise receiver (RCVR), comprising a low-

noise amplifier (LNA) and frequency downconverter. Subsequently, the down-converted wideband signal is divided into multiple narrowband signals via an input multiplexing network (IMUX). Each channel is amplified separately by a high-power amplifier (HPA) and then combined back into a composite wideband signal using an output multiplexer (OMUX). Both the OMUX and IMUX consist of a group of narrowband channel filters. Finally, the composite wideband signal is transmitted through the Tx antennas back to the ground. Often, a common antenna is shared by a transponder, and a diplexer constructed by two wideband feed filters is utilized to separate the Rx and Tx signals. The channel power in satellite transponders typically ranges in the hundreds of watts [7]–[9], making the power handling capability a crucial consideration when designing satellite microwave filters. Their power handling capability is influenced by several factors [9]–[11]: (1) passive intermodulation (PIM) interferences, which arise from material imperfections and contact nonlinearity; (2) high-power breakdown, an electron discharge phenomenon dependent on factors like operating power, electron density and air pressure; (3) thermally-induced frequency detuning, mainly caused by power-induced self-heating and temperature variation during operation. In some high-power applications, the power handling capability of microwave components is limited by the permissible temperature rise. This underscores the importance of temperature stability in the design of high-power microwave filters.

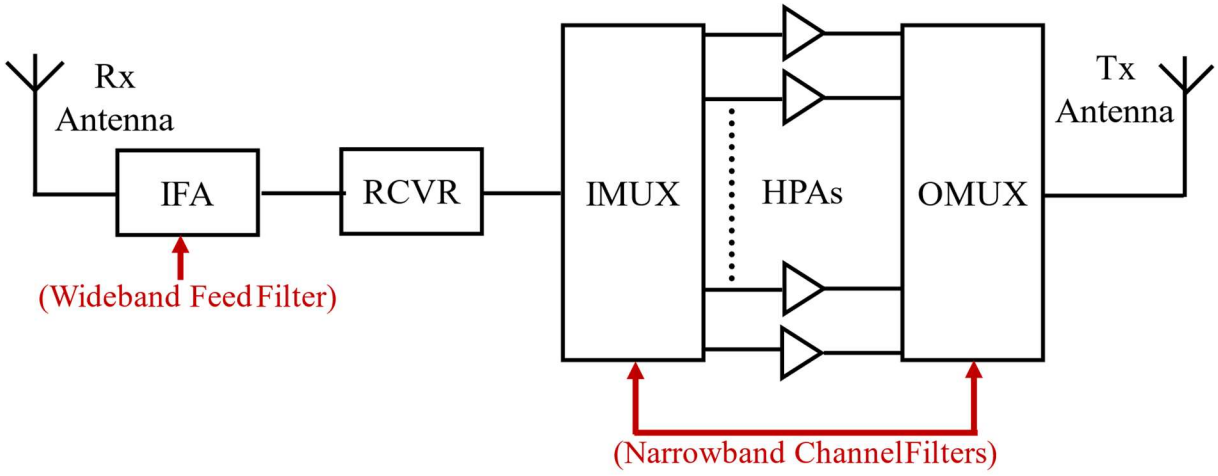

Figure 1.2 A block diagram of typical communication subsystem in satellite transponder.

In recent years, the rapid advancement of satellite communication technology, especially with the emergence of high-throughput satellite systems and satellite internet constellation systems, has led to an escalating demand for high-power microwave filters. This demand is accompanied by the need for filters with more stringent filtering characteristics, higher power-handling capability, and tighter size and weight limitations. As these requirements continue to evolve, they present significant challenges to the current satellite microwave filter solutions, both in terms of design and manufacturing. Consequently, it is imperative to evolve from the current microwave filters to meet the ever-increasing communication demands of today's world. This evolution will play a crucial role in ensuring efficient and reliable satellite communication systems for the future.

Additive manufacturing (AM), commonly referred to as 3-D printing, is an emerging advanced manufacturing technology that is revolutionizing various industry sectors and research communities [12].

In recent times, 3-D printing has also unlocked new possibilities for microwave components. This technology enables rapid prototyping of novel design concepts, reducing lead time and costs. It offers superior flexibility to create intricate geometric structures, thus enhancing design freedom. Numerous 3-D printed microwave devices have been reported in recent years [13]–[15]. However, it is important to note that the majority of these previously demonstrated microwave filters were not specifically designed for real-world high-power operations. As a result, there is a significant need to further explore and develop 3-D printed microwave filters that can meet the stringent demands of practical high-power applications.

1.2 Novelty and Contributions of the Thesis

The aim of this thesis is to address the current challenges in the design and implementation of high-power microwave filters through advanced manufacturing techniques, primarily involving AM technology and novel low coefficient-of-thermal-expansion (CTE) materials. The focus will be on tackling the thermal-induced frequency detuning issue and designing innovative filter structures and topologies.

The specific novelty and contributions of this research work are as follows:

(1) AM technology has been utilised to overcome the complex manufacturability issues associated with Invar alloys. The new alternative end-to-end fabrication route for all-Invar high-power microwave components have been established. A narrowband 3D printed Invar spherical dual-mode channel filter with enhanced thermal stability has been demonstrated and published in IEEE Transactions on Microwave Theory and Techniques.

(2) 3D printing technology has been combined with novel alloy materials to create new opportunities for temperature compensation mechanisms. End-to-end fabrication solutions based on several alloy materials have been investigated, opening design possibilities for comprehensive improvements in RF, mechanical, and thermal properties of high-power microwave components. This research has been published in the 51st European Microwave conference and is being extended for submission to an IEEE Journal.

(3) The application of a low CTE non-metallic material - carbon-fibre reinforced silicon carbide ceramic composite (HB-Cesic®) - in high-power microwave components have been demonstrated for the first time in a high-Q resonator. This research has been published in IEEE Journal of Microwaves.

(4) A pole-generating resonant iris structure has been proposed and implemented in monolithically printed wideband waveguide filters, by exploiting the manufacturing flexibility of AM processes. This design offers a more compact filter structure and wider bandwidth. The findings of this work have been published in the 51st European Microwave conference and IEEE Journal of Microwaves.

(5) By harnessing the advantages of ceramic 3D printing technology in manufacturing complex monolithic geometries, a 3D printed monolithic dielectric waveguide filter has been presented. The findings of this work have been published in the 2022 IEEE MTT-S International Microwave Workshop Series on Advanced Materials and Processes for RF and THz Applications.

1.3 Outline of the Thesis

The thesis is presented as a series of published and publishable papers following the University's Alternative Format Thesis guidelines. The thesis comprises nine chapters, organized as follows:

Chapter 1: This chapter serves as an introduction to the research, providing the background and motivation for the study. It outlines the main contributions and an overview of the thesis structure.

Chapter 2: A comprehensive literature review related to this thesis is presented in this chapter. It covers microwave filters for satellite communication systems, practical considerations involved in designing high-power microwave filters, AM technology, and 3D printed microwave components.

Chapter 3: A 3-D printed narrowband bandpass filter based on spherical dual-mode resonators is presented. It is designed for output multiplexers (OMUXs) using high-Q spherical dual-mode resonators. The realization is by laser powder bed fusion (L-PBF) technology of Invar alloy, chosen for its low coefficient of thermal expansion (CTE). Using L-PBF circumvents Invar's manufacturability issues. To demonstrate the proposed solution, detailed thermal-RF test at different temperatures was carried out. The experimental results of a fourth-order silver-plated Invar filter with two transmission zeros verify the design and manufacturing.

Chapter 4: This chapter presents the measurement results of the Invar spherical filter introduced in Chapter 3 after further post-processing. It also investigates the effect of different surface treatment techniques such as the mechanical polishing method based on vibratory grinding and the electrochemical Hirtisation® process. The thermal stability of the filter during high-power operation is modelled through Multiphysics simulation. The power breakdown threshold is analysed using SPARK3D, showing that the Invar filter has a sufficient margin against the specified power requirements.

Chapter 5: This chapter presents the investigation into the thermal stability of microwave cavity resonators using several novel alloy materials. Shaped spherical resonators are additively manufactured by L-PBF technology from alloy powders. The end-to-end manufacture method of each sample is presented, and their thermal stability is experimentally characterized by thermal-RF measurement. A detailed comparison between different samples in terms of their mechanical, thermal and RF performance is presented. This work introduces an expanded range of materials that may be used for microwave filters and opens opportunity for new temperature compensation techniques for high power filters.

Chapter 6: This chapter presents a high-Q spherical resonator manufactured using carbon-fiber reinforced silicon carbide (SiC) ceramic composite material HB-Cesic®. Compared to the common conventional Invar alloy, the SiC composite has attractive properties of low coefficient of thermal expansion, low density, and high thermal conductivity as well as its flexibility in manufacturing. Two resonators, one monolithic version and other one based on split-block structure, have been experimented. The detailed comparison between the measured RF performances and simulated analysis are presented to evaluate the novel material and manufacturing technology. The thermal-handling capability is experimentally characterized through the thermal-RF test at different temperatures. The measured high thermal stability correlates very well with the prediction. This work establishes the feasibility of using HB-Cesic SiC in microwave resonators and paves the way for further development and verification program for more complex passive microwave devices such as filters and multiplexers for space applications.

Chapter 7: This chapter presents a new pole-generating resonant iris structure for the design of iris-coupled cavity filters. Different from conventional reactive iris, the resonant iris can generate an extra transmission pole without increasing the number of resonant cavities. As a result, several design

advantages can be gained: (i) a more compact filter structure; (ii) an ability to realize strong coupling and therefore wide bandwidth; and (iii) a new polarization rotation capability. Two third-order Chebyshev filters are designed and implemented, demonstrating the miniaturization and polarization rotation feature. A fifth-order Chebyshev filter with 20% fractional bandwidth is presented to show the capability of realizing wideband. This also demonstrates the realization of asymmetric coupling between the resonant iris and the cavity resonator on either side. An approach to control and extract the coupling between the iris and the cavity resonator has been presented. To manufacture the intricate asymmetric iris structure, all the presented filters are printed monolithically using L-PBF technology. Excellent agreement between the measurements and simulations has been achieved, verifying the design concept as well we the additive manufacturing capability.

Chapter 8: This chapter presents a 3-D printed monolithic dielectric waveguide filter. The proposed filter is constructed by a single piece of 3D printed dielectric puck with silver plated outer surface. A lithography-based ceramic 3-D printing technology is employed. In this way, the mould required in conventional ceramic forming technologies is eliminated and higher design freedom can be obtained. The detailed manufacturing parameters and post-processing methods are described. A prototype filter operating at 11.5 GHz with 850 MHz bandwidth is designed, fabricated, and measured. The measurement result shows reasonable agreement with the simulation.

Chapter 9: This chapter serves as the conclusion of the thesis, summarizing the key findings and contributions. It also outlines the limitations of the research and potential directions for future work.

Reference

[1] S. Nam, M. Z. Koohi, W. Peng, and A. Mortazawi, "A Switchless Quad Band Filter Bank Based on Ferroelectric BST FBARs," *IEEE Microw. Wirel. Components Lett.*, vol. 31, no. 6, pp. 662–665, 2021.

[2] C. C. Huang, W. T. Fang, and Y. S. Lin, "Miniaturized wideband bandpass filter in IPD technology with passive equalizer to improve the flatness of insertion loss response," *2017 IEEE CPMT Symp. Japan, ICSJ 2017*, vol. 2017-January, pp. 75–78, 2017.

[3] J. S. Hong and M. J. Lancaster, "Aperture-coupled microstrip open-loop resonators and their applications to the design of novel microstrip bandpass filters," *IEEE Trans. Microw. Theory Tech.*, vol. 47, no. 9 PART 2, pp. 1848–1855, 1999.

[4] X. Wang, G. Jang, B. Lee, and N. Park, "Compact quad-mode bandpass filter using modified coaxial cavity resonator with improved Q-factor," *IEEE Trans. Microw. Theory Tech.*, vol. 63, no. 3, pp. 965–975, 2015.

[5] R. R. Mansour, "Filter technologies for wireless base stations," *IEEE Microwave Magazine*, vol. 5, no. 1. pp. 68–74, Mar-2004.

[6] V. E. Boria and B. Gimeno, "Waveguide filters for satellites," *IEEE Microw. Mag.*, vol. 8, no. 5, pp. 60–70, 2007.

[7] F. De Paolis and C. Ernst, "Challenges in the design of next generation ka-band OMUX for space applications," *31st AIAA Int. Commun. Satell. Syst. Conf. ICSSC 2013*, no. October 2013, pp. 1–7, 2013.

[8] B. Yassini and M. Yu, "Ka-Band Dual-Mode Super Q Filters and Multiplexers," *IEEE Trans. Microw. Theory Tech.*, vol. 63, no. 10, pp. 3391–3397, Oct. 2015.

[9] V. Singh, P. K. Ambati, S. Soni, and K. Karthik, “Enhancing Satellite Communications: Temperature-Compensated Filters and Their Application in Satellite Technology,” *IEEE Microw. Mag.*, vol. 20, no. 3, pp. 46–63, 2019.
[10] M. Yu, “Power-handling capability for RF filters,” *IEEE Microw. Mag.*, vol. 8, no. 5, pp. 88–97, 2007.
[11] I. Arregui *et al.*, “High-Power Filter Design in Waveguide Technology: Future Generation of Waveguide Satellite Filters in Payloads Handling Increasing Bit Rates and Numbers of Channels,” *IEEE Microw. Mag.*, vol. 21, no. 6, pp. 46–57, 2020.
[12] I. Gibson, D. Rosen, and B. Stucker, *Additive Manufacturing Technologies: 3D Printing, Rapid Prototyping, and Direct Digital Manufacturing*. Springer New York, 2016.
[13] R. Sorrentino, P. Martin-Iglesias, O. A. Peverini, and T. M. Weller, “Additive Manufacturing of Radio-Frequency Components [Scanning the Issue],” *Proc. IEEE*, vol. 105, no. 4, pp. 589–592, 2017.
[14] R. Sorrentino and O. A. Peverini, “Additive manufacturing: A key enabling technology for next-generation microwave and millimeter-wave systems [point of view],” *Proc. IEEE*, vol. 104, no. 7, pp. 1362–1366, 2016.
[15] C. Tomassoni, O. A. Peverini, G. Venanzoni, G. Addamo, F. Paonessa, and G. Virone, “3D Printing of Microwave and Millimeter-Wave Filters: Additive Manufacturing Technologies Applied in the Development of High-Performance Filters with Novel Topologies,” *IEEE Microw. Mag.*, vol. 21, no. 6, pp. 24–45, Jun. 2020.

CHAPTER 2: LITERATURE REVIEW

This chapter surveys the relevant literature pertaining to the research topics investigated in this thesis. Section 2.1 presents an overview of microwave filters used in satellite payloads. Section 2.2 introduces practical considerations involved in the design of the high-power microwave filters. Section 2.3 reviews additive manufacturing techniques and their application in the development of 3-D printed microwave filters. Section 2.4 discusses the current state-of-the-art in these research field and highlights the motivation behind this PhD project.

2.1 Microwave Filter Networks for Satellite Payload

As illustrated in Figure. 1.2, the microwave filter networks employed in satellite payloads can be broadly categorized into two types: wideband feed filters and narrowband channel filters. Wideband feed filters are utilized as antenna feed filters or in feed diplexers to isolate the RX signal and TX signal from a shared antenna. On the other hand, narrowband channel filters are used in input or output multiplexers to separate different channels within the system.

2.1.1 Wideband Feed Filters

Wideband feed filters in satellite payloads are typically positioned next to the antenna and serve the purpose of allowing only the RX (up-link) or TX (down-link) band signals to pass through, while attenuating other signals outside this frequency range [1], [2]. These wideband filters typically have a bandwidth of 250 MHz or 500 MHz, which correspond to the total bandwidth of the multiple channel filters present in the satellite transponder.

Among the wideband filters, the most employed is the rectangular waveguide filter based on the TE_{10N} mode resonator. Figure. 2.1 shows a photograph of some representative TE_{10N} mode waveguide filters and diplexers. Traditionally, the feed diplexer consists of inductively coupled TE_{101} mode filters and a waveguide junction [1], [2]. With the development of the satellite communication system, these in-line TE_{101} mode filters, with Chebyshev response, fail to meet the increasingly stringent requirement. To enhance out-of-band rejection, quasi-elliptic microwave filters with extra transmission zeros were used. The cross-coupling technique is the most widely used method to generate transmission zeros [3]. For cross-coupled TE_{101} mode waveguide filters, both the capacitive and inductive irises are usually needed to realize the special coupling topology [4]. To achieve more compact configuration, dual-mode square cavity filter using a pair of orthogonal degenerate TE_{101}modes was reported [1]. Another common transmission zero generating approach is the extracted-pole technique [5]. In [6], a TE_{101} mode extracted-pole filter was presented, where a low-cost H-plane waveguide configuration was proposed to implement the zero-pole pair generating element. In addition to the fundamental TE_{101} resonance mode, a few rectangular waveguide filters based on higher-order TE_{10N} modes have also been proposed [7]–[12]. By utilizing these higher-order modes, negative cross-coupling can be achieved solely through inductive irises, simplifying the fabrication process. Furthermore, a novel type of TE_{101} mode filter utilizing the interaction of multi-path signals within a single resonator has recently been presented [13], [14]. The phase shift can be generated by two different signal paths within the same resonator, resulting in an additional transmission zero without the need for the cross coupling.

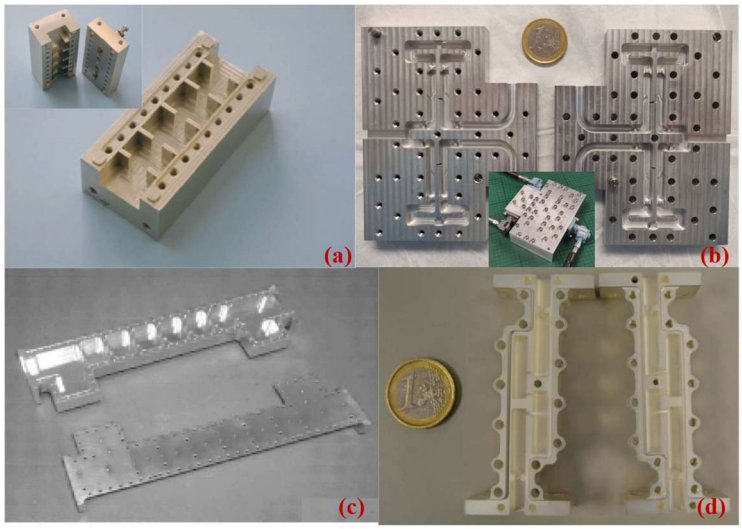

Figure 2.1 Wideband feed filter and diplexer based on TE_{10N} resonance mode. (a) Inductively coupled inline TE_{101} mode rectangular waveguide filter with Chebyshev response [1]. (b) Rectangular waveguide diplexers based on cross-coupled TE_{103} mode resonator filter [12]. (c) H-plane extracted-pole rectangular waveguide filter [6]. (d) Quasi-elliptical rectangular waveguide filter implemented through multiple-path signal interference approach [13].

Rectangular waveguide resonators operating in the TM modes are also commonly used in wideband feed filters. Compared to TE mode resonator filters, TM mode filters offer a more compact configuration. The common TM mode resonators include TM_{110} single-mode resonators and $TM_{120/210}$ dual-mode resonators. Figure. 2.2 shows several representative TM mode resonators filters [15]–[17]. Another notable feature of TM mode resonator filters is that the quasi-elliptic response can be readily achieved in the in-line configuration. These filters utilize non-resonating modes within the resonator to create additional paths for power flow between non-adjacent resonators, thereby generating transmission zeros. In [15], the concept of bypass coupling using the non-resonant $TE_{10/01}$ mode was introduced in an in-line TM_{110} mode filter to realize the pseudo-elliptic response. The idea was extended to TM dual-mode filters [16], [18]–[20], where the TM_{110} mode serves as the non-resonating mode. However, a major limitation of TM mode filters is their narrow spurious-free band compared to TE mode filters. To address this limitation, one approach is to replace the single coupling iris with multiple coupling irises [21]. Another approach is to cascade with a comb-line resonator filter as used in [17], [22].

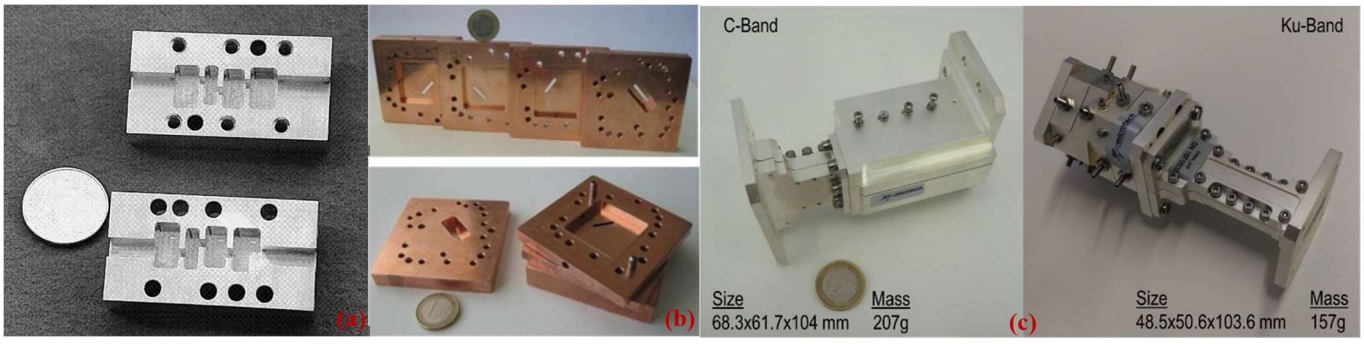

Figure 2.2 Wideband feed filters based on TM resonance mode. (a) Inline TM_{110} mode waveguide filter utilizing bypass couplings of non-resonating $TE_{10/01}$ modes [15]. (b) Waveguide $TM_{120/210}$ dual-mode filter with non-resonating TM11 mode [16]. (c) C-/Ku-band filter with TM dual-mode section cascaded comb-line section [17].

2.1.2 Narrowband Channel Filters

For narrowband channel filters, Table 2.1 provides some typical bandwidths and channel separations used in satellite transponders. The relatively narrow bandwidth requires high Q_u values to achieve low insertion loss, while the small guard band between channels poses a tough challenge to achieving very stringent out-of-band rejection. In practical applications, these narrowband filters are designed to have a quasi-elliptic response using high-Q cavity resonators. Common high-Q cavity resonators are the TE_{11N} (N = 1 - 5) cylinder resonator [23] and TE_{011} mode cylinder resonators. To meet the growing power requirements, a super-Q dual-mode resonator based on the TE_{221} cylinder cavity was proposed as well [24], [25].

Table 2.1 Typical Channel Bandwidth and Separations for C- to Ku-Band Satellite Transponder

Channel Bandwidth (MHz)	24	36	54	72
Channel Separation (MHz)	27	40	61	80

The TE_{11N} resonator filters typically operate in dual mode, where two orthogonal degenerate TE_{11N} modes are excited within a single cylinder resonator. Compared to single-mode resonators, dual-mode resonators offer a significant reduction in footprint, and the orthogonal modes provide flexibility in generating transmission zeros. Figure. 2.3 shows several TE_{11N} dual-mode filters. Depending on the position of the feeding port, TE_{11N} dual-mode filters can be classified into two different configurations: end-coupled [23] or side-coupled [26]. In [23], the end-coupled configuration was first proposed, and a channel filter based on the TE_{111} dual-mode resonator with a 24 MHz bandwidth was designed. In [27], a 14-channel output multiplexer with an end-coupled TE_{111} mode filter was presented, where each channel filter was realized using a combination of dual-mode and single-mode cavities. In [28], a C-band waveguide multiplexer based on dual-mode TE_{111} filters was demonstrated. This work employed three cavities for each channel filter, resulting in a six-order Chebyshev filtering characteristic. To further reduce insertion loss, an end-coupled dual-mode quasi-elliptic filter utilizing the higher-order TE_{113} resonance mode was shown in [29]. For the side-coupled configuration, the feeding ports are moved to the side wall, allowing for further reduction in filter length and the placement of additional tuneable structures at the end walls. An output multiplexer based on a side-coupled TE_{113} dual-mode filter was reported in [30]. A probe-excited TE_{111} mode filter with a side-coupled configuration was described in [31]. To mitigate the adverse impact of tuning and coupling elements, a narrowband filter based on an elliptical cavity (TE_{111} mode) resonator was presented in [32]. To suppress spurious modes in the TE_{11N} resonator, a stepped cylinder resonator was proposed for wideband OMUX applications [33].

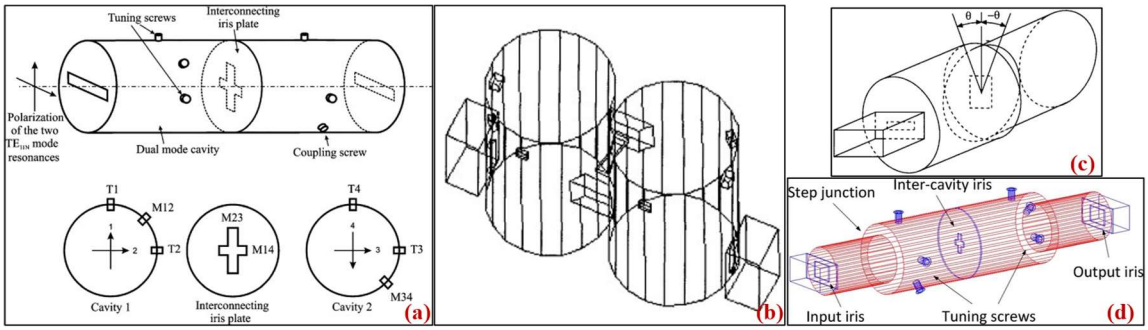

Figure 2.3 Narrowband channel filters based on TE_{11N} resonance mode. (a) End-coupled TE_{111} dual-mode circular waveguide filter [29]. (b) Side-coupled TE_{111} dual-mode circular waveguide filter [26]. (c) TE_{11N} dual-mode channel filter based on elliptical cavity resonator [32]. (d) TE_{11N} dual-mode channel filter based on stepped circular waveguide resonator [33].

The narrow-band channel filters based on TE_{011} mode cylinder resonators have also been extensively reported [34]–[36]. Compared to TE_{11N} mode resonators, the main advantage of TE_{011} mode resonators is their even higher unloaded quality factor, which can exceed 20000 in Ku band [36]. However, the single-mode operation of TE_{011} resonators also presents challenges in terms of filter footprint and the generation for transmission zeros. In the early designs [34], [35], TE_{011} filters were mainly constructed from direct-coupled resonators, where transmission zeros were introduced through cross coupling. Figure. 2.4(a) shows the configuration of such classical TE_{011} mode filters. The main challenges here are to suppress the degenerate TM_{111} mode and implement negative cross coupling. In [37]–[39], the standard TE_{011} mode cavity was modified to separate the TM_{111} mode, and several novel approaches to generate negative cross coupling were reported. In practical engineering designs, TE_{011} resonators are usually coupled through two sidewall coupling apertures arranged at 90° angular offset with each other to suppress the degenerate spurious modes. For the ease of fabrication, extracted-pole technique was often used to achieve quasi-elliptic filter responses. Different from the cross-coupling method, this technique generates a zero-pole pair using modular pole-generating elements with uniform coupling signs. Early work on TE_{011} mode extracted pole filters and multiplexers was reported in [40], [41]. Recently, a few novel synthesis techniques have been proposed for these kinds of filters [42], [43]. Figure. 2.4(b) and (c) shows several novel configurations of extracted pole TE_{011} mode narrowband channel filters. Additionally, the increasing demand for higher power capacity drives the development of resonators with even higher Q_u values. In [24], [25], a super-Q cylinder cavity resonator with a Q_u of over 30000 at 20 GHz was proposed, and a K-band 14-channel output multiplexer based on this resonator was demonstrated.

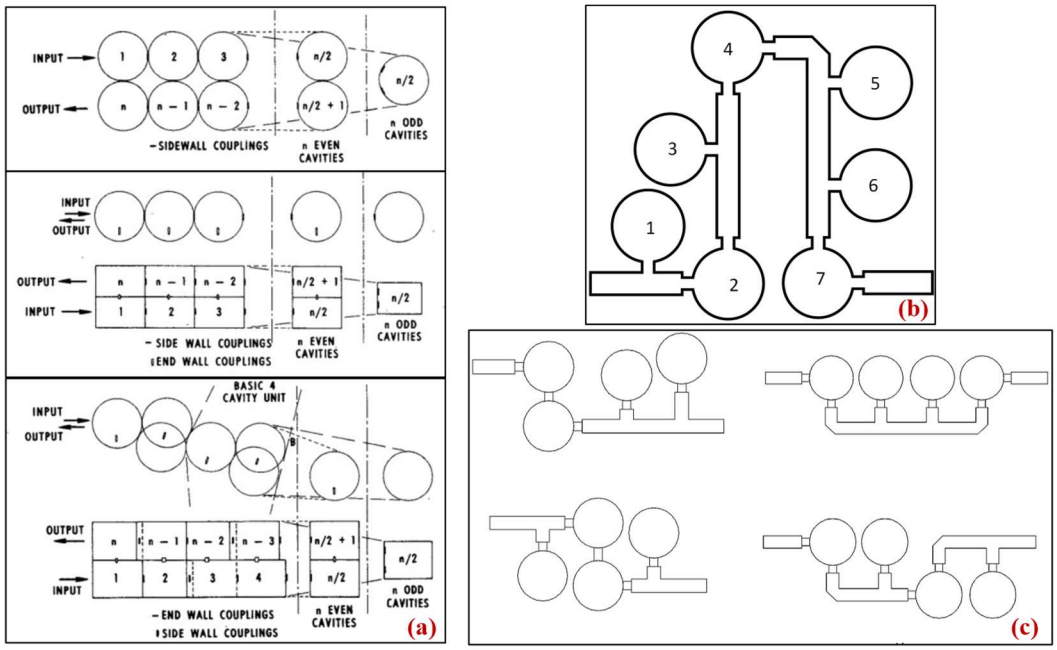

Figure 2.4 Narrowband channel filter based on TE_{011} mode cylinder resonator. (a) Direct-coupled TE_{011} mode filters [35]. (b) and (c) Extracted pole TE_{011} mode filter [42], [43].

2.2 Practical Considerations for High-power Filter Networks

In addition to the RF performance, several practical factors must be carefully considered in designing high-power filter networks [44]–[48]. These factors include:

(1) Passive Intermodulation (PIM) Interferences: PIM is a phenomenon that generates undesired intermodulation products in passive devices. In high-power applications, PIM can significantly degrade the overall system performance. Therefore, it is essential to minimize PIM effects during the design process.

(2) High-Power Breakdown: High-power signals can cause breakdown in microwave components, leading to device failure and performance degradation. Designing filters that can handle high-power levels without experiencing breakdown is crucial for reliable operation.

(3) Thermal-induced Frequency Detuning: High-power operation can lead to temperature increases in the filter components, which may cause frequency detuning due to thermal expansion of the cavity resonators. This detuning can affect the filter's performance and stability. Therefore, managing thermal effects is essential to ensure consistent and reliable filter performance.

This section will provide a brief review of each of these factors and their impact on the design of high-power filter networks, with a particular focus on thermal-related issues. This is because, in many practical applications, the power handling capability of microwave components is determined by the permissible temperature rise of the equipment rather than the limitation imposed by microwave breakdown [44], [47].

2.2.1 Passive Intermodulation Interferences

Intermodulation is a widespread phenomenon in active devices due to their intrinsic nonlinearity. However, even passive components such as filters and multiplexers exhibit a certain degree of nonlinear behaviour and can generate intermodulation products, known as passive intermodulation (PIM). Although PIM products are typically at a low level, they can still cause severe interference to the communication system, particularly in high-power operation [49]–[52]. In satellite communication systems, a common antenna is often used for the RF transponder, allowing for coupling between the transmit and receive sections. Additionally, there can be a significant difference in power levels between the transmission and reception in a satellite transponder, sometimes reaching 130–140 dB. Consequently, the level of PIM should be suppressed by at least 160 dB below the power level of the transmission signal to avoid interference with the receive channel. Due to the complex physical principles underlying the PIM phenomenon, a complete theory for PIM has not yet been fully developed. In general, PIM primarily originates from material nonlinearity and contact nonlinearity. The former usually stems from thin oxide layers on metal surfaces, microcracks or voids in metal structures, and residual metal particles on surfaces. The latter arises from mechanical imperfections in interfaces and joints. The practical PIM is the combination of all these effects.

In practical design, guidelines can be followed to mitigate PIM products [50], [52]:

(1) Using metals with low levels of PIM (such as gold, silver, copper, and brass) rather than aluminium and steel.

(2) Avoiding structures that can lead to current density concentration (e.g., sharp edges).

(3) Minimizing or eliminating mechanical connections and tuning screws.

(4) Avoiding the use of ferromagnetic and dielectric materials in high-power components.

(5) Paying particular attention to electroplated surfaces and avoiding nickel plating.

It should be noted that PIM reduction can only be achieved experimentally.

2.2.2 High-Power Breakdown

Filters and multiplexers based on high-Q resonators are particularly susceptible to high-power breakdown due to their compact structures, field enhancement at discontinuities, and sharp rejection outside the intended passband. The common types of high-power breakdown within microwave filter networks are ionization breakdown and multipaction breakdown.

Ionization breakdown is a phenomenon where the insulating gas in a microwave system turns into conducting plasma due to the high electric field. This leads to an exponential increase in electron concentration and eventually results in ionization breakdown. On the other hand, multipaction breakdown is a secondary electron resonance phenomenon that occurs under vacuum or low-pressure conditions when the gap within a cavity filter is smaller than the mean free path of electrons. When conditions are met regarding frequency and intensity of the applied electrical field, free electrons bombard the nearby conducting walls, leading to continuous release of secondary electrons and eventual multipaction breakdown. Understanding the operational mechanisms behind these two high-power breakdown phenomena requires multidisciplinary knowledge encompassing various fields of physics and engineering, such as electrodynamics, kinetics, and statistical mechanics [52]–[64]. The complexity is further increased in the case of multipaction breakdown due to the increasing number of RF carriers and complex modulation schemes [65]–[69]. Comprehensive investigation of these aspects is beyond the scope of this PhD project. In this section, a concise overview of the analysis methods will be presented, followed by a discussion on practical considerations in high-power microwave breakdown, including design margins and prevention methods.

2.2.2.1 Analyse Method

(1) Analytical Method:

The classical methods for analysing high-power breakdown, including both ionization and multipaction breakdown, are well-established[46], [64]. The analysis procedure mainly involves the following steps: (1) Evaluating the breakdown threshold; (2) Obtaining the internal electrical field strength or voltage value; (3) Determining the design margin. However, the evolution of satellite communication technology – characterized by an increasing number of carriers, more complex modulation schemes, and novel microwave component configurations – poses significant challenges to conventional analytical methods. These methods often fail to provide accurate predictions of high-power breakdown phenomena.

(2) Numerical Method:

The advancement of numerical methods has made it possible to model and analyse high-power breakdown phenomena, even in combination with full-wave electromagnetic solvers, entirely numerically. One of the most well-known methods is the particle-in-cell (PIC) codes [70], which simultaneously solve the motion of particles and field equations in two different spaces. These two spaces are connected through particle-to-grid or grid-to-particle interpolation methods. PIC codes have been successfully integrated into commercial electromagnetic simulation software, such as CST Particle Studio, SPARK3D®, and FEST3D®. Compared to conventional analytical methods, these integrated tools offer enhanced prediction accuracy for arbitrary structures and are applicable to nonhomogeneous fields and different numbers of carriers and modulations. In [71]–[73], a comparative investigation of both analytical and numerical methods was conducted using practical microwave filter cases. The results showed that numerical methods achieved better agreement with experimental data than conventional analytical techniques.

2.2.2.2 Design Margin

Ideally, a higher design margin is preferred to ensure greater safety and reliability. However, the practical design margin is a sensitive issue for both customers and suppliers due to various influencing factors, such as manufacturing technology, tolerances, contamination, environmental conditions, and test setup.

Currently, two main standards for satellite high-power microwave system are adopted: one by the European Space Agency [52] and the other by Aerospace Corporation [69]. In both standards, the design margin is defined based on the following factors: (1) Type of component: Microwave components are classified according to their materials and topologies. (2) Stage of design or test: Different design margins are applied

at different phases of the design or during the test campaign. (3) Type of signal: Different margins are considered for single-carrier or multi-carrier operation.

For individual high-power microwave components, such as filters, both standards suggest a 3-dB margin for the test campaign. If an analysis demonstrates a 6-dB margin, it could avoid costly measurement verification campaigns, as testing at such high-power levels and frequencies is complex and very expensive. For multi-carrier operation, the margin becomes more complex. Assuming the input power for the components operating with N carriers is P_{in}, the peak power threshold complying with the 3-dB margin should be ($2N^2 \cdot P_{in}$). However, such high power-handling specifications are rarely required in practical designs as they represent worst-case scenarios for multi-carrier operation and are beyond the range of most common high-power measurement setups.

2.2.2.3 Prevention of Breakdown

Preventing high-power breakdown is of utmost importance to ensure the reliable and safe operation of microwave components. As discussed in previous sections, various factors influence the occurrence of breakdown phenomena. For ionization breakdown, one effective mitigating method is to employ a pressurized system. By filling the microwave system with electronegative gases, the mean free path of free electrons can be reduced, leading to an improvement in breakdown field strength. Additionally, using gases with higher attachment coefficients can further enhance the breakdown field strength. For multipaction breakdown, modifying the mean free path is also a common approach to prevent the phenomenon. Adjusting the gap size between the resonator walls can influence the mean free path of electrons and potentially reduce multipaction. Furthermore, avoiding the resonance conditions and reducing the secondary emission yield are other effective methods to prevent multipaction.

Table 2.2 summarises the characteristics and advantages of common prevention methods for high-power breakdown.

Table 2.2 High-power Breakdown Prevention Methods

Ionization Breakdown		
Method	Prevention Mechanism	Advantage & Disadvantage
Pressurized System	Reduce the mean free path of electrons	1. Ready to apply 2. Decreased reliability 3. A source of potential PIM
Filling Electronegative Gases	Increase the attachment coefficient to localize the gas discharge	1. Effective increase the breakdown threshold 2. Electronegative gases (such as freon) are usually toxic and are not applicable to commercial systems.
Multipaction Breakdown		
Method	Prevention Mechanism	Advantage & Disadvantage
Pressurized System	Reduce the mean free path of electrons	1. Simple to apply 2. Decreased reliability 3. A source of potential PIM
Dielectric Filling	Reduce the mean free path of electrons	1. Simple in theory and in implementation 2. Low cost 3. Lowers the effective Q_u. 4. Not applicable above 12 GHz
Large Gap Size	Violate the resonance condition and hence improve the breakdown voltage threshold.	1. Simple to implement 2. Limitation on achievable RF performance
DC or Magnetic Bias	Altering the electron resonance condition to allow the higher breakdown threshold	1) Prevent discharge across the gap 2) Possible wideband noise because of the surface erosion 3) Limited improvement in power handling margin
Reduce Surface Potential	Reduce the secondary emission ratio of surface through the special coating layer	1) Simple to implementation 2) Higher power loss due to the deceased effective electrical conductivity

2.2.3 Thermal-Induced Frequency Detuning

In practical applications, thermal stability is also a crucial consideration for high-power microwave components. When exposed to high RF power, these components experience ohmic loss, leading to the generation of a significant amount of heat, or self-heating. This heat can cause local hot spots and an overall temperature rise within the component.

Due to the thermal expansion of materials, the geometric dimensions of microwave resonators change with varying temperatures. Since the resonance frequency of a microwave cavity resonator is influenced by its geometric dimensions, its RF performance will exhibit a certain degree of temperature dependence. For microwave filters, a particularly noticeable effect of temperature variation is the frequency detuning. As the temperature changes, the resonance frequency of the filter can shift, affecting its performance. This frequency detuning is especially critical for narrow band filters, where the narrower bandwidth implies relatively high losses and less margin for frequency shift.

To minimize the power dissipation (and therefore self-heating), high-Q resonators are usually used in microwave filters. However, achieving a higher Q value often requires larger cavity sizes and/or higher-order resonance modes. This can lead to an increase in the volume of the filter. The higher-order resonance modes can introduce more nearby spurious modes. These factors need to be carefully considered in the design of high-Q microwave filters to balance the benefits of higher Q values with the potential drawbacks. In addition to the heating effect caused by power dissipation, variations in environmental temperature also pose significant challenges to the temperature stability of microwave components. This is particularly so for those used in space applications. For satellite payloads, the channel filters and feed filters typically operate in temperature ranges of −15 to +85 °C and −135 to +160 °C, respectively.

Therefore, considering the impact of temperature on the performance is essential in high power filter design. Mitigating frequency detuning and maintaining thermal stability are crucial for the efficient and effective operation of microwave components in the space applications.

2.2.3.1 Coefficient of Thermal Expansion (CTE) and Effective Temperature Coefficient (ETC)

Coefficient of thermal expansion (CTE), α, quantifies the fractional change in length (or volume) of a material for a unit change in temperature. The CTE is usually expressed in the unit of micrometres per meter per degree Celsius (μm/m·°C) or parts per million per degree Kelvin (ppm/K). For small temperature changes, the thermal expansion or contraction of uniform linear objects can be approximated by the formula:

$$\alpha = \frac{(l_1 - l_0)}{l_0 \cdot (T_1 - T_0)} \tag{3.2}$$

where l_0 is the original length of the material at temperature T_0, and l_1 is the length of the material at the final temperature T_1.

Figure 2.5 shows the thermal-induced frequency detuning for a bandpass filter, where the passband is shifted down with rising temperature and up with decreasing temperature. A common way to describe the frequency shift Δf against the temperature variation ΔT is through the parameter $\Delta f/\Delta T$, which is typically measured in Hz/K. To establish a correlation between the frequency shift and the Coefficient of Thermal Expansion (CTE), we define the "effective temperature coefficient" (ETC) of the resonator or filter as:

$$ETC = \frac{(\Delta f / f_0)}{\Delta T} \tag{3.3}$$

where f_0 represents the centre frequency. The ETC of the device has the unit of 10-6×Hz/Hz/K or ppm/K. It is directly comparable with CTE of the material. As a first order approximation, $\Delta f / f_0 \approx$ - CTE × ΔT.

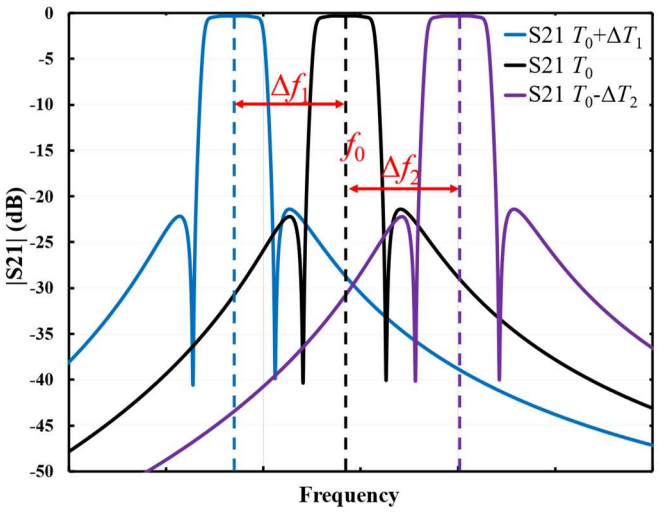

Figure 2.5 Frequency detuning induced by temperature variation.

2.2.3.2 Temperature Compensation Technology

To address the issue of thermal-induced frequency detuning, various temperature-stable filters and multiplexers have been developed [45], [47], [74]–[76]. There are two approaches: 1) Use of low CTE materials; 2) Temperature compensation structures.

1) Use of Low CTE Materials

To reduce the frequency detuning caused by temperature variation, the most intuitive method is to construct filters using low CTE materials, such as Invar-36 alloy. Invar is an iron-nickel alloy with exceptionally high dimensional stability under temperature variation, with a CTE in the range of 0.5 to 2 ppm/K, depending on the alloy composition. Compared to common aluminium alloy (Al6061) with a CTE of around 23 ppm/K, Invar alloy can achieve a reduction of around 90% in temperature shift. Many Invar-based microwave components have been reported in the past [25], [45], [77]–[79], as shown in Figure 2.6. Initially, Invar filters were constructed using standard 1.6 mm thick walls and standard flanges [45]. However, Invar has very high density (8.1 g/cm^3), three times that of Al6061 (2.7 g/cm^3). To reduce the mass of Invar filters, the wall thickness of some Invar components was reduced to 0.8 mm. While thinner walls make the components lighter, the hardness of Invar results in very poor manufacturability, leading to work hardening and part warping during the machining process. Additionally, thin Invar parts are prone to breakage, making the construction using Invar difficult and expensive. In addition to the manufacturability difficulty, Invar's intrinsic low thermal conductivity is another design concern. To ensure efficient heat transfer and avoid over-heating, additional temperature control mechanisms had to be introduced [77]–[79]. A typical approach is to build the coupling irises separately using thick copper, as the hotspots are mainly concentrated at the coupling irises. These copper irises can be integrated with external heat exchangers, increasing the cooling surface and dissipating heat more efficiently. In [77], an Invar TE_{113} dual-mode bandpass filter with copper irises was demonstrated (see Figure. 2.6(b)), showing an order of magnitude reduction in temperature rise compared to an all-Invar filter. In [79], an extra heat pipe system was integrated into a high-power satellite multiplexer to improve the overall temperature stability. The channel filter in the multiplexer is constructed purely from Invar, while heat pipes containing NH3 were integrated with the Invar cavities as illustrated in Figure. 2.6(c).

To increase the contact area, the TE_{112} signal-mode cavity resonator was used. As the temperature increases, the NH3 evaporates and travels to the evaporation area (near the perimeter of the satellite), where heat is dissipated by radiation. After this, the NH3 condenses, and the cycle continues. Since the medium in the heat pipes is transported by capillary action, no actuators are required. Although the temperature stability can be effectively improved, the increase in mass is evident. The additional cooling system inevitably increases the system's complexity.

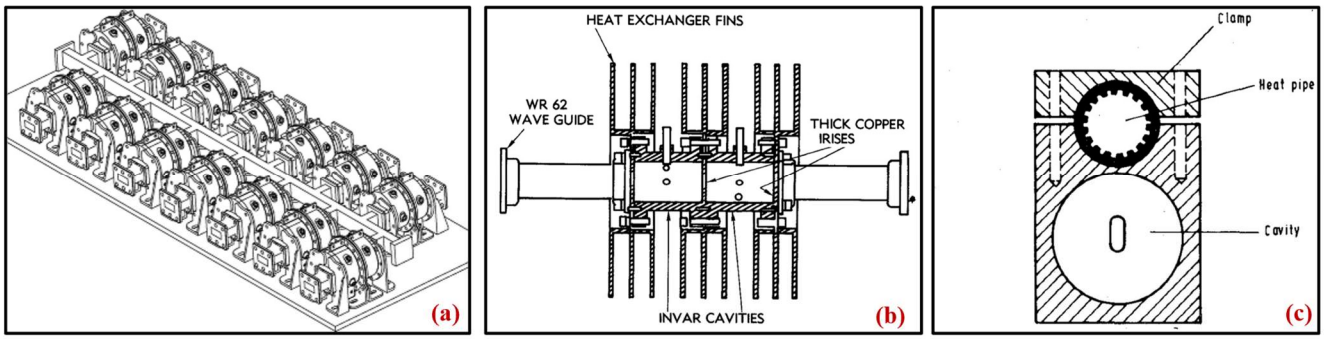

Figure 2.6 Temperature-stable Invar filters and multiplexer. (a) 14-channel herringbone all-invar high-power output multiplexer [25]. (b) Invar TE_{113} dual-mode bandpass filter with copper irises [77]. (c) Cross-section of TE_{112} signal-mode Invar filter with heat pipes [79].

Recently, a high-performance aluminium alloy (AlSi40) has been used in microwave components [80], [81]. AlSi40 has similar density and thermal conductivity to Al6061 alloy, but its CTE is only 13 ppm/K. By changing the alloy composition, the CTE of the substrate material can be further reduced to around 5 ppm/K. In [81], a Ku-band wideband feed filter with a 300 MHz bandwidth was designed and manufactured using AlSi40 alloy. The measurement results show improved thermal stability with an ETC around 13 ppm/K while maintaining low mass and good thermal conductivity.

Apart from metallic materials, a few non-metallic composite materials have also attracted interest from researchers. One is Graphite Fiber Epoxy Composite (GFEC) [82]. GFEC is a graphite composite for high-power space applications. Compared to common Invar multiplexers, the GFEC achieves approximately 50% weight reduction while maintaining similar or even better thermal stability. However, the anisotropic property of this material complicates the design process. The complex manufacturing and plating process present challenges to quality control. Another material with a CTE similar to Invar is carbon-fibre-reinforced plastics (CFRPs) [83]. CFRP is a polymer-based material with low density, high specific stiffness, and a very low CTE ranging from -0.4 to 0.76 ppm/K. This material has been used in antennas for space applications and circuit packaging. One filter application is reported in [83]. However, the significant challenges with this material are its anisotropic nature and the difficulty with metal plating.

2) Temperature Compensation Structures

Introducing extra temperature compensation structures is another common method to improve the thermal stability of microwave components. This compensation mechanism exerts offsetting changes to cancel the geometry thermal expansion in microwave resonant cavities, maintaining a constant resonant frequency. The temperature compensation structures can be either internal [84]–[96] or external [97]–[101].

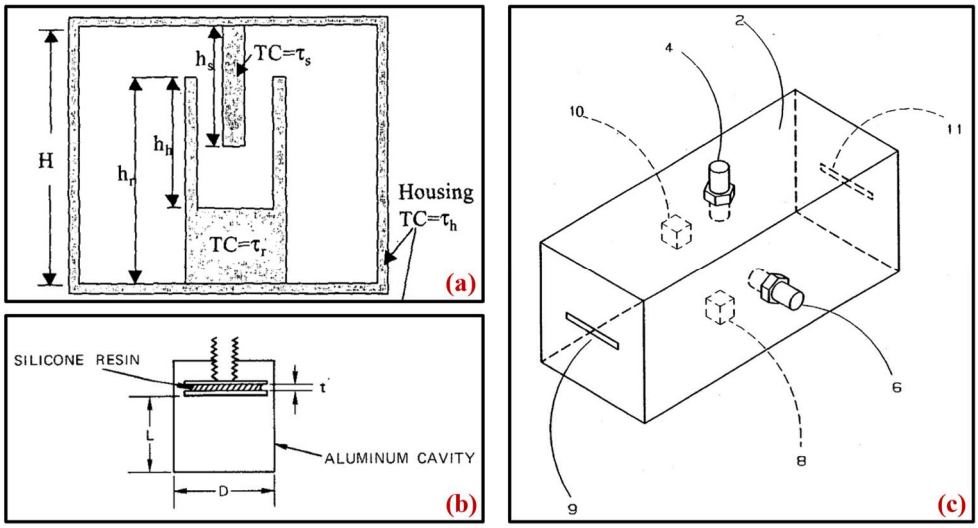

Figure 2.7 Temperature-stable resonators based on internal compensation mechanism. (a) Coaxial resonator [89]. (b) TE_{011} cylinder resonator [92]. (c) TE_{101} rectangular dual-mode resonator [87].

One example of internal compensation mechanism is the temperature-compensated coaxial resonator [84], [85], [89]–[91]. Figure. 2.7(a) illustrates the classical configuration [89], where the coaxial resonator is constructed by materials with different CTE values. By choosing materials with different CTE values for the metallic housing, the partial resonator rod, and the tuning screw, a negative temperature coefficient of the loaded capacitance can be realized, thereby reducing, or even cancelling the thermal-induced frequency shift. Another example of internal compensation is the TE_{011} mode cylinder cavity resonator in [92]. A non-contacting tuning plunger consisting of two metallic disks with a layer of sandwiched silicon resin is inserted into the TE_{011} mode resonant cavity, as presented in Figure. 2.7(b). The silicon resin has a higher CTE value than the metallic disks and housing, offsetting the thermal expansion of the metallic housing. Furthermore, a dielectric compensation method was proposed for multiple-mode resonators and filters [87] as shown in Figure. 2.7(c). By selecting the proper dielectric blocks placed into the resonator cavities, the temperature-induced frequency shift can be balanced by the variation of the permittivity of the dielectric material.

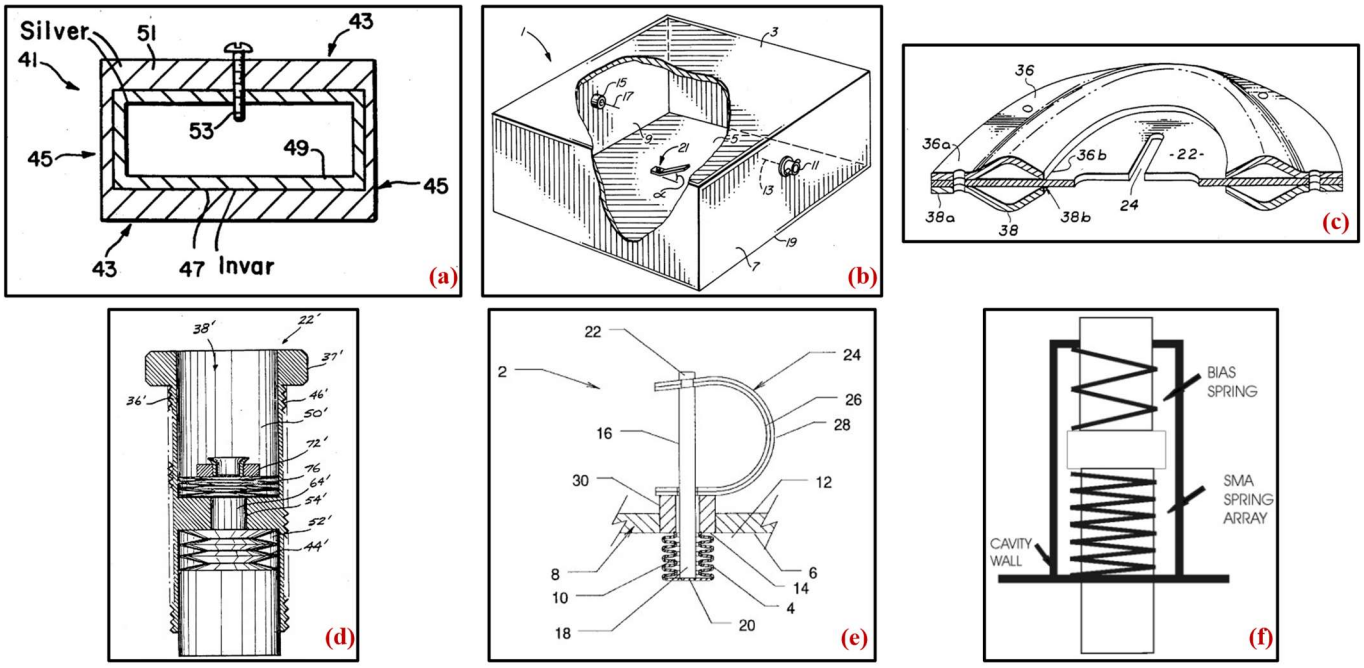

Figure 2.8 Internal temperature compensation structures based on bimetallic actuator and shape memory alloy. (a) Cavity resonator with bimetallic wall [93]. (b) Rectangular resonator with the bimetallic temperature compensation strip [95]. (c) Bimetallic temperature compensation coupling iris [94]. (d) Temperature-compensated tuning screw with a bimetallic washer [96]. (e) Temperature-compensated tuning screw with collapsible pocket [86]. (f) Temperature-compensated tuning screw with shape-memory alloy spring [88].

There are also a few internal temperature compensation schemes based on bimetallic actuators [86], [93]–[96] and shape memory alloys (SMAs) [88]. Bimetal is a layered material, comprising two or more layers, each of which possesses distinct CTE values. With a rise in temperature, the differential expansion in the planar direction across the layers causes an out-of-plane deflection. Shape memory alloys are engineering materials capable of reverting to a pre-set shape as the temperature increases. Figure. 2.8 illustrates some representative temperature compensation structures incorporating the above two engineering materials. In [93], the notion of bimetallic boundary motion was first introduced in a temperature-compensated microwave resonator. The resonator's cavity wall was constructed from bimetal featuring initial deformation in a stabilized curvature condition (see Figure. 2.8(a)). In [95], a wall-mounted internal bimetal compensator was proposed. The compensation level is contingent on the length of the bimetallic strip and can be adjusted using a tuning screw, as presented in Figure. 2.8(b). A bimetallic compensated iris was also proposed in [94]. This design concept involved reducing the electric length of the cavity via a bimetal coupling iris as the temperature increases (see Figure. 2.8(c)). In [96], a temperature-compensated tuning screw was proposed. This design used a bimetallic compensation washer to adjust the protrusion and retraction of the tuning screw, consequently offsetting the temperature-induced changes in the geometry of the cavity filter (see Figure. 2.8(d)). Another bimetal-actuated compensation screw was suggested in [86], where a conductive bellows was sealed with the internal wall to eliminate the small gap between the tuning screw and the metallic housing, as presented in Figure. 2.8(e). Furthermore, study [88] proposed a shape memory alloy-based temperature compensator (see Figure. 2.8(f)). This design involved the SMA spring expanding to its pre-set shape as temperature increased, thereby reducing the penetration of the tuning rod. However, these internal compensation methods often encountered PIM issues, and the inherent hysteretic property of shape memory alloys obstructed its practical application.

In addition to internal compensation, various external compensation mechanisms have also been proposed in the past decades [97]–[101]. Figure. 2.9 illustrates the configurations of these external compensation

structures. In [97], a temperature-compensated filter based on differential expansion is proposed (see Figure. 2.9(a)). The end caps of the microwave filters are constructed from high-expansion materials and protrude into the cavity. As the temperature increases, the end caps will protrude further into the cavity, effectively shortening the electrical length of the cavity. In [98], external control and deflecting rods are employed to constrain cavity expansion (see Figure. 2.9(b)). Each control assembly consists of a pair of side bracing control rods made of low CTE materials and an end deflecting rod made of high CTE materials. This design ensures effective constraint of thermal-induced expansion. A similar approach using external compensators was proposed in [101], as shown in Figure. 2.9(c). The compensator comprises a bent strap, a thumb screw, and a spacer made of low CTE material such as Invar. By leveraging the different thermal expansion rates and the configuration, the thermal-induced changes in the volume of the cavities can be minimized. The amount of compensation can be adjusted by modifying parameters like the cavity end-wall thickness, the bent strap length and thickness, and the spacer height.

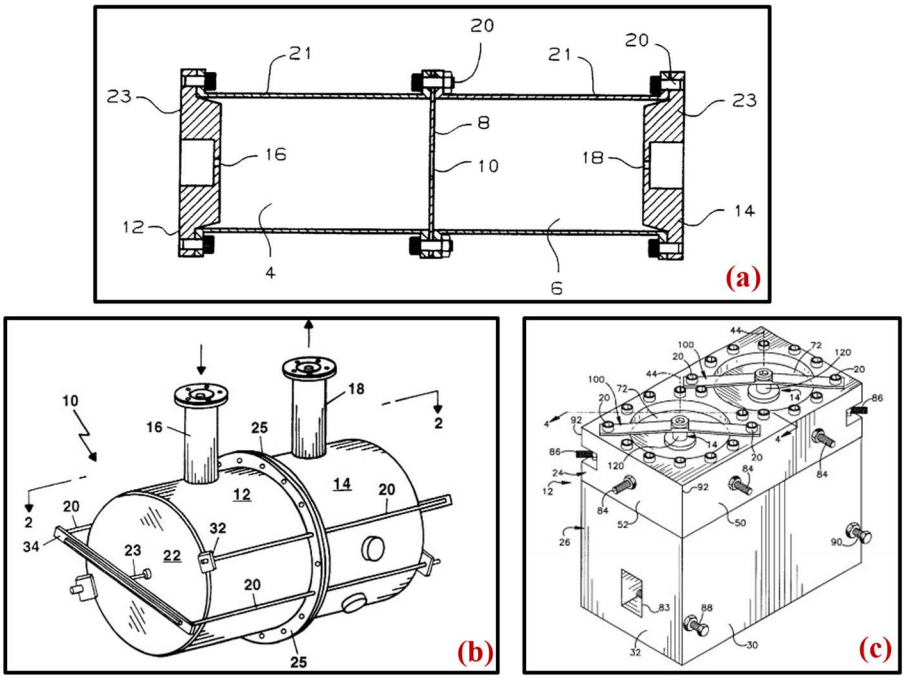

Figure 2.9 Temperature-stable resonators based on external compensation mechanism. (a) Temperature-stable filter with protruded end cap and coupling iris [97]. (b) Temperature-stable filter with external control and deflecting rod [98]. (c) Temperature-stable filter with external temperature compensator [101].

While the external compensation mechanisms can effectively mitigate the potential PIM issue and achieve comparable or even better thermal stability compared to all-Invar components, they also introduce complexities in the assembly process and impose limitations on the filter configuration. Additionally, these compensation structures are highly sensitive to manufacturing tolerances, necessitating a significant amount of empirical iteration during the final implementation. Furthermore, the practical compensation range is constrained by the material properties, and plastic deformation of the cavity end-wall may give rise to severe hysteresis issues.

2.3 Microwave Components Based on Additive Manufacturing Technology

Additive Manufacturing (AM), commonly known as 3D printing, is a versatile manufacturing process that emerged in the 1980s [102]. According to the American Society of Testing and Materials (ASTM), AM is defined as "the process of joining materials to make objects from 3D model data, usually layer upon layer, as opposed to subtractive manufacturing methodologies [103]." Initially, AM technology was primarily used for rapid prototyping of visualization models and tooling. Over the past few years, its application areas have significantly expanded due to advancements in process accuracy and material properties. Today, AM finds widespread use in diverse industries, such as medical, aerospace, and automotive sectors, among others.

The academic interest in 3D printing microwave components began around 2002 when researchers from Purdue University and the University of Michigan Ann Arbor explored ceramic-based metamaterials and electromagnetic bandgap (EBG) structures [104]. During this period, stereolithography apparatus (SLA) technology was utilized to create lost molds to facilitate the fabrication of all-dielectric EBG structures. The same research group also made significant progress by directly manufacturing various passive microwave components using SLA technology [105]–[111].

In recent years, AM of microwave components has gained even more attention due to advancements in AM technology and the increasing demand for next-generation microwave and millimetre-wave devices. The scope of research has expanded to cover various passive microwave components, such as waveguides [112], [113], resonators, and filters [114], [115], as well as antennas and antenna-feed systems [116]–[119]. AM technology has now been recognized as a crucial enabling technology for the development of advanced microwave and millimetre-wave systems for the future [120], [121].

2.3.1 Additive Manufacturing Technology

According to ASTM, AM technologies are classified into seven categories: binder jetting, material jetting, direct energy deposition, sheet lamination, material extrusion, powder bed fusion, and vat photopolymerization. Each category comprises various processes that share the same principle of selectively building layers. Different types of materials such as metals, polymers, and ceramics, can be processed using the same category of AM technology. However, the specific use of these materials depends on the type of AM process employed. The generic workflow for the 3D printing process can be divided into eight steps [102], as illustrated in Figure. 2.10. The printing process begins with a model generated using a three-dimensional Computer-Aided Design (3D CAD) system. Next, the model is converted into the stereolithography (STL) file format, which approximates the 3D model with a mesh of triangles. Subsequently, the STL file is transferred to the AM machine to set the process parameters. These settings are defined based on the geometry of the model (e.g., position and orientation of the components, design of support structures) and the building process (e.g., energy source, material constraints, and layer thickness). At the completion of the printing process, the part is removed from the building platform and prepared for post-processing operations, such as cleaning, sandblasting, or shot-peening, thermal treatments, and plating.

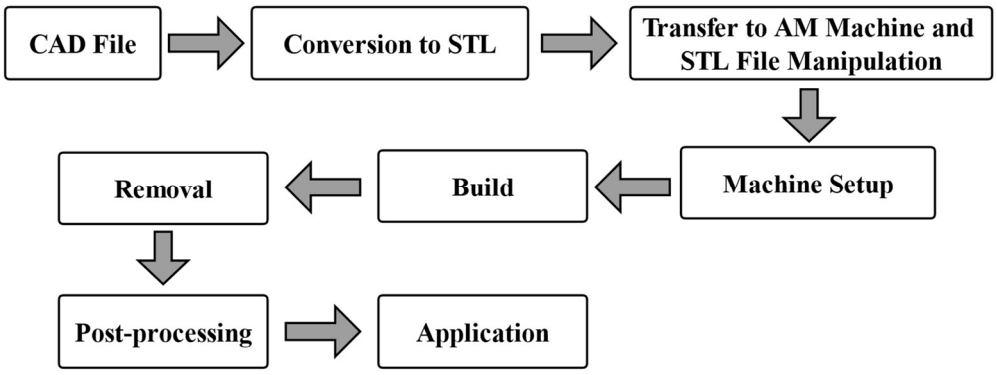

Figure 2.10 Generic AM process of CAD to part, showing all eight steps.

The AM process stands apart from conventional subtractive manufacturing by offering the ability to build complex geometries in a layer-upon-layer fashion. The main advantages of AM are the high freedom of rapid prototyping, the unique capability of free-form fabrication of complex monolithic structures that are difficult or impossible for subtractive techniques, and the versatility of printing with novel materials or even multi-materials. Currently, the most investigated AM techniques in the RF area are material extrusion, material jetting, vat photopolymerization, and powder-bed fusion. This section will provide an overview of each technology, with a particular focus on powder-bed fusion, as it is the primary technology used in this PhD project.

1) Material Extrusion

Material extrusion is considered one of the most common and popular 3D printing technologies, with the largest unit shipments among all 3D printing methods. It offers low machine and feedstock material costs. A typical process in material extrusion is also known as fused deposition modelling (FDM), which was invented and patented in 1989 [122]. This printing technology is based on extrusion and selective deposition of thermoplastic polymers in filament form. The filament is continuously supplied and heated within a moving nozzle at a temperature just above its melting point, enabling easy extrusion through the nozzle to form a layer. Upon extrusion, the material solidifies immediately over the previous layer, and then the vat and platform supporting the part being produced are lifted or lowered by the thickness of a layer, determined by the minimum repeatable mechanical displacement. The nozzle diameter determines both the shape and size of the extruded filament and the minimum feature size that can be printed. The larger the nozzle diameter, the faster the process, but with lower precision. Some FDM machines can be equipped with two or three nozzles, allowing for the use of different building materials or soluble support material. The support material can be dissolved in a chemical or ultrasonic bath after the fabrication process.

2) Material Jetting

The origins of material jetting technology can be traced back to the 1980s, with patents related to the development of Ballistic Particle Manufacturing [102]. Similar to inkjet printing, material jetting creates a 3D model using movable inkjet print heads that jet photopolymer onto a build platform. The droplets are selectively ejected using the drop-on-demand technique, which ensures high accuracy in positioning, low waste, small droplet size, and a wide range of available materials. The printer head deposits the jetted material drops on the substrate, mounted on the build platform, and then the layers are cured and hardened using UV (ultraviolet) light following the print head. Many material jetting machines utilize multi-nozzle print heads to increase speed and enable the deposition of different materials. As a result, soluble or gel-like support material can be used to facilitate the printing of intricate geometries. An essential advantage of material jetting is its

ability to deposit materials of different colours and hardness in the same part, thus creating components with various properties and characteristics.

3) Vat Photopolymerization

Vat photopolymerization is an additive manufacturing process where liquid photopolymer in a vat is selectively cured by light-activated polymerization. SLA is the most representative process of this kind. It was the first commercial AM system developed in 1984 [123]. The photosensitive resin is contained within a vat. The printing process begins when the building platform is lowered from the top of the polymer vat by a specific layer thickness. Subsequently, an ultraviolet laser is used to selectively cure the top layer of the resin, transforming it into a layer of solid material. After the polymerization is completed for one layer, the platform is lowered again, and the surface of the resin is levelled off by a squeegee/blade to provide a smooth resin surface. The process is then repeated until the part is fully constructed. Thereafter, the platform is raised and removed from the machine. During post-processing, the part is cleaned in a chemical bath to remove excess resin, supports are detached, and the part is placed into a UV oven to complete the curing process.

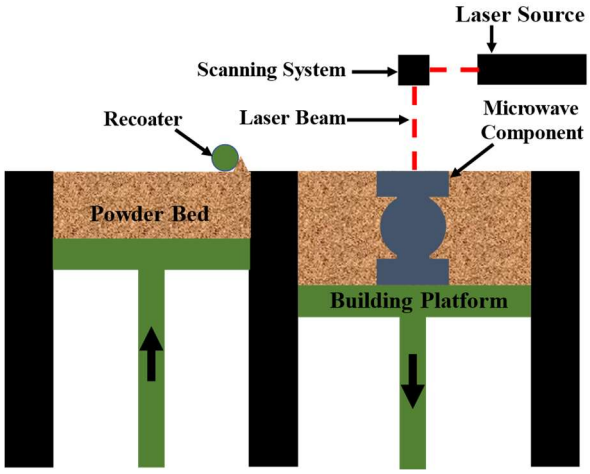

Figure 2.11 Schematic diagram of the general laser powder bed fusion process.

4) Powder Bed Fusion

Powder bed fusion (PBF) process is an additive manufacturing method that enables the direct manufacturing of metal parts. As suggested by the term, powder-based technologies primarily utilize loose powder particles contained in a powder-bed as feedstock. The common powders used include plastic, metal, and ceramics. Selective laser sintering (SLS) was the first commercially adopted PBF process, developed at the University of Texas at Austin [124]. Presently, selective laser melting (SLM) is the most extensively utilized AM technology for manufacturing all-metal microwave components. Unlike the conventional SLS method, SLM technology melts and fuses the metallic powder, transforming it into a liquid phase, which results in the production of more homogeneous and dense parts. More recently, a higher-precision PBF technology called micro laser sintering (MLS) has been commercialised. This is similar to the common PBF process but employs smaller powder particle sizes and thinner layer thicknesses, allowing the manufacturing of micro metal parts with improved accuracy and surface quality. Figure. 2.11 depicts the schematic diagram of a generic laser PBF process. It begins by evenly spreading a thin layer of metal powder using a recoater onto the building platform. A high-energy laser beam is used to selectively fuse the deposited powder layer, following the contour defined in the STL file. After each layer is completed, the building platform is lowered, and a new layer of powder is spread, upon which the laser melts to form the next layer. This process is repeated until the parts are fully manufactured. To prevent oxidation, the process is carried out in a controlled

atmosphere, typically using an inert gas like argon. Once the process is complete, excess powder is removed and recycled, and the parts that remain attached to the building platform undergo a stress-relieving treatment in an oven. This thermal treatment is essential for minimizing deformations caused by the high thermal stresses during manufacturing. Finally, the components are detached from the building platform and may undergo additional post-processing steps.

2.3.2 AM-oriented Design for Microwave Components

The practical manufacturing of microwave components through the AM process poses some particular challenges. Unlike common structural parts, microwave components require higher manufacturing accuracy and surface quality. Additionally, the presence of complex internal irises and channels is a common feature in most microwave devices. These make the implementation of 3D printing for microwave components challenging. One strategy is to divide the component into two or more parts. This allows the complex internal channels to be separately printed, facilitating post-processing. However, this approach comes with the drawback of potential misalignment between the different parts. Moreover, by splitting the component, the unique advantage of AM processes in producing complex monolithic prototypes is not fully utilized. This diminishes the necessity and effectiveness of using AM for microwave components. To fully leverage the advantages of AM processes, the electromagnetic design must be tailored to fit the AM process. An AM-oriented design approach is required [125], [126]. To achieve the best dimension accuracy and surface quality while ensuring the reproducibility of 3D printed microwave components, several key aspects should be considered.

1) Manufacturing Accuracy and Volume

The geometric accuracy of AM processes varies depending on the specific AM approach and processing parameters. Table 2.3 provides a generic summary of the manufacturing accuracy and the typically usable frequency range for different AM technologies, based on reported work in [127], [128]. It is important to note that higher manufacturing accuracy typically comes with a more restrictive manufacturing volume, as with most manufacturing methods. In practical implementation, a trade-off between manufacturing accuracy and building volume must be considered for the targeted microwave component.

Table 2.3 Comparison of Different AM Technologies

Technology	Accuracy (μm)	Frequency Range (GHz)
FDM	100-200	1-20
SLA	< 50	1-90
SLM	< 100	10-50
MLS	< 15	60-180

2) Layer Thickness

In AM processes, components are built layer-by-layer, regardless of the specific AM technique used. Selecting the appropriate layer thickness is a crucial parameter for the manufacturing process. A significant challenge associated with layer thickness is the stair-case effect, as illustrated in Figure. 2.12. Excessively high layer thickness can lead to a substantial increase in approximation error, particularly for objects with small inclination angles. The vertical accuracy of the printing direction is also influenced by the layer thickness. Smaller layer thickness can theoretically improve accuracy, but it comes at the cost of increased printing time. Moreover, the achievable layer thickness is limited by the particle size of the feedstock material and the capability of the 3D printer itself.

As such, finding the right balance between layer thickness, printing time, and accuracy is essential in AM processes. It requires careful consideration and optimization based on the requirements of the microwave components being manufactured. By choosing an appropriate layer thickness, manufacturers can ensure the

production of high-quality components with minimal approximation error and optimal vertical accuracy, while also maintaining an efficient printing process.

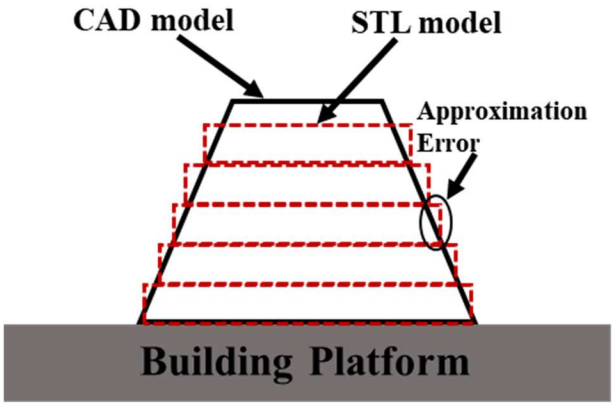

Figure 2.12 Schematic view of staircase effect in AM process

3) Overhangs

Dealing with overhang structures presents a common challenge in 3D printing, as certain areas of a printed part may lack support from the layer below. Different 3D printing processes have their own limitations when it comes to handling overhangs. One solution involves adding extra supporting structures underneath the overhanging surface, as depicted in Figure. 2.13. These supporting structures are typically built in a scaffold-like form during the manufacturing process and require manual removal afterward, resulting in increased complexity and longer fabrication time. More importantly, it should be noted that the surface the supporting structures attach to usually ends up with higher surface roughness or even defects after their removal. There is another approach known as the self-supporting concept. For downward sloping surfaces with inclination angles smaller than the critical angle (usually within a maximum angle of 45° from the vertical), the overhanging structure becomes self-supported, eliminating the need for additional supporting structures. This concept reduces the complexity and time of fabrication for these specific surfaces.

In practical implementation, adjusting the printing direction is a common strategy to reduce or even avoid overhang structures altogether. By carefully selecting the orientation of the part during printing, one can optimize the self-supporting effect and achieve better overall results in terms of surface quality and structural integrity.

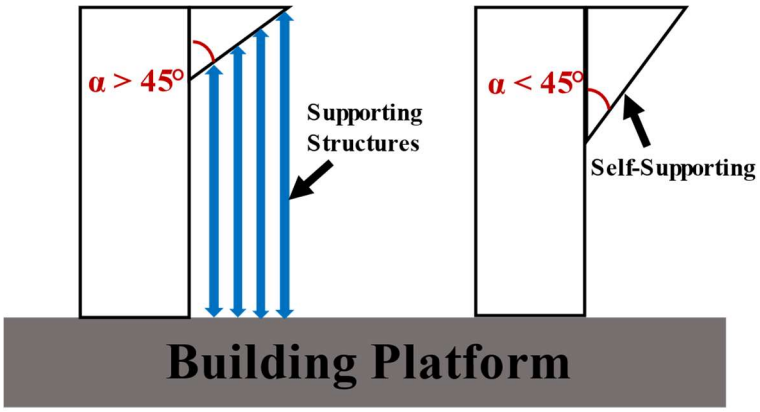

Figure 2.13 Schematic view of overhang structures

4) Residual Stress

Residual stress is another factor that should be considered in AM processes. The rapid changes in physical states during the AM process, such as heating and cooling, can lead to the accumulation of residual stress, which may cause deformation in the fabricated components. To address this issue from a design perspective, incorporating lattice structures or hollowing the solid block can reduce residual stress within the printed part.

For the PBF processes, applying thermal treatment to the as-printed parts is an effective method to relieve residual stress and often an essential process step. Additionally, the use of additional supporting structures and preheating the substrate can help control cooling rates and temperature gradients, further reducing residual stress and minimizing the risk of warping on larger flat surfaces and shrinkage in larger blocks.

In SLA processes, minimizing the printing cross-section and ensuring adequate surface adhesion between the build platform and component play a vital role in avoiding part distortion. Furthermore, pre-compensating the part can help mitigate shrinkage caused by compression stress, making the final product more accurate.

5) Post-Processing

Post-processing for 3D printed microwave components primarily involves surface treatment, such as polishing and plating. For SLA and FDM components made from non-metallic materials, surface metallization is essential to achieve the desired electrical conductivity. For components directly manufactured from metallic powder, surface metal coating may also be necessary due to the insufficient electrical conductivity of the metallic materials. Common plating methods include silver painting, electroless plating, and electroplating. Electroless plating is compatible with non-metallic materials, while electroplating involves coating a layer of metal onto an electrically conductive material. A combination of both approaches is often employed to achieve better coverage and surface conductivity.

For plating, it is crucial to ensure that the thickness of the coated metal layer is greater than five times the skin depth to minimize microwave loss. it is also well known that the surface roughness of the components significantly affects their effective conductivity. Common polishing methods, such as sandpapering, shot-peening, and vibration polishing, are utilized to improve the surface smoothness. From a design perspective, it is beneficial to place the electrical current concentrating area away from the downward surface with the worst surface roughness. This design strategy helps optimize the overall performance of the microwave components.

2.3.3 3-D Printed Microwave Filters

As this PhD project primarily focuses on microwave filters, the following subsections will review the reported 3D printed microwave filters. These filters can be put into three categories based on the material used.

1) Polymer-based 3D printed microwave filters

As previously mentioned, the plastic SLA process was among the first AM technologies used in the microwave field. In 2004, two 3D printed polymer microwave filters were reported [105], [106]. In [106], an X-band evanescent resonator filter based on capacitive loading posts and periodic vias was proposed. The entire filter was printed into two pieces and then bonded together after metallization. In [105], a K-band rectangular cavity filter with a vertical configuration was proposed. The filter consisted of four rectangular resonators and was fed by coaxial probes. To facilitate fabrication, the filter was split along the E-plane of the rectangular resonator. Both articles demonstrated good agreement between experimental responses and simulations, validating the feasibility of the SLA process for microwave filters. Another study [129] investigated a two-step metallization procedure for polymer-based microwave components. They developed an X-band rectangular waveguide filter with a slanted coupling iris as a test bench, achieving an impressive quality factor (Q_u) over 6000. A few SLA based millimetre-wave filters have also been reported [112], [130].

In [130], a W-band rectangular waveguide filter was presented, fabricated as a single piece with multiple apertures on the outer surface to facilitate metallization.

FDM technology has been another common AM process used in the fabrication of microwave filters [131]–[133]. One of the first attempts was reported in [131], where a corrugated low-pass filter, a high-pass filter, and an iris-coupled band-pass filter were presented. In [132], researchers proposed a 3D printed waveguide insert that, when placed into a standard waveguide, easily implements an inline waveguide filter, reducing manufacturing costs and lead time. In [133], an X-band extracted-pole filter was presented, realizing the zero-pole block through a symmetrical oversized cavity. To facilitate the printing process, the filter was split along the E-plane into two pieces. Additionally, a Ka-band groove gap waveguide filter fabricated using polymer jetting (PolyJet) technology was proposed in [134]. Compared to its CNC-machined counterpart, this 3D printed filter showed evident improvement in response while achieving significant weight reduction.

In addition to the common waveguide cavity filters, many 3D printed filters with novel cavity geometries have been proposed, taking advantage of the manufacturing flexibility offered by AM processes. A series of spherical and hemispherical cavity filters were reported in [135]–[139]. Compared to the conventional rectangular or cylindrical cavity resonators, spherical resonators exhibit significant advantages in terms of Q_u and spurious resonance modes, especially in dual-mode operation. However, the complex curved surfaces of spherical resonators make them challenging to fabricate using conventional CNC machines, making 3D printing an attractive alternative. Another interesting tunable waveguide filter based on shaped cavity was reported in [140]. The filter is divided into two halves along the E-plane, and a rotated spiral ribbon is inserted into the cavity to tune the centre frequency.

Transmission-line-based resonator filters, such as helical filters and coaxial filters, are another type of filters that can leverage the free-forming capability of polymer AM processes. Traditionally, these filters are assembled from several parts, such as a housing, a cover, and internal posts or helixes attached inside the housing. With 3D printing, the assembly process can be significantly simplified, often requiring only two parts: the housing and the cover. In [141]–[144], several 3D printed combline filters were reported, where novel doublet topology and mixed electromagnetic coupling were employed to enhance filter performance. A novel planar in-line coaxial line filter was proposed in [145], where the coaxial line is attached to the enclosure with supports. The portions of the lines without support act as resonators, while the supports serve as coupling elements. In [146], a half-wavelength helical resonator with a variable helix was proposed, enabling higher Q_u and a wider spurious-free range. Apart from these 3D structures, a few 3D printed planar filters were also reported [147], [148].

The main characteristics of some of the polymer-based 3D printed filters presented in this section are summarized in Table 2.4. From this table, it is evident that a wide range of standard rectangular waveguide filters, ranging from X-band to W-band, have been reported. The experimental results of these filters show good agreement with the simulations, verifying the feasibility of polymer-based 3D printed microwave filters. Several metallization methods have been established, enabling fast and low-cost prototyping of microwave components using AM technology. Furthermore, several novel filter configurations with advanced filter functions were reported, taking advantage of the flexibility of the polymer-based AM process. Compared to conventional microwave filters, these novel resonator structures allow for simplified fabrication processes, while effectively enhancing the RF performance of the filters.

Table 2.4 Comparison between the reported polymer-based 3D printed microwave filters

Ref	Filter Type	Resonator Type	f_0 (Sim./Meas) (GHz)	FBW	IL (Meas.) (dB)	AM and metallization technology
[106]	2nd-order Chebyshev response	Evanescent mode resonator	11.95/11.96	1.8%	0.61	SLA Photopolymer (Conductive ink painted and Copper electroplated)
[129]	3rd-order Chebyshev response	Rectangular resonator	9.98/9.98	2.2%	0.16	SLA Photopolymer (Silver painted and copper electroplated)
[130]	5th-order Chebyshev response	Rectangular resonator	90/87.5	11.1%	0.4	SLA Photosensitive resin (Copper electroplated with gold passivation)
[131]	4th-order Chebyshev response	Rectangular resonator	13.85/-	2.88%	2.8	FDM PLA (Silver painted)
[133]	4th-order Quasi-elliptic response	Rectangular resonator	11/11.2	9.1%	0.9	FDM PLA (Copper sprayed and galvanized)
[134]	4th-order Quasi-elliptic response	Groove gap waveguide resonator	35.65/35.65	1.4%	0.45	PolyJet Photopolymer (Copper electroless plated)
[136]	4th-order Quasi-elliptic response	Spherical dual-mode resonator	10/10	3%	0.24	SLA Photopolymer (Copper electroless plated)
[143]	4th-order Quasi-elliptic response	Asymmetric mushroom-shaped resonator	1.8/1.83	2.8%	0.54	SLA Photopolymer (Silver painted and copper electroplated)
[145]	4th-order; Chebyshev response	In-line coaxial resonator	3/3	3.3%	1.45	SLA Photopolymer (Silver painted and copper electroplated)
[146]	4th-order; Chebyshev response	Helical resonator	0.5/0.5	4%	0.9	SLA Photopolymer (Silver electroplated)
[148]	3rd-order Chebyshev response	Microstrip resonator	98/95	5.1%	8	Ink-Jetting Polyimide ink and silver nano-particle ink

2) Metal-based 3D printed microwave filters

The first 3D printed metallic microwave filter was reported in 2009 by researchers from the European Space Agency [149]. Using Selective Laser Melting (SLM) technology, they printed a fifth-order waveguide passband filter operating in the Ku band, directly from titanium (Grade 2) and aluminum alloy (AlSi10Mg). The filter was printed as a single part, leveraging the geometric freedom offered by AM to shape the resonator and coupling iris and minimize the insertion loss. Booth et al. from Airbus presented a series of K/Ku-band 3D printed super-ellipsoid resonator filters in [150], [151]. Compared to classical rectangular waveguide filters, the super-ellipsoid filter achieved higher rejection levels and a wider spurious-free range. The 3D printed filter prototypes successfully passed all space qualification tests, demonstrating that SLM-printed metallic microwave components can competitively replace conventional CNC waveguide components in satellite payloads. In [152], a fourth-order X-band lollipop-shaped resonator filter with a Chebyshev response was designed and directly implemented using metallic printing. The lollipop-shaped resonator was a variation of the well-known mushroom-shaped resonator, and the filter was designed to be manufactured in a single piece. Leveraging the special free-form capability, a series of composite step/stub filters were developed in [153], [154]. Compared to iris-coupled filters, the stub structure was more suitable for AM processes. The AM-oriented design process was used in this work. It mainly involves rotating the printing direction and tilting the stubs downward, allowing the entire filter to be printed monolithically along the propagation direction. A comparative study of these stub filters was conducted in [155], where filters were printed using different materials such as aluminium alloy (AlSi10Mg), titanium alloy (Ti6Al4V), and maraging steel. The printing parameters were fine-tuned through pre-manufacturing and measuring the waveguide transmission lines. Additionally, the outer profile of the filter was redesigned to maximize heat transfer and reduce deformation caused by thermal residual stress. The results showed excellent agreement between measured and simulated scattering parameters for all filter prototypes. In [156], a Ka-band monolithic 4th-order waveguide filter manufactured using the metallic binder jetting (BJ) printing technology was reported. The paper provided a detailed investigation of the fabrication process and the RF performance. However, a significant frequency shift was observed in the experimental response due to relatively large dimensional variations.

In addition to filters operating at or below the Ka-band, a few 3D printed metallic filters operate at millimetre-wave and even sub-terahertz frequency bands. In [157], two E-band rectangular waveguide filters were printed from copper-tin alloy (CuSn15) using SLM technology. However, due to limitations in manufacturing tolerance and surface roughness, significant degradation in RF performance was observed. A more suitable AM process for millimetre-wave applications is the micro laser sintering (MLS) technology. In [158], Salek et al. reported a W-band 5th-order rectangular waveguide filter, with two prototypes printed from stainless steel using MLS technology, and one further electroplated with copper. Measurement results showed good agreement between measured return loss and simulated results, with measured insertion loss close to 1 dB around 90 GHz. Researchers also attempted to push the upper frequency limit of MLS printed components, leading to the reporting of a D-band waveguide diplexer [159] and a 300 GHz waveguide filter [160]. However, both devices exhibited evident degradation in terms of centre frequency and insertion loss. Additionally, these devices were designed in E-plane split-block configurations, resulting in extra assembly error. More recently, a G-band 3D printed monolithic waveguide filter was reported in [128], where the printing quality was investigated in detail to evaluate the boundaries of MLS technology for manufacturing sub-terahertz monolithic devices. A specially developed gold-plating process was employed, and the as-printed stainless-steel filters underwent multiple supplements plating processes, achieving an impressive insertion loss of 0.5 dB. Another AM technology potentially suitable for manufacturing sub-terahertz filters is 3D screen printing, a new AM technique based on a modified screen-printing process using the powder-binder mixture. In [161], a 300 GHz rectangular waveguide filter was manufactured using this emerging 3D printing technique. The filter was fabricated in multiple pieces and gold-plated. However, there was a

significant frequency shift and return loss deterioration in the experimental responses compared to simulated ones.

Table 2.5 summarizes the main characteristics of the 3D printed metal filters discussed in this section. From this table, we can find that a wide range of 3D-printed metallic filters, from X-band to sub-terahertz frequencies, have been reported. For filters below the Ka-band, the experimental responses show good agreement with the simulations, demonstrating that SLM technology can be a viable manufacturing solution for microwave filters in these frequency bands. For filters operating in the millimetre-wave frequency band, some initial work (up to G-band) based on the MLS process has presented very promising results. However, most reported filters are based on rectangular waveguide resonators with Chebyshev responses, and the flexibility of monolithically manufacturing complex geometric structures has not been fully exploited. Considering the current manufacturing resolution of 3D printing technologies, they might not be a reliable manufacturing technology as yet for sub-terahertz microwave filters.

Table 2.5 Comparison between the reported metal-based 3D printed microwave filters

Ref	Filter Order and Response	Resonator Type	f_0 (Sim./Meas) (GHz)	FBW	Meas. IL (dB)	Printing Techniques and Material
[149]	5th-order Chebyshev bandpass filter	Shaped rectangular resonator	11/11.12	1.8%	1	SLM AlSi10Mg, Titanium (Silver plated)
[151]	9th-order Quasi-elliptic bandpass filter	Depressed super-ellipsoid resonator	12.875/12.88	1.9	1	SLM Scalmalloy (Silver plated)
[152]	4th-order Chebyshev bandpass filter	Lollipop-shaped resonator	7.924/7.926	3.9	1.1	SLM Stainless Steel
[155]	6th-order; Chebyshev low-pass filter	Composite step/stub resonator	13.725/13.725	18.2	0.1	SLM AlSi10Mg, Ti6Al4V Maraging steel (Silver plated)
[156]	4th-order; Chebyshev bandpass filter	Rectangular resonator	32/32.35	6.3	1	BJ Stainless Steel (Copper infiltrated)
[157]	11th-order; Chebyshev bandpass filter	Rectangular resonator	83.5/87	6.0	3	SLM CuSn15
[158]	5th-order; Chebyshev bandpass filter	Rectangular resonator	90/89.1	11	1	MLS Stainless Steel (Copper plated)
[160]	5th-order; Chebyshev bandpass filter	Rectangular resonator	300/297	10.5	1.9	MLS Stainless Steel (Gold plated)
[128]	5th-order; Chebyshev bandpass filter	Rectangular resonator	180/179.94	11	1	MLS Stainless Steel (Gold plated)
[161]	5th-order Chebyshev bandpass filter	Rectangular resonator	300/313.2	9	3	3D Screen Printing Tungsten-copper (Gold Plated)

3) Ceramic-based 3D printed microwave filters

Compared to air-filled cavity filters, dielectric resonator filters offer the advantage of miniaturization, as the wavelength in dielectric ceramic material is smaller than in the free space. Since the introduction of dielectric resonators in microwave filter design, enormous advances have been achieved. Conventionally, fabricating these filters has been challenging. Special molds are often required to manufacture the dielectric puck, which is only cost-effective for large-scale production, and the practical design freedom is usually limited. On the other hand, binding and soldering separate dielectric blocks together require high assembly accuracy. Even minor misalignments could lead to considerable degradation in filter performance.

Recent advances in ceramic 3D printing have spurred researchers to explore its application in microwave component fabrication. Several 3D printed dielectric resonator filters have been reported in [162]–[167]. The 3D ceramic SLA process was initially tested in [162] to manufacture a microwave filter. This work involved printing periodic dielectric structures from high permittivity ceramics such as Yttria-stabilized Zirconia (ZrO_2) and $Ba_3ZnTa_2O_9$ (BZT). The printed dielectric plates were then inserted into a common air metallic cavity to create high-Q_u resonators and filters. In [163], a C-band dielectric wideband filter based on $TM_{01\delta}$ mode was proposed, where all resonators and inter-resonator coupling elements were designed and implemented in a single piece using ceramic SLA process. However, the measured bandwidth was only half of the designed bandwidth (400 MHz), due to cracks in the two end resonators. Another work based on ceramic SLA process is the X-band skeleton-like monolithic dielectric filter [164]. Designed with a quasi-elliptic response, this filter combines all dielectric resonators through the dielectric arms and spinal column. This innovative design eliminates the need for adhesive glue and supporting structures, reducing losses and assembly errors. More recently, a novel ceramic AM technology, known as Lithography based Ceramic Manufacturing (LCM), has emerged and has also been applied in the manufacture of dielectric filters. Unlike common SLA technology, LCM is a mask-based SLA method where an integral image is projected onto the photopolymerizable slurry surface through an optical system. In [165], a monolithic TM single-mode dielectric resonator filter manufactured by LCM process was presented, with the filter printed as a single piece of dielectric puck. The outer surface of the dielectric block was metallized to replace the conventional metallic housing. A similar piece of work on TM dual-mode dielectric filter was reported in [166]. In this case, an X-shaped dielectric resonator with a pair of orthogonal TM_{010} operating modes was proposed, and the entire resonator structure as well as the housing were printed using LCM technology in a single piece. However, noticeable frequency shifts and bandwidth deterioration were observed in the experimental results for both designs.

Table 2.6 provides a summary of the main characteristics of the 3D printed dielectric filters discussed in this section. From this table, it is evident that the reported dielectric resonator filters mainly involve the $TE_{01\delta}$ and TM_{010} mode dielectric resonators, and the vat photopolymerization process was predominantly employed in their fabrication. The research on ceramic-based 3D printed microwave filters is in the early stage compared to its plastic and metallic counterparts. Future research and development are needed to fully exploit the capability of ceramic AM technology for microwave components design and manufacturing.

Table 2.6 Comparison between the reported ceramic-based 3D printed microwave filters

Ref	Filter Order and Response	Resonator Type	f_0 (Sim./Meas) (GHz)	FBW	Meas. IL (dB)	Printing Techniques and Material
[162]	3rd-order Chebyshev bandpass filter	Dielectric periodic structure	33.0/ 32.9	1%	3	SLA Zirconia and BZT
[163]	4th-order Chebyshev bandpass filter	TM010 mode resonator	4/4.05	5%	0.3	SLA Zirconia
[164]	6th-order Quasi-elliptic bandpass filter	TE01δ mode resonator	11.75/11.74	1.7%	1.8	SLA Alumina
[165]	2nd-order Chebyshev bandpass filter	TM010 mode resonator	8.3/8.0	1.3%	1.5	SLA Alumina
[166]	4th-order Quasi-elliptic bandpass filter	TM010 dual-mode resonator	6.0/5.9	4.7%	0.7	SLA Alumina

2.4 Discussion on the State-of-the-art and Research Objectives

The literature review provides valuable insights into the research state-of-the-art in the research fields involved in this PhD project. The main conclusions drawn from the above review are as follows:

For the microwave filters in satellite payload, the classical design paradigm has been well established. Wideband feed filters typically utilize TE_{10N} and TM mode rectangular resonators, while narrowband channel filters commonly adopt TE_{11N} and TE_{011} mode cylinder resonators. To improve out-of-band selectivity, the cross coupling and extracted-pole techniques have been developed, enabling the realization of the quasi-elliptic filter response.

The power handling capability of microwave filters is constrained by several factors, such as PIM interference, high-power breakdown, and thermal-induced frequency detuning. While a complete analytical theory for PIM interference has not been established, several practical methods can be employed to mitigate its impact. For high-power breakdown, classical analytical theories and design guidelines are well established. The development of numerical methods further simplifies the analysis of breakdown phenomena and provides more accurate breakdown threshold estimations. Effective breakdown prevention methods have also been summarized. To address thermal-induced frequency detuning, classical methods involving the use of low-CTE materials and temperature compensation structures have been developed. Notably, in many practical applications, the power handling capability of microwave components is determined by the permissible temperature rise of the equipment rather than microwave breakdown limitations. Hence, maintaining good temperature stability is crucial for high-power microwave filter design.

The development of AM technology indeed opens new perspectives for design of microwave components, leading to the prodigious numbers of expert-level publications on 3D printed microwave components. Among the AM technologies, the SLA process is primarily employed for polymer-based microwave filters. Several microwave filters with novel cavity geometries and enhanced RF performance have been reported. The feasibility and flexibility of SLA in manufacturing polymer-based microwave filters have been well demonstrated. Although such polymer-based microwave filters can feature near-net shape manufacturing and highly reduced weight, but their mechanical strength and poor thermal handling capability hinder their practical application in the real-world high-power scenarios, making them suitable mainly for proof-of-concept prototypes. For metal-based 3D printed filters, SLM is the prominent AM technology. Its feasibility in manufacturing microwave filters has been verified through numerous reported 3D printed metallic filters ranging from X-band to G-band. However, most metallic 3-D printing filters are of relatively wide bandwidth (greater than 2%), unsuitable for the narrowband channel characteristics required for many satellite communications systems. Although some 3-D printed narrowband metallic filters were also reported, the used metallic materials only concentrate on common stainless steel and aluminium alloy. The high CTE value of these materials also limits the practical high-power application of these designs. Moreover, most reported metal-based filters are the standard rectangular waveguide filter, the full potential of monolithically manufacturing complex geometric structures using SLM process has not been fully exploited. Regarding ceramic-based 3D printed filters, the employed AM processes mainly involve SLA technology, and the reported 3D printed dielectric filters only focus on $TE_{01\delta}$ and TM_{010} mode dielectric resonators. Moreover, experimental results indicate significant degradation in most reported 3D printed dielectric filters. The research on ceramic-based 3D printed microwave filters is still in its early stages, and the relevant research is relatively limited compared to the polymer-based and metal-based counterparts. More investigations are required to unlock the full potential of the ceramic 3D printing technology in this field.

Recently, the rapid advancement of satellite communication technology, particularly the emergence of very high-throughput satellite (VHTS) systems and satellite internet constellation systems, has fuelled a growing demand for high-power microwave filters. For example, the HTS needs more transponders to enable

the frequency reuse and the multiple spot-beams system. The satellite payloads operating at the higher frequency (Ku, Ka, V-band) also requires the higher channel power. Apart from the electrical specification, other evolving requirements, such as the more stringent footprint and weight limitations, all present significant challenges to the current satellite microwave filter solutions. These demanding requirements not only increases the complexity in the filter design but also pose the challenge to the manufacture of the microwave filters. Therefore, an evolution from the current microwave filters is indispensable to meet the increasing communication demand.

This PhD project aims to address these challenges by leveraging advanced manufacturing techniques, primarily focusing on AM technology and novel materials. The research motivation and scope are summarized as follows:

(1) The AM technology will be utilized to overcome the complex manufacturability issues associated with Invar alloy, and a new alternative end-to-end fabrication route will be established for all-Invar high-power microwave components.

(2) The combination of 3D printing technology and novel thermal-stable alloys will be explored to open new opportunities for temperature compensation mechanisms. Feasible end-to-end fabrication solutions for microwave components will be investigated for several novel low-CTE alloy materials.

(3) The application of novel non-metallic materials in high-power microwave components will be investigated.

(4) The manufacturing flexibility of metal AM processes will be exploited to design novel metal-based 3D printed filters.

(5) The advantages of ceramic 3D printing technology in manufacturing complex monolithic geometries will be harnessed to design novel dielectric microwave filters.

2.5 Summary

This chapter provides a comprehensive review of the relevant literature pertinent to this PhD project. The reviewed topics encompass microwave filters designed for satellite applications, practical considerations in power handling capability, and the application of 3D printing technology in microwave components. The state-of-the-art research in these areas is thoroughly examined, shedding light on the current advancements and challenges. Additionally, the chapter outlines the objectives and contributions of this PhD project. By delving into the prior art of these research areas and their interconnections, this chapter sets the stage for this thesis.

Reference

[1] V. E. Boria and B. Gimeno, “Waveguide filters for satellites,” *IEEE Microw. Mag.*, vol. 8, no. 5, pp. 60–70, 2007, doi: 10.1109/MMM.2007.903649.

[2] S. Shin and S. Kanamaluru, “Diplexer design using EM and circuit simulation techniques,” *IEEE Microw. Mag.*, vol. 8, no. 2, pp. 77–82, Apr. 2007, doi: 10.1109/MMW.2007.335532.

[3] R. Levy and S. B. Cohn, “A History of Microwave Filter Research, Design, and Development,” *IEEE Trans. Microw. Theory Tech.*, vol. 32, no. 9, pp. 1055–1067, 1984, doi: 10.1109/TMTT.1984.1132817.

[4] J. Ding, S. Shi, and W. Wu, “Cavity bandpass filters with quasi-elliptic response at 220GHz,” *9th Int. Conf. Microw. Millim. Wave Technol. ICMMT 2016 - Proc.*, vol. 2, pp. 940–942, 2016, doi: 10.1109/ICMMT.2016.7762493.

[5] M. Yu and Y. Yang, “Unified Extracted Pole Filter Synthesis: Bridging the Gap Between EM and Circuit Simulations,” *IEEE Microw. Mag.*, vol. 21, no. 3, pp. 84–95, Mar. 2020, doi: 10.1109/MMM.2019.2958163.
[6] J. R. Montejo-Garai, J. A. Ruiz-Cruz, J. M. Rebollar, M. J. Padilla-Cruz, A. Oñoro-Navarro, and I. Hidalgo-Carpintero, “Synthesis and design of In-line N-order filters with N real transmission zeros by means of extracted poles implemented in low-cost rectangular H-plane waveguide,” *IEEE Trans. Microw. Theory Tech.*, vol. 53, no. 5, pp. 1636–1642, 2005, doi: 10.1109/TMTT.2005.847053.
[7] U. Rosenberg, “New ‘Planar’ waveguide cavity elliptic function filters,” *1995 25th Eur. Microw. Conf.*, vol. 1, pp. 524–527, 1995, doi: 10.1109/EUMA.1995.337014.
[8] D. Miek, A. Morán-López, J. A. Ruiz-Cruz, and M. Höft, “Ku-Band Waveguide Filter with Multiple Transmission Zeros by Resonant Source to Load and Bypass Cross-Coupling,” *2019 49th Eur. Microw. Conf. EuMC 2019*, pp. 57–60, 2019, doi: 10.23919/EuMC.2019.8910677.
[9] D. Miek, P. Boe, F. Kamrath, and M. Höft, “Techniques for the generation of multiple additional transmission zeros in H-plane waveguide filters,” *Int. J. Microw. Wirel. Technol.*, vol. 12, no. 8, pp. 723–732, 2020, doi: 10.1017/S1759078720000811.
[10] J. Q. DIng, S. C. Shi, K. Zhou, Y. Zhao, D. Liu, and W. Wu, “WR-3 Band Quasi-Elliptical Waveguide Filters Using Higher Order Mode Resonances,” *IEEE Trans. Terahertz Sci. Technol.*, vol. 7, no. 3, pp. 302–309, May 2017, doi: 10.1109/TTHZ.2017.2686007.
[11] J. Ossorio, S. Cogollos, V. Boria, and M. Guglielmi, “Rectangular Waveguide Quadruplet Filter for Satellite Applications,” *IEEE MTT-S Int. Microw. Symp. Dig.*, vol. 2019-June, pp. 1359–1362, 2019, doi: 10.1109/mwsym.2019.8701045.
[12] J. O. Garcia, J. C. M. Lermas, S. Cogollos, V. E. Boria, and M. Guglielmi, “Waveguide Quadruplet Diplexer for Multi-Beam Satellite Applications,” *IEEE Access*, vol. 8, pp. 110116–110128, 2020, doi: 10.1109/ACCESS.2020.3002818.
[13] S. Cogollos, P. Soto, M. Brumos, V. E. Boria, and M. Guglielmi, “Novel rectangular waveguide structures for advanced filter characteristics,” *IEEE MTT-S Int. Microw. Symp. Dig.*, pp. 14–17, 2014, doi: 10.1109/MWSYM.2014.6848424.
[14] S. Cogollos *et al.*, “Efficient Design of Waveguide Manifold Multiplexers Based on Low-Order EM Distributed Models,” *IEEE Trans. Microw. Theory Tech.*, vol. 63, no. 8, pp. 2540–2549, 2015, doi: 10.1109/TMTT.2015.2442990.
[15] U. Rosenberg, S. Amari, and J. Bornemann, “Inline TM110-mode filters with high-design flexibility by utilizing bypass couplings of nonresonating TE10/01 modes,” *IEEE Trans. Microw. Theory Tech.*, vol. 51, no. 6, pp. 1735–1742, 2003, doi: 10.1109/TMTT.2003.812577.
[16] C. Tomassoni, S. Bastioli, and R. Sorrentino, “Generalized TM dual-mode cavity filters,” *IEEE Trans. Microw. Theory Tech.*, vol. 59, no. 12 PART 2, pp. 3338–3346, 2011, doi: 10.1109/TMTT.2011.2172622.
[17] P. Vallerotonda *et al.*, “Compact waveguide bandpass filters for broadband space applications in c and ku-bands,” *Proc. Eur. Microw. Conf. Cent. Eur. EuMCE 2019*, pp. 116–119, 2019.
[18] S. Bastioli, L. Marcaccioli, C. Tomassoni, and R. Sorrentino, “Ultra-compact highly-selective dual-mode pseudoelliptic filters,” *Electron. Lett.*, vol. 46, no. 2, p. 147, 2010, doi: 10.1049/el.2010.2971.
[19] S. Bastioli, C. Tomassoni, and R. Sorrentino, “A new class of waveguide dual-mode filters using TM and nonresonating modes,” *IEEE Trans. Microw. Theory Tech.*, vol. 58, no. 12 PART 2, pp. 3909–3917, 2010, doi: 10.1109/TMTT.2010.2086068.
[20] L. Pelliccia *et al.*, “Very-compact Waveguide Bandpass Filter based on Dual-Mode TM Cavities for Satellite Applications in Ku-band,” *2018 48th Eur. Microw. Conf. EuMC 2018*, pp. 93–96, 2018, doi: 10.23919/EuMC.2018.8541740.
[21] C. Tomassoni, M. Dionigi, and R. Sorrentino, “Strategies for the improvement of the out of band behavior of TM dual-mode filters,” *2015 IEEE 1st Int. Forum Res. Technol. Soc. Ind. RTSI 2015 -*

Proc., pp. 90–93, 2015, doi: 10.1109/RTSI.2015.7325076.
[22] C. Tomassoni *et al.*, "Compact broadband waveguide filter with wide spurious-free range based on mixed TM and combline resonators," in *2017 47th European Microwave Conference (EuMC)*, IEEE, Oct. 2017, pp. 985–988. doi: 10.23919/EuMC.2017.8231011.
[23] A. E. Williams, "A Four-Cavity Elliptic Waveguide Filter," *IEEE Trans. Microw. Theory Tech.*, vol. 18, no. 12, pp. 1109–1114, Dec. 1970, doi: 10.1109/TMTT.1970.1127419.
[24] B. Yassini and M. Yu, "A novel ka band dual mode super Q Cavity Filter," *IEEE MTT-S Int. Microw. Symp. Dig.*, pp. 220–222, 2014, doi: 10.1109/MWSYM.2014.6848452.
[25] B. Yassini and M. Yu, "Ka-Band Dual-Mode Super Q Filters and Multiplexers," *IEEE Trans. Microw. Theory Tech.*, vol. 63, no. 10, pp. 3391–3397, Oct. 2015, doi: 10.1109/TMTT.2015.2462822.
[26] Ming Yu, D. J. Smith, A. Sivadas, and W. Fitzpatrick, "A dual mode filter with trifurcated iris and reduced footprint," in *2002 IEEE MTT-S International Microwave Symposium Digest (Cat. No.02CH37278)*, IEEE, 2002, pp. 1457–1460. doi: 10.1109/MWSYM.2002.1012130.
[27] D. Wolk, J.-M. Mari, and D. Rosowsky, "The 14 channel C-band output multiplexer assembly for Intelsat 805/806," in *16th International Communications Satellite Systems Conference*, Reston, Virigina: American Institute of Aeronautics and Astronautics, Feb. 1996. doi: 10.2514/6.1996-982.
[28] G. Pfitzenmaier, "A Waveguide Multiplexer with Dual-Mode Filters for Satellite Use," in *1975 5th European Microwave Conference*, IEEE, Oct. 1975, pp. 407–411. doi: 10.1109/EUMA.1975.332227.
[29] S. Cogollos *et al.*, "A systematic design procedure of classical dual-mode circular waveguide filters using an equivalent distributed model," *IEEE Trans. Microw. Theory Tech.*, vol. 60, no. 4, pp. 1006–1017, 2012, doi: 10.1109/TMTT.2012.2183381.
[30] M. Kunes, "Microwave multiplexers for space applications," *Electron. Commun. Eng. J.*, vol. 10, no. 1, pp. 29–35, Feb. 1998, doi: 10.1049/ecej:19980104.
[31] K. G. H. Leng, Z. Shen, and A. Khong, "A new probe-excited dual-mode cavity filter," *Microw. Opt. Technol. Lett.*, vol. 38, no. 4, pp. 335–337, 2003, doi: 10.1002/mop.11053.
[32] L. Accatino, "Elliptical cavity resonators for dual-mode narrow-band filters," *IEEE Trans. Microw. Theory Tech.*, vol. 45, no. 12 PART 2, pp. 2393–2401, 1997, doi: 10.1109/22.643850.
[33] H. Hu, K. L. Wu, and R. J. Cameron, "Stepped circular waveguide dual-mode filters for broadband contiguous multiplexers," *IEEE Trans. Microw. Theory Tech.*, vol. 61, no. 1, pp. 139–145, 2013, doi: 10.1109/TMTT.2012.2227787.
[34] A. E. Williams and A. E. Atia, "Generalized TE/sub 011/ Mode Waveguide Bandpass Filters," in *MTT-S International Microwave Symposium Digest*, MTT005, 1975, pp. 60–62. doi: 10.1109/MWSYM.1975.1123280.
[35] A. E. Atia and A. E. Williams, "General TE/sub 011/-Mode Waveguide Bandpass Filters," *IEEE Trans. Microw. Theory Tech.*, vol. 24, no. 10, pp. 640–648, Oct. 1976, doi: 10.1109/TMTT.1976.1128929.
[36] C. A. and J. P. J. Nowak, J. Lorente, "A Generic Approach for Output Multiplexer Design," in *7th ESA Workshop on Microwave Filters*, Noordwijk Netherlands, 2018.
[37] H. L. Thal, "Cylindrical TE/sub 011/ /TM/sub 111/ Mode Control by Cavity Shaping," *IEEE Trans. Microw. Theory Tech.*, vol. 27, no. 12, pp. 982–986, Dec. 1979, doi: 10.1109/TMTT.1979.1129777.
[38] D. E. Kreinheder and T. D. Lingren, "Improved Selectivity in Cylindrical TE/sub 011/ Filters by TE/sub 211/TE/sub 311/ Mode Control," *IEEE Trans. Microw. Theory Tech.*, vol. 30, no. 9, pp. 1383–1387, 1982, doi: 10.1109/TMTT.1982.1131265.
[39] A. Melloni, M. Politi, G. G. Gentili, and G. Macchiarella, "Field Design of TE011-Mode Wavegude Passband Filters," in *22nd European Microwave Conference, 1992*, IEEE, Oct. 1992, pp. 533–538. doi: 10.1109/EUMA.1992.335760.
[40] J. D. Rhodes and R. J. Cameron, "General Extracted Pole Synthesis Technique with Applications to

Low-Loss TE011 Mode Filters," *IEEE Trans. Microw. Theory Tech.*, vol. 28, no. 9, pp. 1018–1028, Sep. 1980, doi: 10.1109/TMTT.1980.1130213.
[41] R. J. Cameron, H. Gregg, C. J. Radcliffe, and J. D. Rhodes, "Extracted-Pole Filter Manifold Multiplexing," *IEEE Trans. Microw. Theory Tech.*, vol. 30, no. 7, pp. 1041–1050, 1982, doi: 10.1109/TMTT.1982.1131195.
[42] Y. Yang, M. Yu, and Q. Wu, "Advanced synthesis technique for unified extracted pole filters," *IEEE Trans. Microw. Theory Tech.*, vol. 64, no. 12, pp. 4463–4472, 2016, doi: 10.1109/TMTT.2016.2623618.
[43] Y. Yang, M. Yu, Q. Wu, X. Yin, and J. Yang, "A fully integrated multiplexer using unified extracted pole technique," *IEEE Trans. Microw. Theory Tech.*, vol. 68, no. 8, pp. 3439–3447, 2020, doi: 10.1109/TMTT.2020.2996246.
[44] H. E. King, "Rectangular Waveguide Theoretical CW Average Power Rating," *IEEE Trans. Microw. Theory Tech.*, vol. 9, no. 4, pp. 349–357, Jul. 1961, doi: 10.1109/TMTT.1961.1125342.
[45] C. Kudsia, R. Cameron, and W.-C. Tang, "Innovations in microwave filters and multiplexing networks for communications satellite systems," *IEEE Trans. Microw. Theory Tech.*, vol. 40, no. 6, pp. 1133–1149, Jun. 1992, doi: 10.1109/22.141345.
[46] M. Yu, "Power-handling capability for RF filters," *IEEE Microw. Mag.*, vol. 8, no. 5, pp. 88–97, Oct. 2007, doi: 10.1109/MMM.2007.904712.
[47] V. Singh, P. K. Ambati, S. Soni, and K. Karthik, "Enhancing Satellite Communications: Temperature-Compensated Filters and Their Application in Satellite Technology," *IEEE Microw. Mag.*, vol. 20, no. 3, pp. 46–63, 2019, doi: 10.1109/MMM.2018.2885674.
[48] I. Arregui *et al.*, "High-Power Filter Design in Waveguide Technology: Future Generation of Waveguide Satellite Filters in Payloads Handling Increasing Bit Rates and Numbers of Channels," *IEEE Microw. Mag.*, vol. 21, no. 6, pp. 46–57, 2020, doi: 10.1109/MMM.2020.2979154.
[49] R. CHAPMAN, J. ROOTSEY, I. POLIDI, and W. DAVISON, "Hidden threat - Multicarrier passive component IM generation," in *6th Communications Satellite Systems Conference*, Reston, Virigina: American Institute of Aeronautics and Astronautics, Apr. 1976. doi: 10.2514/6.1976-296.
[50] W.-C. Tang and C. M. Kudsia, "Multipactor breakdown and passive intermodulation in microwave equipment for stellite applications," in *IEEE Conference on Military Communications*, IEEE, 1990, pp. 181–187. doi: 10.1109/MILCOM.1990.117409.
[51] J. Sombrin, I. Albert, and G. Soubercaze-Pun, "Multicarrier Passive Inter-Modulation Prediction from 2-Carrier Measurements," in *31st AIAA International Communications Satellite Systems Conference*, Reston, Virginia: American Institute of Aeronautics and Astronautics, Oct. 2013, pp. 7823–7830. doi: 10.2514/6.2013-5674.
[52] European Space Agency, "Multipactor handbook," European Cooperation for Space Standardisation ESA-ESTEC Document,ECSS-E-HB-20-01A, 2020.
[53] M. A. Herlin and S. C. Brown, "Breakdown of a Gas at Microwave Frequencies," *Phys. Rev.*, vol. 74, no. 3, pp. 291–296, Aug. 1948, doi: 10.1103/PhysRev.74.291.
[54] R. A. Kishek, Y. Y. Lau, L. K. Ang, A. Valfells, and R. M. Gilgenbach, "Multipactor discharge on metals and dielectrics: Historical review and recent theories," *Phys. Plasmas*, vol. 5, no. 5, pp. 2120–2126, May 1998, doi: 10.1063/1.872883.
[55] A. J. Hatch and H. B. Williams, "The secondary electron resonance mechanism of low-pressure high-frequency gas breakdown," *J. Appl. Phys.*, vol. 25, no. 4, pp. 417–423, 1954, doi: 10.1063/1.1721656.
[56] J. R. M. Vaughan, "Multipactor," *IEEE Trans. Electron Devices*, vol. 35, no. 7, pp. 1172–1180, Jul. 1988, doi: 10.1109/16.3387.
[57] A. D. MacDonald, *Microwave Breakdown in Gases*. in Wiley series in plasma physics. Wiley, 1966. [Online]. Available: https://books.google.co.uk/books?id=NcI8AAAAIAAJ

[58] D. Anderson, “Microwave breakdown in resonators and filters,” *IEEE Trans. Microw. Theory Tech.*, vol. 47, no. 12, pp. 2547–2556, 1999, doi: 10.1109/22.809005.
[59] J. Puech *et al.*, “Microwave discharge research activities within the contest of the Chalmers University (Sweden)/Institute of Applied Physics (Russia)/CNES (France) project,” in *Proc. 4th Int. Workshop on Multipactor, Corona and Passive Intermodulation in Space RF Hardware (MULCOPIM 2003)*, 2003.
[60] U. Jordan *et al.*, “On the effective diffusion length for microwave breakdown,” *IEEE Trans. Plasma Sci.*, vol. 34, no. 2 III, pp. 421–430, 2006, doi: 10.1109/TPS.2006.872189.
[61] U. Jordan *et al.*, “Microwave Corona Breakdown Around Metal Corners and Wedges,” *IEEE Trans. Plasma Sci.*, vol. 35, no. 3, pp. 542–550, Jun. 2007, doi: 10.1109/TPS.2007.896987.
[62] T. Pinheiro-Ortega *et al.*, “Microwave corona breakdown prediction in arbitrarily-shaped waveguide based filters,” *IEEE Microw. Wirel. Components Lett.*, vol. 20, no. 4, pp. 214–216, 2010, doi: 10.1109/LMWC.2010.2042555.
[63] A. Gill, EWB and Von Engel, “Starting potentials of high-frequency gas discharges at low pressure,” *Proc. R. Soc. London. Ser. A. Math. Phys. Sci.*, vol. 192, no. 1030, pp. 446–463, Feb. 1948, doi: 10.1098/rspa.1948.0018.
[64] J. R. M. Vaughan, “Multipactor,” *IEEE Trans. Electron Devices*, vol. 35, no. 7, pp. 1172–1180, Jul. 1988, doi: 10.1109/16.3387.
[65] S. Anza *et al.*, “Multipactor theory for multicarrier signals,” *Phys. Plasmas*, vol. 18, no. 3, 2011, doi: 10.1063/1.3561821.
[66] S. Anza *et al.*, “Prediction of multipactor breakdown for multicarrier applications: The quasi-stationary method,” *IEEE Trans. Microw. Theory Tech.*, vol. 60, no. 7, pp. 2093–2105, 2012, doi: 10.1109/TMTT.2012.2197021.
[67] S. Anza, C. Vicente, J. Gil, V. E. Boria, B. Gimeno, and D. Raboso, “Nonstationary statistical theory for multipactor,” *Phys. Plasmas*, vol. 17, no. 6, p. 062110, Jun. 2010, doi: 10.1063/1.3443128.
[68] E. Sorolla, M. Belhaj, J. Sombrin, and J. Puech, “New multipactor dynamics in presence of dielectrics,” *Phys. Plasmas*, vol. 24, no. 10, p. 103508, 2017.
[69] T. P. Graves, “Standard/handbook for radio frequency (RF) breakdown prevention in spacecraft components,” *Rep. NO. TOR-2014-02198*, 2014.
[70] C. K. Birdsall and A. B. Langdon, *Plasma Physics via Computer Simulation*. in Series in Plasma Physics and Fluid Dynamics. Taylor & Francis, 2004. [Online]. Available: https://books.google.co.uk/books?id=S2lqgDTm6a4C
[71] S. Anza, C. Vicente, D. Raboso, J. Gil, B. Gimeno, and V. E. Boria, “Enhanced prediction of multipaction breakdown in passive waveguide components including space charge effects,” *IEEE MTT-S Int. Microw. Symp. Dig.*, pp. 1095–1098, 2008, doi: 10.1109/MWSYM.2008.4633247.
[72] G. Burt, R. G. Carter, A. C. Dexter, B. Hall, J. D. A. Smith, and P. Goudket, “Benchmarking Simulations of Multipactor in Rectangular Waveguides Using {CST}-Particle Studio,” *Proc. SRF2009*, p. oo, 2009.
[73] G. Salza *et al.*, “Helical resonator filters with improved multipactor performance exploiting rigorous modelling and the large gap approach,” *IET Microwaves, Antennas Propag.*, vol. 13, no. 10, pp. 1756–1759, 2019, doi: 10.1049/iet-map.2019.0245.
[74] F. De Paolis and C. Ernst, “Challenges in the design of next generation ka-band OMUX for space applications,” *31st AIAA Int. Commun. Satell. Syst. Conf. ICSSC 2013*, no. October 2013, pp. 1–7, 2013, doi: 10.2514/6.2013-5694.
[75] M. Lisi, “A review of temperature compensation techniques for microwave resonators and filters,” in *Proceedings of the Micro and Millimetre Wave Technology and Techniques Workshop*, 2014.
[76] C. Kudsia, T. Stajcer, and M. Yu, “Evolution of Microwave Technologies for Communications Satellite Systems,” in *34th AIAA International Communications Satellite Systems Conference*,

Reston, Virginia: American Institute of Aeronautics and Astronautics, Oct. 2016. doi: 10.2514/6.2016-5739.
[77] A. E. Atia, "A 14-GHz High-Power Filter," in *MTT-S International Microwave Symposium Digest*, MTT005, 1979, pp. 261–261. doi: 10.1109/MWSYM.1979.1124037.
[78] C. M. Kudsia, J. Dorey, J. Heierli, K. R. Ainsworth, and G. J. P. Lo, "A New Type of Low Loss l4 GHz High Power Combining Network for Satellite Earth Terminals," in *9th European Microwave Conference, 1979*, IEEE, Oct. 1979, pp. 386–391. doi: 10.1109/EUMA.1979.332734.
[79] D. J. Rosowsky and D. Wolk, "A 450-W Output Multiplexer for Direct Broadcasting Satellites," *IEEE Trans. Microw. Theory Tech.*, vol. 30, no. 9, pp. 1317–1323, 1982, doi: 10.1109/TMTT.1982.1131254.
[80] P. Martin-Iglesias *et al.*, "Evaluation of High Performance Aluminum for Microwave Filters," *IEEE MTT-S Int. Microw. Symp. Dig.*, vol. 2019-June, pp. 1183–1186, 2019, doi: 10.1109/mwsym.2019.8700938.
[81] P. Martin-Iglesias *et al.*, "Multiphysic Analysis of High Power Microwave Filter Using High Performance Aluminium Alloy," in *2019 IEEE MTT-S International Microwave Workshop Series on Advanced Materials and Processes for RF and THz Applications (IMWS-AMP)*, IEEE, Jul. 2019, pp. 58–60. doi: 10.1109/IMWS-AMP.2019.8880080.
[82] C. M. Kudsia and M. V. O'Donovan, "A Light Weight Graphite Fiber Epoxy Composite (GFEC) Waveguide Multiplexer for Satellite Application," in *4th European Microwave Conference, 1974*, IEEE, Oct. 1974, pp. 585–589. doi: 10.1109/EUMA.1974.331987.
[83] S. Liberatoscioli, M. Mattes, M. Guglielmi, D. Schmitt, and C. Ernst, "Innovative manufacturing technology for RF Passive devices combining electroforming and CFRP application," in *2008 IEEE MTT-S International Microwave Symposium Digest*, IEEE, Jun. 2008, pp. 743–746. doi: 10.1109/MWSYM.2008.4632939.
[84] Chi Wang and K. A. Zaki, "Temperature compensation of combline resonators and filters," in *1999 IEEE MTT-S International Microwave Symposium Digest (Cat. No.99CH36282)*, IEEE, 1999, pp. 1041–1044. doi: 10.1109/MWSYM.1999.779566.
[85] G. L. Burnett and G. I. Tsuda, "Temperature compensated microwave filter," US4112398A, 1978 [Online]. Available: https://patents.google.com/patent/US4112398A/en?oq=us4%2C112%2C398
[86] R. G. Thomson, "Collapsible pocket for changing the operating frequency of a microwave filter and a filter using the device," US6049261A, 2000 [Online]. Available: https://patents.google.com/patent/US6049261A/en?oq=US6049261
[87] W.-C. Tang, "Multi-mode temperature compensated filters and a method of constructing and compensating therefor," US5589807A, 1996 [Online]. Available: https://patents.google.com/patent/US5589807A/en?oq=US5%2C589%2C807
[88] B. F. Keats, R. B. Gorbet, and R. R. Mansour, "Design and testing of SMA temperature-compensated cavity resonators," *IEEE Trans. Microw. Theory Tech.*, vol. 51, no. 12, pp. 2284–2289, 2003, doi: 10.1109/TMTT.2003.820166.
[89] H. W. Yao and A. E. Atia, "Temperature characteristics of combline resonators and filters," in *IEEE MTT-S International Microwave Symposium Digest*, 2001, pp. 1475–1478. doi: 10.1109/mwsym.2001.967181.
[90] J. Müller and M. Höft, "Temperature compensation of resonators using different materials and suitable dimensions," in *35th European Microwave Conference 2005 - Conference Proceedings*, 2005, pp. 685–688. doi: 10.1109/EUMC.2005.1608949.
[91] R. Tkadlec, F. Hrnicko, and G. Toth, "Method for compensating a temperature drift of a microwave filter," US10199704B2, 2019 [Online]. Available: https://patents.google.com/patent/US10199704B2/en?oq=us10199704+B2
[92] A. E. Atia and A. E. Williams, "Temperature Compensation of TE 011-Mode Circular Cavities,"

IEEE Trans. Microw. Theory Tech., vol. 24, no. 10, pp. 668–669, Oct. 1976, doi: 10.1109/TMTT.1976.1128935.
[93] R. V. Basil, J. L. Ondrups, and J. K. Shimizu, "Thermally compensated microwave resonator," US4057772A, 1977 [Online]. Available: https://patents.google.com/patent/US4057772A/en?oq=us4057772
[94] Rolf Kich, "Temperature compensated microwave resonator," US4677403A, 1987 [Online]. Available: https://patents.google.com/patent/US4677403A/en?oq=us4%2C677%2C403
[95] R. E. Jachowski and L. E. Brown, "Internal bi-metallic temperature compensating device for tuned cavities," US4423398A, 1983 [Online]. Available: https://patents.google.com/patent/US4423398A/en?oq=us4%2C423%2C398
[96] H. Schmid and L. R. Mannerstrom, "Temperature-compensated tuning screw for cavity filters," US5039966A, 1991
[97] B. L. Steven, "Temperature compensated microwave filter," US5867077A, 1999 [Online]. Available: https://patents.google.com/patent/US5867077A/en?oq=US5867077A
[98] D. J. Temperature compensated high power bandpass filterSmall and J. A., "Temperature compensated high power bandpass filter," US6232852B1, 2001 [Online]. Available: https://patents.google.com/patent/US6232852B1/en?oq=US6232852B1
[99] D. Wolk, J. Damaschke, and D. Schmitt, "Frequency-stabilized waveguide arrangement," US6433656B1, 2002 [Online]. Available: https://patents.google.com/patent/US6433656B1/en?oq=US6433656
[100] D. J. Small and J. A. Lunn, "Temperature compensated high power bandpass filter," US6529104B1, 2003 [Online]. Available: https://patents.google.com/patent/US6529104B1/en?oq=US6529104B1
[101] F. William, M. Yu, D. Smith, and A. Sivadas, "Microwave resonator having an external temperature compensator," US6535087B1, 2003 [Online]. Available: https://patents.google.com/patent/US6535087B1/en?oq=US6535087
[102] I. Gibson, D. Rosen, and B. Stucker, *Additive Manufacturing Technologies: 3D Printing, Rapid Prototyping, and Direct Digital Manufacturing*. Springer New York, 2016. [Online]. Available: https://books.google.co.uk/books?id=9NxjvgAACAAJ
[103] U. ISO, "Additive manufacturing, general principles, terminology," *Iso/Astm 52900*, pp. 1–26, 2015.
[104] W. J. Chappell, C. Reilly, J. Halloran, and L. P. B. Katehi, "Ceramic synthetic substrates using solid freeform fabrication," *IEEE Trans. Microw. Theory Tech.*, vol. 51, no. 3, pp. 752–760, 2003, doi: 10.1109/TMTT.2003.808727.
[105] B. Liu, X. Gong, and W. J. Chappell, "Applications of layer-by-layer polymer stereolithography for three-dimensional high-frequency components," *IEEE Trans. Microw. Theory Tech.*, vol. 52, no. 11, pp. 2567–2575, 2004, doi: 10.1109/TMTT.2004.837165.
[106] X. Gong *et al.*, "Precision fabrication techniques and analysis on high-Q evanescent-mode resonators and filters of different geometries," *IEEE Trans. Microw. Theory Tech.*, vol. 52, no. 11, pp. 2557–2566, 2004.
[107] L. Schulwitz and A. Mortazawi, "A compact dual-polarized multibeam phased-array architecture for millimeter-wave radar," in *IEEE Transactions on Microwave Theory and Techniques*, Nov. 2005, pp. 3588–3594. doi: 10.1109/TMTT.2005.857104.
[108] L. Schulwitz and A. Mortazawi, "Millimeter-Wave Dual Polarized L-Shaped Horn Antenna for Wide-Angle Phased Arrays," *IEEE Trans. Antennas Propag.*, vol. 54, no. 9, pp. 2663–2668, Sep. 2006, doi: 10.1109/TAP.2006.880761.
[109] A. Buerkle, K. F. Brakora, and K. Sarabandi, "Fabrication of a DRA array using ceramic stereolithography," *IEEE Antennas Wirel. Propag. Lett.*, vol. 5, no. 1, pp. 479–482, 2006, doi: 10.1109/LAWP.2006.885167.
[110] K. F. Brakora, J. Halloran, and K. Sarabandi, "Design of 3-D monolithic MMW antennas using

ceramic stereolithography," *IEEE Trans. Antennas Propag.*, vol. 55, no. 3 II, pp. 790–797, 2007, doi: 10.1109/TAP.2007.891855.
[111] K. F. Brakora and K. Sarabandi, "Integration of single-mode photonic crystal clad waveguides with monolithically constructed ceramic subsystems," *IEEE Antennas Wirel. Propag. Lett.*, vol. 8, pp. 433–436, 2009, doi: 10.1109/LAWP.2008.2007991.
[112] M. D'Auria *et al.*, "3-D Printed Metal-Pipe Rectangular Waveguides," *IEEE Trans. Components, Packag. Manuf. Technol.*, vol. 5, no. 9, pp. 1339–1349, 2015, doi: 10.1109/TCPMT.2015.2462130.
[113] G. Addamo *et al.*, "Experimental research activity on additive manufacturing of microwave passive waveguide components," *Eur. Microw. Week 2017 "A Prime Year a Prime Event", EuMW 2017 - Conf. Proceedings; 47th Eur. Microw. Conf. EuMC 2017*, vol. 2017-Janua, pp. 496–499, 2017, doi: 10.23919/EuMC.2017.8230898.
[114] C. Tomassoni, O. A. Peverini, G. Venanzoni, G. Addamo, F. Paonessa, and G. Virone, "3D Printing of Microwave and Millimeter-Wave Filters: Additive Manufacturing Technologies Applied in the Development of High-Performance Filters with Novel Topologies," *IEEE Microw. Mag.*, vol. 21, no. 6, pp. 24–45, Jun. 2020, doi: 10.1109/MMM.2020.2979153.
[115] R. V. Snyder, G. Macchiarella, S. Bastioli, and C. Tomassoni, "Emerging Trends in Techniques and Technology as Applied to Filter Design," *IEEE J. Microwaves*, vol. 1, no. 1, pp. 317–344, 2021, doi: 10.1109/jmw.2020.3028643.
[116] G. Addamo *et al.*, "3-d printing of high-performance feed horns from Ku-to V-bands," *IEEE Antennas Wirel. Propag. Lett.*, vol. 17, no. 11, pp. 2036–2040, 2018, doi: 10.1109/LAWP.2018.2859828.
[117] T.-H. Chio, G.-L. Huang, and S.-G. Zhou, "Application of Direct Metal Laser Sintering to Waveguide-Based Passive Microwave Components, Antennas, and Antenna Arrays," *Proc. IEEE*, vol. 105, no. 4, pp. 632–644, 2016, doi: 10.1109/jproc.2016.2617870.
[118] M. Kilian, C. Hartwanger, M. Schneider, and M. Hatzenbichler, "Waveguide components for space applications manufactured by additive manufacturing technology," *IET Microwaves, Antennas Propag.*, vol. 11, no. 14, pp. 1949–1954, 2017, doi: 10.1049/iet-map.2016.0984.
[119] G. Addamo *et al.*, "3D Printing of a Monolithic K/Ka-Band Dual-Circular Polarization Antenna-Feeding Network," *IEEE Access*, vol. 9, pp. 88243–88255, 2021, doi: 10.1109/ACCESS.2021.3089826.
[120] R. Sorrentino and O. A. Peverini, "Additive manufacturing: A key enabling technology for next-generation microwave and millimeter-wave systems [point of view]," *Proc. IEEE*, vol. 104, no. 7, pp. 1362–1366, 2016, doi: 10.1109/JPROC.2016.2577327.
[121] R. Sorrentino, P. Martin-Iglesias, O. A. Peverini, and T. M. Weller, "Additive Manufacturing of Radio-Frequency Components [Scanning the Issue]," *Proc. IEEE*, vol. 105, no. 4, pp. 589–592, 2017, doi: 10.1109/jproc.2017.2670298.
[122] S. S. Crump, "Apparatus and method for creating three-dimensional objects," US5121329A, 1992 [Online]. Available: https://patents.google.com/patent/US5121329A/en?inventor=Scott+Crump&before=priority:19891231&after=priority:19890101&oq=Scott+Crump+1989
[123] C. W. Hull, "Apparatus for Production of Three-Dmensonal Objects By Stereo Thography," US4575330A, 1986 [Online]. Available: https://patents.google.com/patent/US4575330A/en?oq=us4575330A
[124] C. R. Deckard, "Method and apparatus for producing parts by selective sintering," US4863538A, 1989 [Online]. Available: https://patents.google.com/patent/US4863538A/en?oq=US4863538A
[125] G. Addamo *et al.*, "Additive manufacturing of ka-band dual-polarization waveguide components," *IEEE Trans. Microw. Theory Tech.*, vol. 66, no. 8, pp. 3589–3596, 2018, doi: 10.1109/TMTT.2018.2854187.

[126] O. A. Peverini, M. Lumia, G. Addamo, G. Virone, and N. J. G. Fonseca, "How 3D-Printing Is Changing RF Front-End Design for Space Applications," *IEEE J. Microwaves*, vol. 3, no. 2, pp. 1–15, Apr. 2023, doi: 10.1109/jmw.2023.3250343.
[127] M. Lumia, G. Addamo, O. Antonio Peverini, F. Calignano, G. Virone, and D. Manfredi, "Additive Manufacturing of RF Waveguide Components," in *Recent Microwave Technologies*, vol. 11, no. tourism, IntechOpen, 2022, p. 13. doi: 10.5772/intechopen.104106.
[128] T. Skaik *et al.*, "Evaluation of 3D Printed Monolithic G-band Waveguide Components," *IEEE Trans. Components, Packag. Manuf. Technol.*, vol. 13, no. 2, pp. 240–248, 2023, doi: 10.1109/TCPMT.2023.3243002.
[129] M. Dionigi, C. Tomassoni, G. Venanzoni, and R. Sorrentino, "Simple High-Performance Metal-Plating Procedure for Stereolithographically 3-D-Printed Waveguide Components," *IEEE Microw. Wirel. Components Lett.*, vol. 27, no. 11, pp. 953–955, 2017, doi: 10.1109/LMWC.2017.2750090.
[130] X. Shang *et al.*, "W-Band Waveguide Filters Fabricated by Laser Micromachining and 3-D Printing," *IEEE Trans. Microw. Theory Tech.*, vol. 64, no. 8, pp. 2572–2580, 2016, doi: 10.1109/TMTT.2016.2574839.
[131] J. R. Montejo-Garai, I. O. Saracho-Pantoja, C. A. Leal-Sevillano, J. A. Ruiz-Cruz, and J. M. Rebollar, "Design of microwave waveguide devices for space and ground application implemented by additive manufacturing," in *2015 International Conference on Electromagnetics in Advanced Applications (ICEAA)*, IEEE, Sep. 2015, pp. 325–328. doi: 10.1109/ICEAA.2015.7297128.
[132] R. Dahle, P. Laforge, and J. Kuhling, "3-D printed customizable inserts for waveguide filter design at X-band," *IEEE Microw. Wirel. Components Lett.*, vol. 27, no. 12, pp. 1080–1082, 2017, doi: 10.1109/LMWC.2017.2754345.
[133] D. Miek, S. Simmich, and M. Hoft, "Additive Manufacturing of Symmetrical X-Band Waveguide Filters for Wide-Band Applications based on Extracted Pole Filter Design," *IMWS-AMP 2019 - 2019 IEEE MTT-S Int. Microw. Work. Ser. Adv. Mater. Process. RF THz Appl.*, pp. 13–15, 2019, doi: 10.1109/IMWS-AMP.2019.8880120.
[134] B. Al-Juboori *et al.*, "Lightweight and Low-Loss 3-D Printed Millimeter-Wave Bandpass Filter Based on Gap-Waveguide," *IEEE Access*, vol. 7, pp. 2624–2632, 2019, doi: 10.1109/ACCESS.2018.2886210.
[135] C. Guo, X. Shang, M. J. Lancaster, and J. Xu, "A 3-D Printed Lightweight X-Band Waveguide Filter Based on Spherical Resonators," *IEEE Microw. Wirel. Components Lett.*, vol. 25, no. 7, pp. 442–444, 2015, doi: 10.1109/LMWC.2015.2427653.
[136] C. Guo, X. Shang, J. Li, F. Zhang, M. J. Lancaster, and J. Xu, "A Lightweight 3-D Printed X-Band Bandpass Filter Based on Spherical Dual-Mode Resonators," *IEEE Microw. Wirel. Components Lett.*, vol. 26, no. 8, pp. 568–570, 2016, doi: 10.1109/LMWC.2016.2587838.
[137] C. Guo, J. Li, D. D. Dinh, X. Shang, M. J. Lancaster, and J. Xu, "Ceramic filled resin based 3D printed X-band dual-mode bandpass filter with enhanced thermal handling capability," *Electron. Lett.*, vol. 52, no. 23, pp. 1929–1931, 2016, doi: 10.1049/el.2016.2955.
[138] F. Zhang *et al.*, "3-D Printed Slotted Spherical Resonator Bandpass Filters with Spurious Suppression," *IEEE Access*, vol. 7, pp. 128026–128034, 2019, doi: 10.1109/ACCESS.2019.2938972.
[139] J. Li, C. Guo, L. Mao, J. Xiang, G. L. Huang, and T. Yuan, "Monolithically 3-D Printed Hemispherical Resonator Waveguide Filters with Improved Out-of-Band Rejections," *IEEE Access*, vol. 6, pp. 57030–57048, 2018, doi: 10.1109/ACCESS.2018.2872696.
[140] A. Perigaud, O. Tantot, N. Delhote, S. Bila, S. Verdeyme, and D. Baillargeat, "Continuously tunable filter made by additive manufacturing using a 3D spiral ribbon," *2017 IEEE MTT-S Int. Microw. Work. Ser. Adv. Mater. Process. RF THz Appl. IMWS-AMP 2017*, vol. 2018-Janua, no. September, pp. 1–3, 2018, doi: 10.1109/IMWS-AMP.2017.8247372.
[141] L. S. Araujo *et al.*, "3-D printed band-pass combline filter," *Microw. Opt. Technol. Lett.*, vol. 59, no.

6, pp. 1388–1390, Jun. 2017, doi: 10.1002/mop.30547.
[142] C. Tomassoni, G. Venanzoni, M. Dionigi, and R. Sorrentino, “Compact quasi-elliptic filters with mushroom-shaped resonators manufactured with 3-d Printer,” *IEEE Trans. Microw. Theory Tech.*, vol. 66, no. 8, pp. 3579–3588, 2018, doi: 10.1109/TMTT.2018.2849067.
[143] G. Venanzoni, M. Dionigi, C. Tomassoni, and R. Sorrentino, “3-D-Printed Quasi-Elliptical Evanescent Mode Filter Using Mixed Electromagnetic Coupling,” *IEEE Microw. Wirel. Components Lett.*, vol. 28, no. 6, pp. 497–499, 2018, doi: 10.1109/LMWC.2018.2829627.
[144] E. Lopez-Oliver *et al.*, “3-D-Printed Compact Bandpass Filters Based on Conical Posts,” *IEEE Trans. Microw. Theory Tech.*, vol. 69, no. 1, pp. 616–628, 2020, doi: 10.1109/tmtt.2020.3035168.
[145] G. Venanzoni, C. Tomassoni, M. DIonigi, M. Mongiardo, and R. Sorrentino, “Design and Fabrication of 3-D Printed Inline Coaxial Filters with Improved Stopband,” *IEEE Trans. Microw. Theory Tech.*, vol. 68, no. 7, pp. 2633–2643, 2020, doi: 10.1109/TMTT.2020.2988244.
[146] X. Shang, J. Li, C. Guo, M. J. Lancaster, and J. Xu, “3-D printed filter based on helical resonators with variable width,” *IEEE MTT-S Int. Microw. Symp. Dig.*, pp. 1587–1590, 2017, doi: 10.1109/MWSYM.2017.8058936.
[147] C. Tomassoni, R. Bahr, M. Tentzeris, M. Bozzi, and L. Perregrini, “3D printed substrate integrated waveguide filters with locally controlled dielectric permittivity,” in *2016 46th European Microwave Conference (EuMC)*, IEEE, Oct. 2016, pp. 253–256. doi: 10.1109/EuMC.2016.7824326.
[148] M. T. Craton, J. Sorocki, I. Piekarz, S. Gruszczynski, K. Wincza, and J. Papapolymerou, “Realization of Fully 3D Printed W-Band Bandpass Filters Using Aerosol Jet Printing Technology,” *2018 48th Eur. Microw. Conf. EuMC 2018*, pp. 1013–1016, 2018, doi: 10.23919/EuMC.2018.8541416.
[149] J. A. Lorente, M. M. Mendoza, A. Z. Petersson, L. Pambaguian, A. A. Melcon, and C. Ernst, “Single part microwave filters made from selective laser melting,” in *2009 European Microwave Conference (EuMC)*, IEEE, Sep. 2009, pp. 1421–1424. doi: 10.23919/EUMC.2009.5296127.
[150] P. Booth and E. V. Lluch, “Enhancing the Performance of Waveguide Filters Using Additive Manufacturing,” *Proc. IEEE*, vol. 105, no. 4, pp. 613–619, 2016, doi: 10.1109/jproc.2016.2616494.
[151] P. A. Booth and E. Valles Lluch, “Realising advanced waveguide bandpass filters using additive manufacturing,” *IET Microwaves, Antennas Propag.*, vol. 11, no. 14, pp. 1943–1948, 2017, doi: 10.1049/iet-map.2017.0170.
[152] S. W. Sattler, F. Gentili, R. Teschl, and W. Bosch, “Direct Metal Printed 4th order Stepped Impedance Filter in the C/X Band,” in *2018 IEEE/MTT-S International Microwave Symposium - IMS*, IEEE, Jun. 2018, pp. 145–148. doi: 10.1109/MWSYM.2018.8439567.
[153] O. A. Peverini *et al.*, “Enhanced topology of E-plane resonators for high-power satellite applications,” *IEEE Trans. Microw. Theory Tech.*, vol. 63, no. 10, pp. 3361–3373, 2015, doi: 10.1109/TMTT.2015.2462839.
[154] O. A. Peverini *et al.*, “Selective laser melting manufacturing of microwave waveguide devices,” *Proc. IEEE*, vol. 105, no. 4, pp. 620–631, 2017, doi: 10.1109/JPROC.2016.2620148.
[155] O. A. Peverini *et al.*, “Additive manufacturing of Ku/K-band waveguide filters: A comparative analysis among selective-laser melting and stereolithography,” *IET Microwaves, Antennas Propag.*, vol. 11, no. 14, pp. 1–7, 2017, doi: 10.1049/iet-map.2017.0151.
[156] E. A. Rojas-Nastrucci, J. T. Nussbaum, N. B. Crane, and T. M. Weller, “Ka-Band Characterization of Binder Jetting for 3-D Printing of Metallic Rectangular Waveguide Circuits and Antennas,” *IEEE Trans. Microw. Theory Tech.*, vol. 65, no. 9, pp. 3099–3108, 2017, doi: 10.1109/TMTT.2017.2730839.
[157] B. Zhang and H. Zirath, “3D printed iris bandpass filters for millimetre-wave applications,” *Electron. Lett.*, vol. 51, no. 22, pp. 1791–1793, 2015, doi: 10.1049/el.2015.2342.
[158] M. Salek *et al.*, “W-Band Waveguide Bandpass Filters Fabricated by Micro Laser Sintering,” *IEEE Trans. Circuits Syst. II Express Briefs*, vol. 66, no. 1, pp. 61–65, 2019, doi:

10.1109/TCSII.2018.2824898.
[159] Y. Yu *et al.*, “D-Band Waveguide Diplexer Fabricated Using Micro Laser Sintering,” *IEEE Trans. Components, Packag. Manuf. Technol.*, vol. 12, no. 9, pp. 1446–1457, 2022, doi: 10.1109/TCPMT.2022.3204887.
[160] T. Skaik *et al.*, “A 3-D Printed 300 GHz Waveguide Cavity Filter by Micro Laser Sintering,” *IEEE Trans. Terahertz Sci. Technol.*, vol. 12, no. 3, pp. 274–281, 2022, doi: 10.1109/TTHZ.2022.3147042.
[161] T. Skaik *et al.*, “A300 GHz Waveguide Cavity Filter Fabricated by 3D Screen Printing Technology,” *2022 52nd Eur. Microw. Conf. EuMC 2022*, pp. 302–305, 2022, doi: 10.23919/EuMC54642.2022.9924503.
[162] N. Delhote, D. Baillargeat, S. Verdeyme, C. Delage, and C. Chaput, “Ceramic layer-by-layer stereolithography for the manufacturing of 3-D millimeter-wave filters,” *IEEE Trans. Microw. Theory Tech.*, vol. 55, no. 3, pp. 548–554, 2007, doi: 10.1109/TMTT.2007.891690.
[163] Y. Marchives, N. Delhote, S. Verdeyme, and P. M. Iglesias, “Wide-band dielectric filter at C-band manufactured by stereolithography,” *Eur. Microw. Week 2014 Connect. Futur. EuMW 2014 - Conf. Proceedings; EuMC 2014 44th Eur. Microw. Conf.*, pp. 187–190, 2014, doi: 10.1109/EuMC.2014.6986401.
[164] A. Perigaud, O. Tantot, N. Delhote, S. Verdeyme, S. Bila, and D. Baillargeat, “Bandpass Filter Based on Skeleton-like Monobloc Dielectric Pucks Made by Additive Manufacturing,” *2018 48th Eur. Microw. Conf. EuMC 2018*, pp. 296–299, 2018, doi: 10.23919/EuMC.2018.8541710.
[165] C. Carceller, F. Gentili, D. Reichartzeder, W. Bösch, and M. Schwentenwein, “Development of monoblock TM dielectric resonator filters with additive manufacturing,” *IET Microwaves, Antennas Propag.*, vol. 11, no. 14, pp. 1992–1996, Nov. 2017, doi: 10.1049/iet-map.2016.1051.
[166] D. Miek *et al.*, “Ceramic Additive Manufactured Monolithic X-Shaped TM Dual-Mode Filter,” *IEEE J. Microwaves*, vol. 2, no. 3, pp. 496–506, 2022, doi: 10.1109/jmw.2022.3167250.
[167] A. Perigaud *et al.*, “Continuously Tuned Ku-Band Cavity Filter Based on Dielectric Perturbers Made by Ceramic Additive Manufacturing for Space Applications,” *Proc. IEEE*, vol. 105, no. 4, pp. 677–687, Apr. 2017, doi: 10.1109/JPROC.2017.2663104.

CHAPTER 3: A NARROW 3-D PRINTED INVAR SPHERICAL DUAL-MODE FILTER WITH HIGH THERMAL STABILITY FOR OMUXS

Lu Qian, Yi Wang, Sheng Li, Abd El-Moez A. Mohamed, Moataz M. Attallah, Talal Skaik, Paul Booth, Laurent Pambaguian, César Miquel España, and Petronilo Martín-Iglesias

Yi Wang suggested this work, planned, and supervised the entire study, and led the project. Lu Qian conceived the idea of this design and carried out the theoretical modelling, analysis and simulations, and performed the experiment, interpreted the data and wrote the manuscript. Paul Booth, Laurent Pambaguian, César Miquel España, and Petronilo Martín-Iglesias advised and provided guidance on this project. Sheng Li, Abd El-Moez A. Mohamed, Moataz M. Attallah and Talal Skaik assisted in the fabrication of this filter. All authors contributed to the writing of the paper and reviewed the manuscript.

This chapter is based on the following publication: A Narrowband 3-D Printed Invar Spherical Dual-Mode Filter With High Thermal Stability for OMUXs, which has been published in IEEE Transactions on Microwave Theory and Techniques., vol. 70, no. 4, pp. 2165–2173, Apr. 2022. Doi: 10.1109/TMTT.2022.3152795

Abstract

A 3-D printed narrowband bandpass filter based on spherical dual-mode resonators is presented in this chapter. It is designed for output multiplexers (OMUXs) using high-Q spherical dual-mode resonators. Realization is by laser powder bed fusion (L-PBF) technology of Invar alloy chosen for its low coefficient of thermal expansion (CTE). Using PBF circumvents the alloy's manufacturability issues associated with its hardness in machining and free forming. Compared with polymer-based vat photopolymerization technology, PBF allows for direct metal manufacture of complex monolithic microwave components with better thermal-mechanical properties and higher power-handling capability. Using Invar can further help achieve high temperature stability of the filter in high-power operation. To demonstrate the proposed solution, detailed thermal-RF test at different temperatures was carried out. The experimental results of a 0.47% fourth-order silver-plated Invar filter with two transmission zeros verify the design and manufacturing. An insertion loss of 1 dB and an effective temperature coefficient of less than 2 ppm/K were achieved.

Keywords: 3-D printing, high-power filter, Invar, novel materials, output multiplexer, spherical resonators.

3.1 Introduction

High-power filters and multiplexers for space applications require high temperature stability due to their large operation temperature ranges as well as the power-induced self-heating effect. Among these devices is the output multiplexer (OMUX), one of the most complex and specialized passive components, also with the most stringent requirement for temperature stability. This is partly because of the narrow channel bandwidth (e.g. 36 or 54 MHz in X and Ku band) and partly because of the tight frequency and distance spacing between the channels. In fact, contiguous channel configurations are not uncommon. This leaves almost no bandwidth margin to allow for any frequency drift. To achieve a sufficiently high temperature stability, there are two well established temperature compensation techniques. One is to build the filter using Invar material with very low coefficient of thermal expansion (CTE of 0.5~2.0 ppm/K) [1]. The other is to build the filter from the favorably light aluminum but using external compensation mechanisms to achieve effective thermal compensation [2]. This complicates the assembly. Despite the attractively low CTE, Invar is not an easy material to work with for its high density and hardness in machining. Moreover, some essential mechanical features such as the straps and brackets will degrade the thermal handling capacity of the channel filter [1]. In this work, a new alternative fabrication route for Invar-based filters is demonstrated using additive-manufacturing (AM).

Different from the conventional subtractive process, AM (known also as 3-D printing) offers the flexibility and capability by selectively building material in layer-upon-layer fashion to form complex geometries monolithically, which is either impossible or too complicated for conventional machining [3]–[5]. When using INVAR, design could be geared toward higher RF performances and reduce cost for machining. AM also provides more design freedom for multi-objective topological optimization of the weight, mechanical and thermal properties. In this work, we will demonstrate a filter with spherical resonators, conformal cavity walls and modified flanges, built in one single piece using laser powder bed fusion (L-PBF) process from Invar powders. More specifically, the selective laser melting (SLM) technique is employed.

Most of the OMUX channel filters are implemented using dual-mode resonators for compactness and ease of layout especially when the channel number is high [6]. Among them, cylindrical high-Q TE_{11N} dual-mode resonators are the most widely used [7], [8]. However, they are normally manufactured cavity-by-cavity or in a split-block fashion. The separate cavities and the split-blocks require extra flanges and screws for assembly. Using AM, one can manufacture not only the Invar filters but also the attached mechanical features (such as brackets and straps) monolithically, with no or reduced interconnection and assembly. This can further translate to reduced mass and less passive intermodulation when the devices work with multiple carriers. In addition, unconventional geometric features are made possible by AM, such as: self-supportive spherical or elliptic cavities for enhanced RF performance, rounded corners for reduced field concentration and ease of plating, and waffle structures for local mechanical reinforcement.

Although the SLM of Invar material [9] has been well studied, we have not found any SLM Invar filters reported in the open literature, except for brief mention in marketing literature from commercial providers such as Swissto12. It is very important to note that majority of the previously demonstrated 3-D-printed filters are of relatively wide band (most larger than 2%) [10], [11], unsuitable for OMUXs. These filters are also much less sensitive to fabrication tolerance than the narrowband dual-mode filter we chose to build and demonstrate. A spherical dual-mode resonator filter with 0.47% fractional bandwidth is presented in this work. A polymer version of the spherical dual-mode resonator using stereolithography technology was first reported in [12]. Holes were added to the structure to facilitate plating. The bandwidth of the filter was over 3%. The high thermal expansion, low power handling, knotty EMC problems with the plating holes, and potential issues related to mechanical loads hinder the polymer-based filters from being used in higher-power OMUXs of real-world satellite payloads.

In this paper, the mechanical properties, as well as the RF and thermal stability performance of SLM Invar resonators and filters are demonstrated. Comparison with an aluminum-copper alloy is done. The manufacturing parameters and the coating process are discussed.

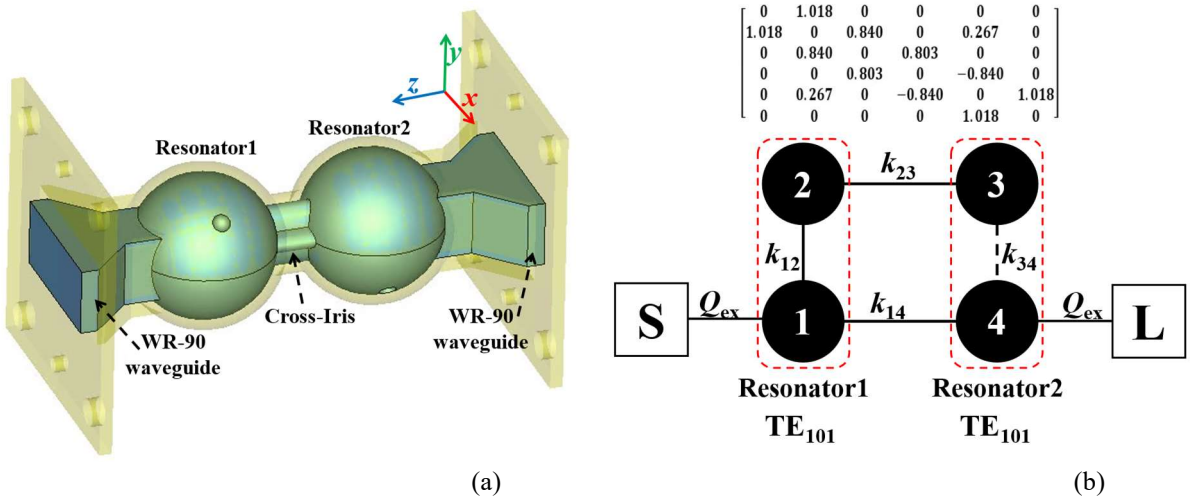

(a) (b)

Figure 3.1 (a) Configuration of the 3D printed Invar spherical dual-mode filter: (yellow: the metallic wall; blue: the internal air-model). (b) Coupling topology and normalized coupling matrix. (Solid line: Positive coupling, Dash line: Negative coupling)

3.2 Spherical Dual-mode Filter Design

A spherical dual-mode fourth-order filter with a quasi-elliptic response and two transmission zeros is adopted here. Figure. 3.1(a) shows the configuration of the proposed filter. It consists of two spherical resonators which are joined by a cross shaped iris. Two WR-90 waveguides serve as the feeding ports. Each resonator supports a pair of orthogonally polarized TM_{101} resonance modes.

Table 3.1 Comparison of Different Types of Cavity Resonators

Resonator	Mode	Q_u	Dimensions (mm)
Rectangular	TE_{101}	7936	22.86 (L) × 10.16 (W) × 15.87 (H)
	TE_{102}	9910	22.86 (L) × 10.16 (W) × 31.73 (H)
	TE_{103}	10710	22.86 (L) × 10.16 (W) × 47.60 (H)
Cylindrical	TE_{111}	11870	27.18 (D) × 15.68 (H)
	TE_{112}	17149	27.18 (D) × 31.36 (H)
	TE_{113}	19873	27.18 (D) × 47.03 (H)
Spherical	TM_{101}	14015	22.80 (D) × 22.80 (D)

L, W, H, D, denote length, width, height, and diameter of the resonators.

Table 3.1 shows a comparison between the used spherical resonator and the common dual-mode cavity resonators in terms of the simulated unloaded quality factor (Q_u) and the corresponding physical dimensions, where all resonators operate at 11.5 GHz. All EM-simulations were performed using the Computer Simulation Technology (CST) Studio Suite, and all cavity walls were assumed to be smooth silver with electrical conductivity of 6.302×10^7 S/m. From this table, it can be seen that the spherical dual-mode resonator exhibits significant advantages over the others. It has the highest Q_u among the dominant modes (TE_{101}, TE_{111}, TM_{101}) and shows considerably reduced size over other higher modes. The filter is designed to have a center

frequency of 11.483 GHz, bandwidth of 54 MHz, and passband return loss of 20 dB. The coupling topology is shown in Figure. 3.1(b), where the cross coupling between mode 1 and 4 is introduced to generate two symmetrical transmission zeros at 11.438 GHz and 11.528 GHz to improve the frequency selectivity. From [13], the external quality factor and non-zero coupling coefficients can be calculated: Q_{ex} = 205.7, k_{12} = -k_{34} = 0.840, k_{23} = 0.803, and k_{14} = 0.267.

Figure. 3.2 illustrates the YZ-plane sectional view of the filter and some critical coupling structures. The two black arrows indicate the electric field (E-field) direction of mode 1 and mode 4. The dash lines denote three *XY*-plane cross sections (XY-1, 2, 3) with key coupling structures to be detailed later in Fig. 3 and 4. The first and third one is located at the middle of the two spherical cavities whereas the second one is at the middle of the cross-iris.

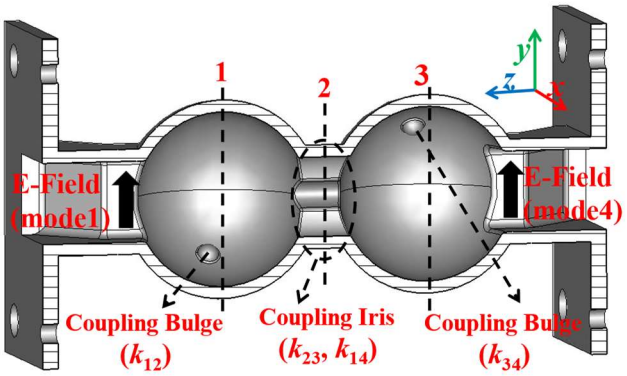

Figure 3.2 Section view showing the internal structures. (Two black solid arrows indicate E-field direction, and three black dash lines indicate the position of three XY-plane cross sections with critical coupling structures).

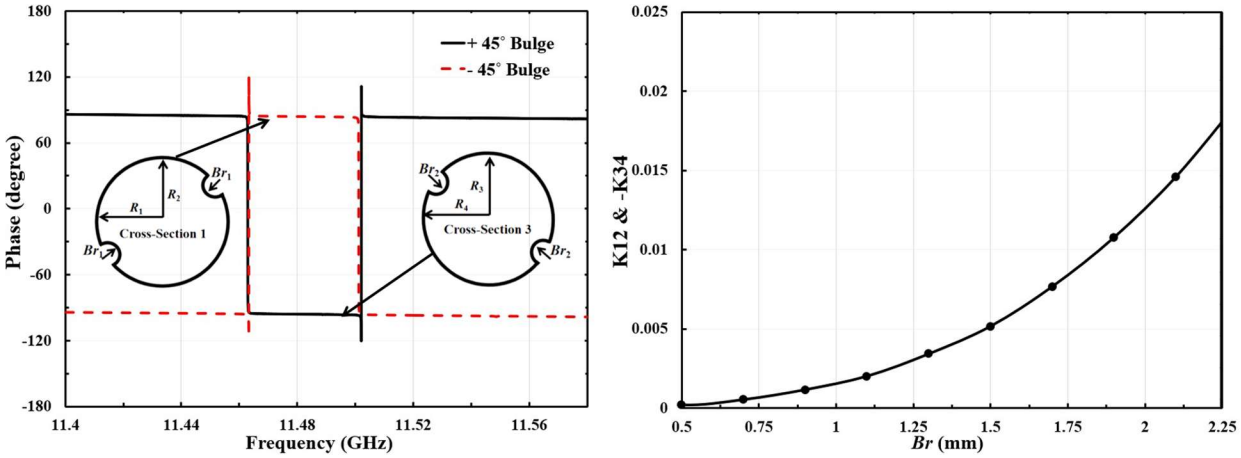

Figure 3.3 (a) Phase response of the transmission coefficient of the intra-resonator coupling with insets showing the corresponding structures and dimensions. (b) Extracted coupling coefficient versus the radius of the coupling bulges *Br*. The final dimensions in millimeter are: R_1= R_4 = 11.025, R_2 = R_3 = 10.954, R_1/R_2 = 1.0065, Br_1 = Br_2 = 1.345.

The inset in Figure. 3. 3(a) displays the cross section XY-1 and XY-3. They are not strictly circular but elliptical with a width-height ratio close to 1. The horizontal and vertical radius of each spherical cavity are labelled as R_1, R_2, R_3 and R_4. By changing them, the frequency of each mode can be tuned. The intra-resonator coupling (k_{12} and k_{34}) between the two orthogonal modes can be further controlled by a pair of round bulges

at +/− 45° directions. The purpose for adding a pair of coupling bulges rather than just one in each cavity is to reduce the impact on the polarization orthogonality between the two TM resonance modes. Compared with the commonly used coupling stubs [12], the round bulge is easier to be printed and integrated with the spherical cavity. Positioning the coupling bulges at +/- 45° enables the coupling k_{12} and k_{34} to be out of phase and hence achieves the required coupling topology. Figure. 3. 3(a) shows the phase responses of the transmission coefficient where the +/- 45° coupling bulges exhibit opposite phase. The coupling strength is determined by the radius of the coupling bulges Br_1 or Br_2, as presented in Figure. 3.3(b).

The inter-resonator and cross coupling are realized by the cross shaped iris between two cavities where the horizontal aperture is for the cross coupling k_{14} and the vertical aperture is for the main line coupling k_{23}, as indicated in Figure. 3.4(a). In this design, the thickness of the iris t is deliberately increased to allow an enlarged iris opening. This is an important feature because it not only eases the printing process but also facilitates the subsequent surface treatment (polishing and coating), when either polishing agents or an electrode needs to be inserted into the cavities. Figure. 3.4(b) shows the variation of the coupling coefficient versus the width of coupling aperture l for different thicknesses t. To achieve the same level of coupling, a thicker iris will allow an increased l. It is also shown that the curve representing the thicker iris has a gentler slope. This means the thicker iris reduces the sensitivity to the fabrication tolerance as an added benefit. The wider and longer iris would have a negative impact on the spurious performance. However, both measurement and simulation show that there is no spurious passband over the whole X band from 8.2 to 12.4 GHz.

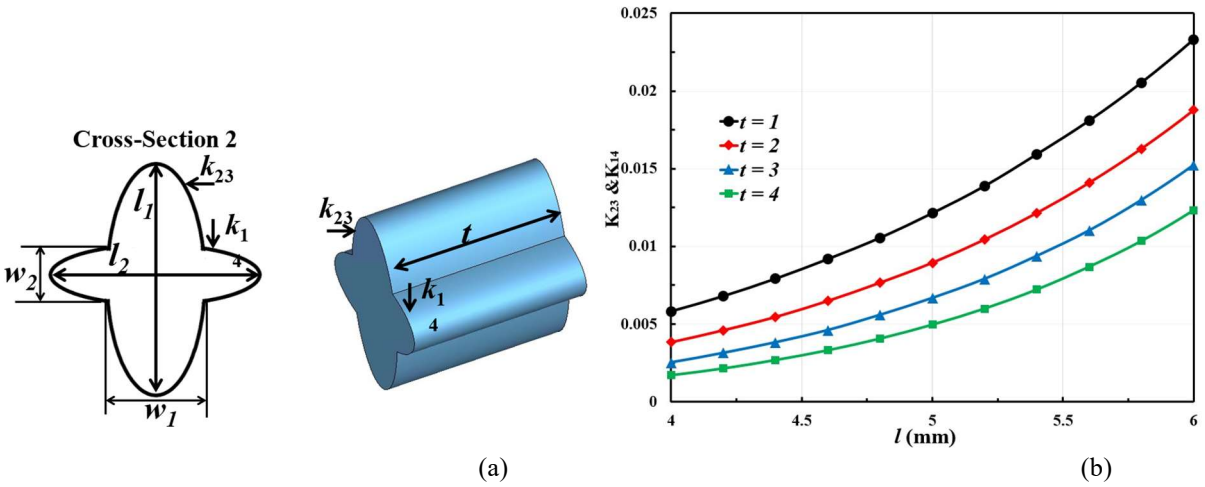

(a) (b)

Figure 3.4 (a) The inter-resonator and cross coupling structures with key dimensions. (b) Extracted coupling coefficient versus the dimension l (w = 2 mm) with varying t. The final dimensions in millimeter are t = 4.3, l_1 = 5, w_1 = 2.33, l_2 = 4.25, w_2 = 2.

3.3 Material, Manufacture and Coating

The Invar filter samples were 3D printed from a pre-alloyed spherical powder on top of a steel substrate with SLM additive manufacturing technique using a Concept Laser M2 Cusing system. In order to achieve maximum bulk microstructure density, a laser parametric study was performed first on 5 mm × 5 mm × 7 mm coupons as shown in Figure. 3.5(a), using the laser processing window parameters given in Table II and with a constant powder layer thickness of 30 µm. The heat input was represented in terms of the laser energy density (E = *Laser-Power*/*Scan-Speed*/*Scan-Spacing*) [14]. The scanning electron microscope (SEM) micrographs in Figure. 3.5(b)-(d) show the influence of E on the microstructure's density evolution. It is observed that the coupons built with $E \leq 1.0$ J/mm^2 show porous microstructure with unfused defects (un-melted particles within the pores) as seen in Fig. 5(b), leading to low density. The monotonic increase in E

decreases the lack-of-fusion defects and increases the degree of consolidation, as shown in Figure. 3.5 (c) and (d), leading to a dense material when the laser energy density is between $1.4 \leq E \leq 4.2$ J/mm^2. However, the higher E values in this range lead to evaporation that creates pores within the builds as seen in Fig. 5(d). Also, the high E parameters might cause over-melting, rough downward surface, and distortion. The consolidation behavior is also represented by the Archimedes density measurements in Fig. 5(e), where all coupons built with $1.4 \leq E \leq 4.2$ J/mm^2 show fairly constant density with an average value of 8.0 g/cm^3. In order to achieve reasonably high density as well as good surface finishing, the parameter chosen to manufacture the part is 1.4 J/mm^2, which is the minimum E required to reach the high-density regime. The estimated porosity fraction is $2.3 \pm 0.15\%$. It is worth mentioning that all builds beyond $E = 4.2$ J/mm^2 failed as the extremely high E value leads to higher thermal stresses [15].

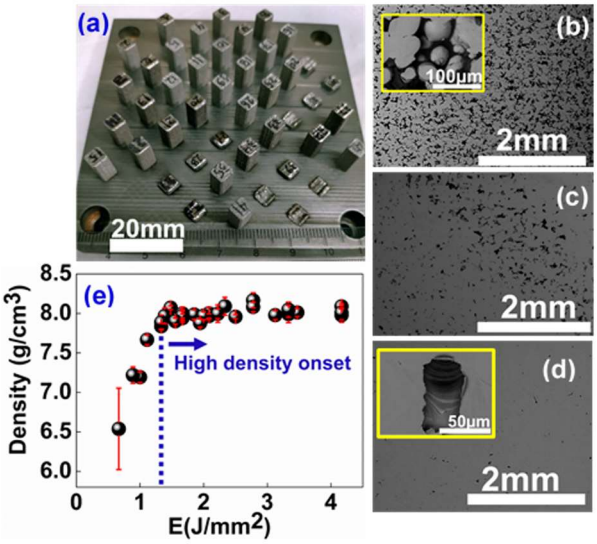

Figure 3.5 (a) The as-printed coupons with different laser energy density E on top of a steel substrate, (b) (c) (d) SEM micrographs of the coupons built with E = 0.8, 1.1 and 1.4 J/mm^2, respectively, which show the influence of laser process parameters on densification mechanism. The inset shows the respective microstructural defects, and (e) the influence of laser process parameters on the Archimedes density.

An aluminium-copper alloy (A20X) sample was also 3D printed and used as a benchmark as its CTE value is similar to the aluminium alloy used for space application. The A20X sample was fabricated using a SLM500HL printer with the processing parameter given in Table 3.2.

Table 3.2 Investigated Range of Processing Parameters

Material	Laser power/P (W)	Scan speed/V (mm/s)	Scan spacing/h (mm)	Energy density/E (J/mm^2)
Invar	150-350	800-2500	0.06-0.09	0.6-7.3
A20X	360	1500	0.15	1.6

Table 3.3 compares the SLM Invar and SLM A20X in terms of their mechanical properties. Where two values are provided, they correspond to the horizontal/vertical building directions, respectively. This measurement was carried out by Deben 500 tensile testing machine using 2 mm × 2 mm flat dogbone samples.

Table 3.3 Mechanical Properties of The SLM Invar and A20X Alloy

Material	Density (g/cm^3)	E* (GPa)	$\sigma_{0.2}$ (MPa)	σ_{UTS} (MPa)	δ (%)
A20X-AF#	2.85	72.8/75.5	303/313	398/390	9.8/9.6
Invar-AF [9]	8.1	-	398/353	510/422	15/3

*E: Elastic modulus; $\sigma_{0.2}$: Yield strength; σ_{UTS}: Ultimate tensile strength; δ: Elongation. #AF: As-fabricated.

The printing direction is parallel to the propagation direction of the microwave components, as shown in Figure. 3.6. No internal support structures are required. The design has considered several features to facilitate SLM manufacturing. The spherical cavities are self-supportive during the printing. The inter-cavity and input/output irises alleviate overhangs of greater than 45°. The feed waveguide is tapered to avoid flat ceilings. The waveguide flange is modified (see the photo in Figure. 3.6) to alleviate stress-induced bending as well as to reduce the weight. The as-printed samples were cut off the substrates via EDM and the flange surface was mechanically ground to improve its smoothness. Post polishing was done by a Sharmic vibration polishing machine with 3 mm size ceramic particle media. The polishing process takes 6 hours, and the samples are then ultrasonically cleaned with ethanol for 10 min and dried in oven at 100 °C before further testing.

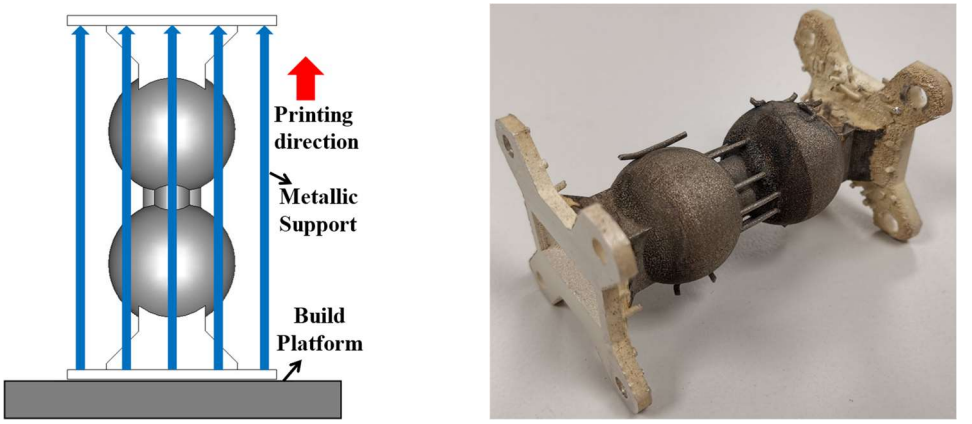

Figure 3.6 (a) Diagram showing the printing direction; (b) Photo of the Invar filter after silver plating.

The SLM Invar filter was electroplated with silver. Figure. 3.6 shows the photography of the Invar filter after surface coating. To encourage coating on the inside, part of the external surface was masked during plating. An anode was inserted through the filter. This necessitates large enough irises in the design especially for narrow band filters. The roughness of the internal surface is believed to have some adverse impact on the quality of silver plating. It is worth mentioning that silver plating on machined Invar is a well-tested and used process in general. However, what is less known is the quality of coating on the internal surface of a semi-closed, monolithic, 3D-printed part like the cavity filter. This is worth further investigation and research.

3.4 Measurement and Discussion

To evaluate the printing quality and the thermal stability of the printed Invar components, a thermal-RF measurement was performed. This test was carried out using an in-house built experimental setup where a pair of thermal isolators are used [16].

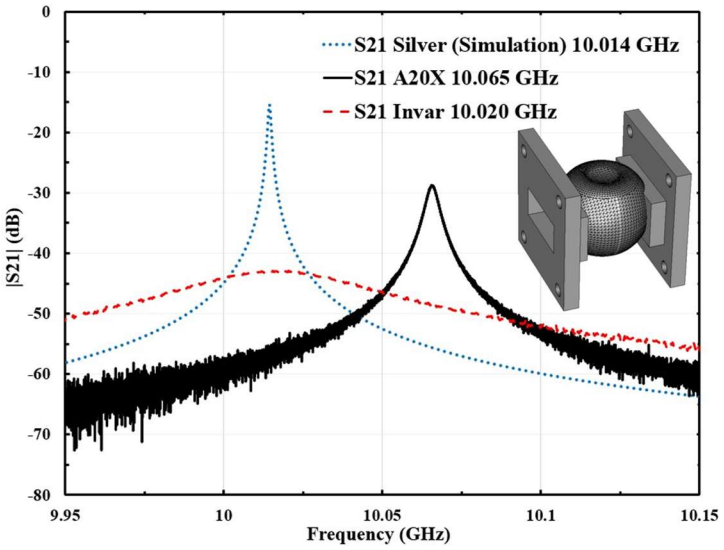

Figure 3.7 Measured resonance curves at room temperature with inset showing the dimpled spherical single-mode resonator.

A dimpled spherical single-mode resonator [17] was first measured. To provide a benchmark and the first-order indication of the dimension accuracy of the as-printed sample, an A20X and an Invar resonator were first tested at room temperature (~20 ℃). As shown in Figure. 3.7, both samples have a slightly higher resonance frequency than expected from the simulation, which is partly due to the shrinkage during the printing process. From the transmission response in Figure. 3.7, the Q_u and the corresponding effective electrical conductivity can be further extracted, as presented in Table 3.4.

Table 3.4 Measurement Result Summary of The Resonators

Material	Q_u @20 ℃	Effective conductivity ($\times 10^7$S/m)	Effect. temp. coefficient (ppm/K)
Invar	167	0.0015	1.85
A20X	4057	0.778	21.7

Next, the operating temperature was raised up to 160℃ at an interval of around 20℃. The transmission responses at each point were measured after a stabilization time of 30-40 minutes. Figure. 3.8 shows the measured resonance curves as a function of temperature for both resonators. It is apparent that the frequency variation of the Invar resonator is negligible comparing to the A20X resonator. To establish a correlation between the frequency shift and the CTE, we define the 'effective temperature coefficient' of the resonator as $\mathrm{d}(\Delta f/f)/\mathrm{d}T$. It has the same unit of ppm/K as the CTE of the materials. The start and end temperature are used to extract this coefficient. The results are summarized in Table 3.4. The Invar resonator has a very low thermal expansion of 1.85 ppm/K. Its Q_u increased slightly with temperature. As expected, the Invar resonator has extremely low Q_u. It requires surface-coating to improve its RF performance.

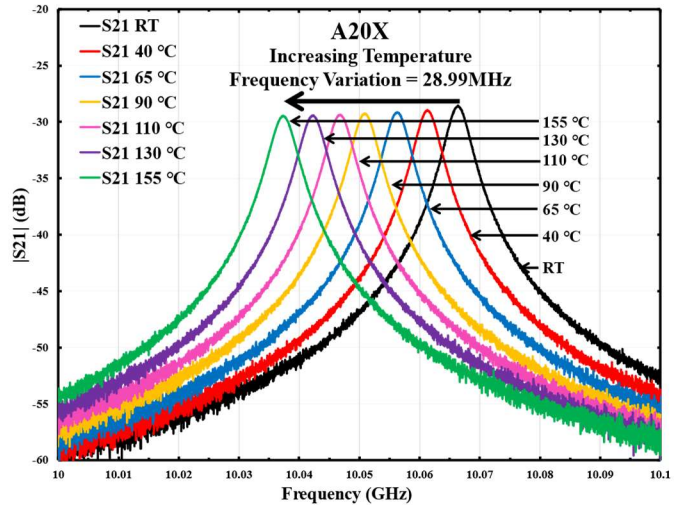

(b)

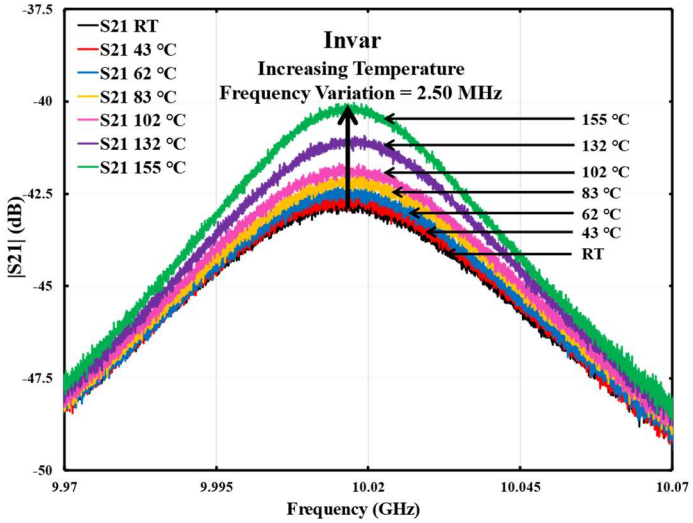

(a)

Figure 3.8 Measured resonance curves as a function of temperature. (a) A20X resonator. (b) Invar resonator.

For the RF measurement of the Invar filter, Figure. 3.9 shows the measurement results before and after silver plating without any tuning. As can be observed, both measured responses exhibit a shift of the passband against their simulated counterparts. The frequency shift before and after silver-plating is 70 MHz and 80 MHz, respectively. The small discrepancy (10 MHz) in the shifts is attributed to thickness of the plated silver layer which is estimated to be 11 μm. The conductivity of the Invar used in the simulation is extracted from the resonator measurement as given in Table 3.4.

For the silver-coated filter, the measured center frequency is 11.565 GHz, and the average insertion loss is around 1 dB, which is higher than the simulated one of 0.4 dB, as shown in Figure. 3.9(b). This extra loss is partly due to the lower-than-expected return loss (~10 dB) and partly due to the surface roughness [18], which degrades the effective conductivity of silver.

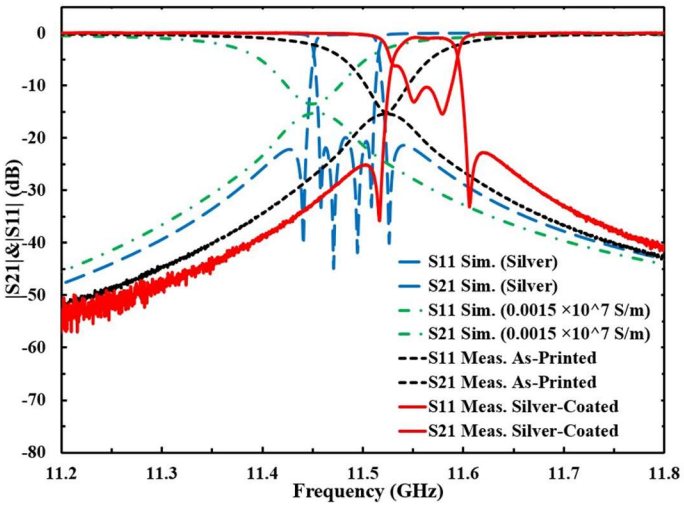

(a)

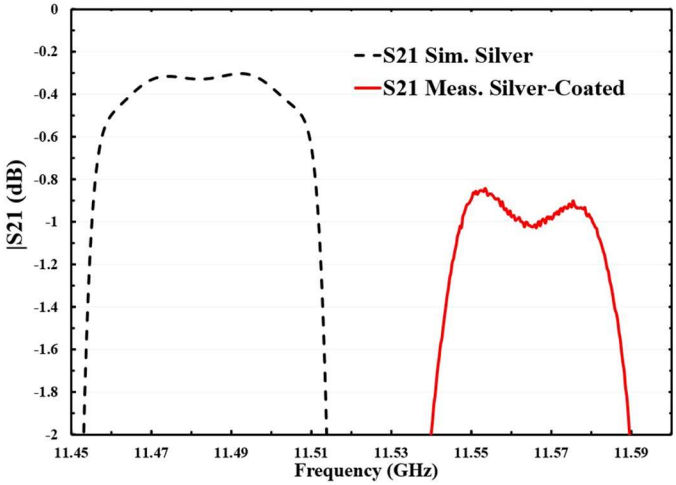

(b)

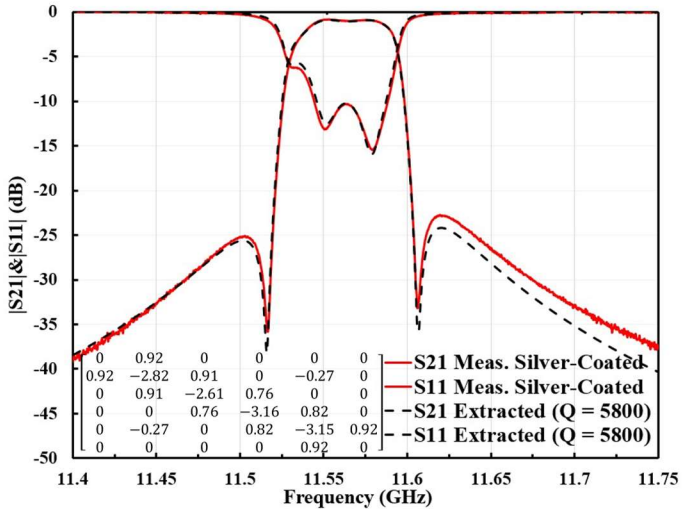

(c)

Figure 3.9 (a) Measurement (solid lines) and simulation (dashed lines) results of the 3D printed Invar filter. (b) The enlarged view of S_{21} responses over the passband. (c) comparison between the measured results and the filter response from the extracted coupling matrix (see the inset).

In the ideal situation of the resonator with infinite Q_u, the return loss of 10 dB alone would have contributed 0.45 dB mismatch loss. If perfectly smooth silver is assumed for the conductivity of the filter (6.302×10^7 S/m), the total insertion loss would be 0.8 dB. The Q_u can be calculated to be about 12500. For the measured insertion loss of 1 dB, the coupling matrix method is used to reproduce the measured response and to extract the corresponding Q_u. Figure. 3.9(c) shows a comparison between the measured result and the extracted filter response. They agree very well. From this figure, the Q_u can be extracted to be 5800, which is about 46% of the ideal silver-plated filter. Simulation shows this corresponds to an effective conductivity of 1.26×10^7 S/m. If the return loss can be improved to 15 – 20 dB, the insertion loss should be reduced to well under 1 dB. The higher-than-simulated S_{11} is probably due to the small dimension inaccuracies in critical coupling structures. Considering the narrow bandwidth and tuning-free measurement condition, we think the performance of the 3-D printed Invar filter is very encouraging.

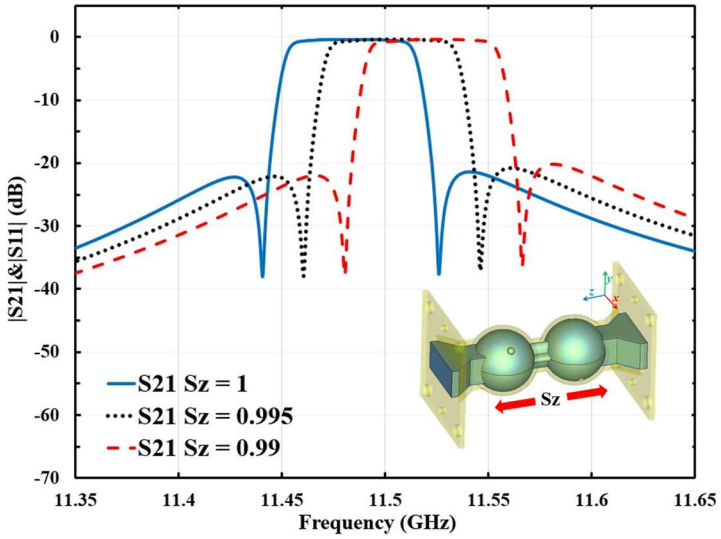

(a)

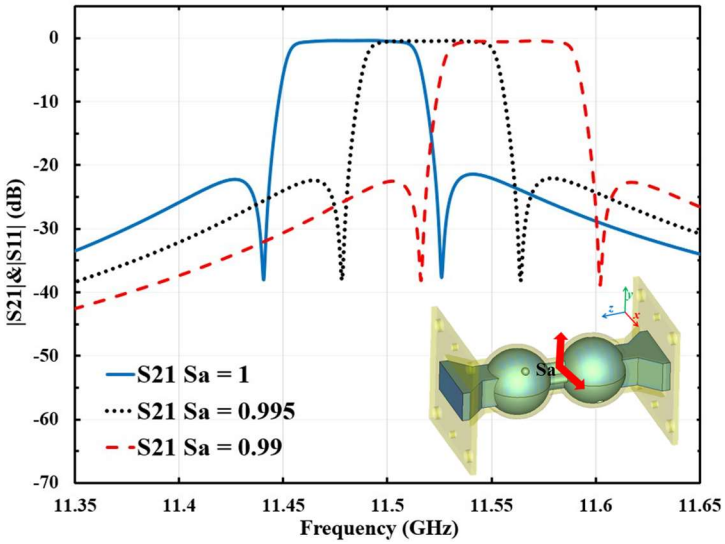

(b)

Figure 3.10 The simulated transmission response as a function of the shrinkage ratio. (a) shrinkage along the *Z*-axis. (b) Shrinkage along the *XY*-plane.

To investigate the frequency shift of the passband which is believed to be mainly due to the material shrinkage during the printing process, a parameter study involving dimension scaling was carried out. The shrinkage ratio along *Z*-axis is set as *Sz* and that along the *XY*-plane is *Sa* (the shrinkage assumed to be isotropic along *X*/*Y* direction). As can be observed from Figure. 3.10, the shrinkage on *XY*-plane has a more pronounced effect on the frequency, while the *Z*-axis shrinkage incurs a small asymmetry to the transmission response, which also exists in the measurement result. Figure. 3.11 shows a comparison between the measured and simulated filter performance where *Sz* = 0.99 and *Sa* = 0.995. A reasonably good agreement can be observed.

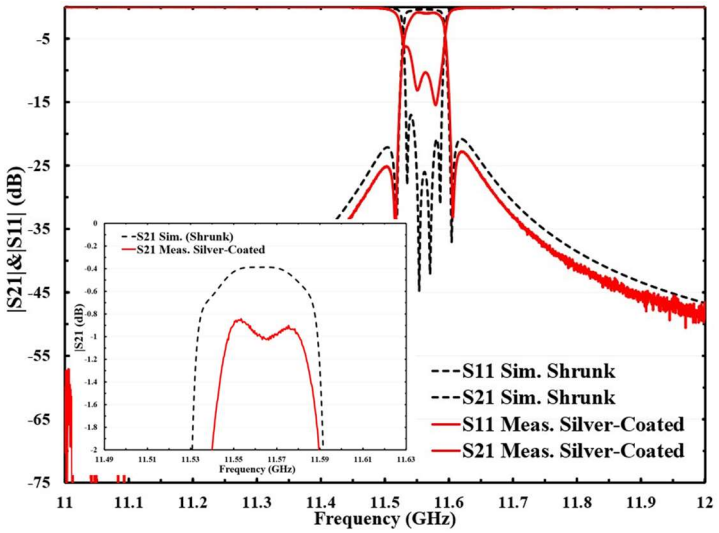

Figure 3.11 Comparison of the filter performance. (Solid line: measurement result. Dot line: Simulation result considering the impact of shrinkage).

Based on the above discussion, it is expected that the final filter performance can be improved by pre-design compensation for the dimension and by adding tuning screws. To demonstrate this, holes were drilled on the 3D printed filter and six M2 stainless steel tuning screws were added for fine tuning the resonant frequencies and inter-resonator couplings. An improvement has been evidenced as shown in Figure. 3.12(a). However, the insertion loss with tuning screws is increased by almost 0.5 dB, as a result of loose installation of the screws as well as the loss from the un-plated steel materials. The corresponding Q_u can be extracted to be 2900 using the coupling matrix method, as shown in Figure. 3.12(b). It is expected that the insertion loss can be improved using silver-coated brass or Invar screws. It is also worth pointing out that a more optimal process is to drill the tuning holes before silver plating to avoid potential damage to the coating.

Next, the temperature-dependent RF measurement was performed on the Invar filter. The experiment process is similar to the resonator-based test. Figure. 3.13 shows the measured performances of the Invar filter. The temperature stable performance is clearly demonstrated. There is no visible frequency shift. The loss degradation at raised temperatures is 0.3 dB. It is worth noting that the thermal isolator pair, used in the thermal-RF measurement, contributes an extra insertion loss of 0.25 dB.

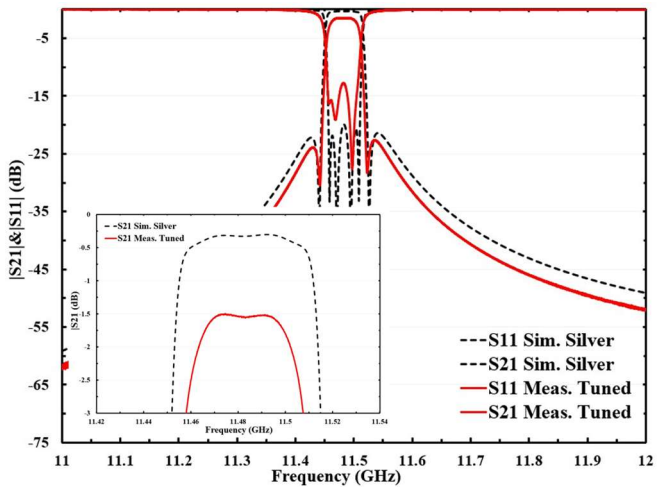

(a)

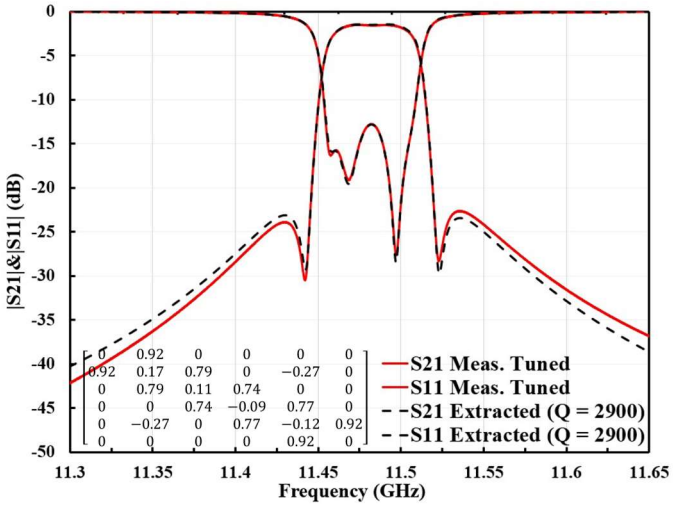

(b)

Figure 3.12 (a) Measured and simulated results of the Invar filter after tuning with inset showing the enlarged view of the S_{21} over the passband. (b) Comparison between the measured results and the filter response from the extracted coupling matrix.

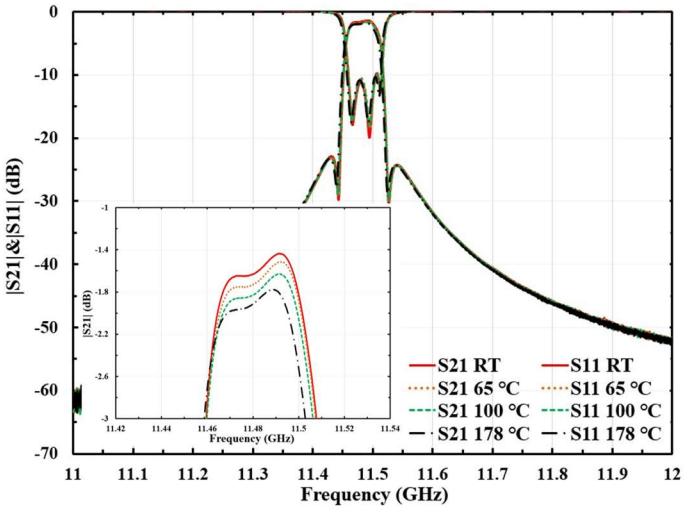

Figure 3.13 Measured filter performances of the Invar filter after-tuning as a function of the temperature with inset showing the enlarged view of S21 over the passband.

Table 3.5 provides a comparison with the 3-D printed A20X filter and an Invar filter fabricated by conventional CNC milling. There are two values given for the 3-D printed Invar filter, which correspond to the before/after-tuning results. The comparison shows that the added steel tuning screws not only increase the insertion loss but also degrade the thermal stability slightly. This could be alleviated by using silver-plated Invar screws. What is encouraging about the data is that the 3-D printed Invar filter (after tuning) exhibits comparable stability with the CNC Invar filter. The higher insertion loss can be accounted for by the low return loss as well as losses associated with the surface roughness and tuning screws.

Table 3.5 Summary and Comparison of Thermal-RF Measurement Result

	Insertion loss at ambient (dB)	Loss Degradation (dB)	Freq. temp. coefficient (ppm/K)
3-D Invar	1/1.5	0.2/0.3	0.5/1.1
3-D A20X	1.5	0.1	20
CNC Invar [1]	0.5	0.1	< 2

3.5 Conclusion

A fourth-order 0.47% bandwidth spherical dual-mode filter designed for OMUX has been reported. To the best of our knowledge, this is the first demonstrated narrowband filter additively manufactured from Invar alloy in the open literature. Table 3.6 provides a comparison with published 3-D printed filters and CNC Invar filters. This work demonstrates the possibility of using complex resonator structures in Invar filter design (without being limited to the rectangular and cylindrical cavities), and opens more design opportunities for optimal RF, mechanical and thermal properties for narrowband filters. The improvement in the thermal stability demonstrates the feasibility and superiority of the 3-D printed Invar filter. The end-to-end manufacturing methods and the detailed experimental investigation have been discussed. The presented design concept, manufacturing parameters, and material characterization may find useful applications in the design of future high-power filters.

Table 3.6 A Comparison With Some 3-D Printed Filters and CNC Machined Invar Filters

Ref.	Filter Order and Resonator Type	f_c (GHz)	FBW (%)	Printing Technology	Material
[19]	4th-order, with mushroom-shaped coaxial resonators	7.924	3.9	SLM	Stainless steel
[20]	9th-order, with depressed super ellipsoid resonator	12.875	1.9	SLM	Scalmalloy aluminum alloy
[21]	3rd-order, with spherical resonator	10	1	SLM/SLA	Al-Cu alloy/Accura Xtreme resin
[12]	4th-order, with spherical dual-mode resonator	10	3	SLA	Accura Xtreme resin
[22]	4th-order, with dual-mode super Q resonator	19.9	0.22	CNC	Invar
T.W.	4th-order, with spherical dual-mode filter	11.483	0.47	SLM	Invar

Ref: reference, f_c: central frequency, FBW: fractional bandwidth; SLM: selective laser melting; SLA: stereolithography apparatus; CNC: computer numerical control; T. W.: this work.

The 3D-printed Invar filter technology is not without challenges. Conventional machined Invar filters of the similar fractional bandwidth can have an insertion loss as low as 0.5 dB. To match this performance, more work needs to be done about the surface treatment (polishing and coating). Polishing the internal surface of monolithically-built closed cavity is especially challenging. Currently we are restricted to vibratory grinding technique, which is less intrusive to the internal critical structures compared with some other more aggressive polishing methods but also has limited capability. Electrochemical polishing may be a promising alternative.

The quality of silver plating on the SLM Invar filter can be improved. Reducing the surface roughness will help. It is worth mentioning that to understand the 3D printed internal surfaces is an ongoing research area. The influence of multiple factors such as the laser process parameters, the printing direction and the thermal treatment complicates this matter significantly. Finally, it is also expected to have more weight reduction features, and further optimized resonator geometry are expected to enhance the competitiveness of the SLM Invar technology in high-power filter applications.

Reference

[1] B. Yassini and M. Yu, "Ka-Band Dual-Mode Super Q Filters and Multiplexers," *IEEE Trans. Microw. Theory Tech.*, vol. 63, no. 10, pp. 3391–3397, Oct. 2015.

[2] Ming Yu, D. J. Smith, A. Sivadas, and W. Fitzpatrick, "A dual mode filter with trifurcated iris and reduced footprint," in *2002 IEEE MTT-S International Microwave Symposium Digest (Cat. No.02CH37278)*, 2002, vol. 3, pp. 1457–1460.

[3] M. D'Auria *et al.*, "3-D Printed Metal-Pipe Rectangular Waveguides," *IEEE Trans. Components, Packag. Manuf. Technol.*, vol. 5, no. 9, pp. 1339–1349, 2015.

[4] X. Shang, J. Li, C. Guo, M. J. Lancaster, and J. Xu, "3-D printed filter based on helical resonators with variable width," *IEEE MTT-S Int. Microw. Symp. Dig.*, pp. 1587–1590, 2017.

[5] M. Salek, X. Shang, and M. J. Lancaster, "Compact S-Band Coaxial Cavity Resonator Filter Fabricated by 3-D Printing," *IEEE Microw. Wirel. Components Lett.*, vol. 29, no. 6, pp. 382–384, 2019.

[6] V. E. Boria and B. Gimeno, "Waveguide filters for satellites," *IEEE Microw. Mag.*, vol. 8, no. 5, pp. 60–70, 2007.

[7] A. E. Williams, "A Four-Cavity Elliptic Waveguide Filter," *IEEE Trans. Microw. Theory Tech.*, vol. 18, no. 12, pp. 1109–1114, Dec. 1970.

[8] S. Cogollos *et al.*, "A systematic design procedure of classical dual-mode circular waveguide filters using an equivalent distributed model," *IEEE Trans. Microw. Theory Tech.*, vol. 60, no. 4, pp. 1006–1017, 2012.

[9] C. Qiu, N. J. E. Adkins, and M. M. Attallah, "Selective laser melting of Invar 36: Microstructure and properties," *Acta Mater.*, vol. 103, pp. 382–395, 2016.

[10] C. Guo, J. Li, X. Shang, M. J. Lancaster, and J. Xu, "Progress on microwave devices fabricated using stereolithography 3-D printing technique," *2017 Int. Appl. Comput. Electromagn. Soc. Symp. China, ACES-China 2017*, no. 2, pp. 2–3, 2017.

[11] C. Tomassoni, O. A. Peverini, G. Venanzoni, G. Addamo, F. Paonessa, and G. Virone, "3D Printing of Microwave and Millimeter-Wave Filters: Additive Manufacturing Technologies Applied in the Development of High-Performance Filters with Novel Topologies," *IEEE Microw. Mag.*, vol. 21, no. 6, pp. 24–45, Jun. 2020.

[12] C. Guo, X. Shang, J. Li, F. Zhang, M. J. Lancaster, and J. Xu, "A Lightweight 3-D Printed X-Band Bandpass Filter Based on Spherical Dual-Mode Resonators," *IEEE Microw. Wirel. Components Lett.*, vol. 26, no. 8, pp. 568–570, 2016.

[13] J.-S. Hong and M. J. Lancaster, *Microstrip Filters for RF/Microwave Applications*. New York, USA: John Wiley & Sons, Inc., 2001.

[14] L. N. Carter *et al.*, "Process optimisation of selective laser melting using energy density model for nickel based superalloys," *Mater. Sci. Technol. (United Kingdom)*, vol. 32, no. 7, pp. 657–661, 2016.

[15] X. Li *et al.*, "Improved plasticity of Inconel 718 superalloy fabricated by selective laser melting through a novel heat treatment process," *Mater. Des.*, vol. 180, 2019.

[16] J. Hesler, A. R. Kerr, and N. Horner, "A broadband waveguide thermal isolator," *14th Int. Symp. Sp.*

Terahertz Technol., pp. 148–154, 2003.
[17] C. Guo *et al.*, “Shaping and Slotting High-Q Spherical Resonators for Suppression of Higher Order Modes,” *IEEE MTT-S Int. Microw. Symp. Dig.*, vol. 2019-June, pp. 1205–1208, 2019.
[18] G. Gold and K. Helmreich, “A physical surface roughness model and its applications,” *IEEE Trans. Microw. Theory Tech.*, vol. 65, no. 10, pp. 3720–3732, 2017.
[19] S. W. Sattler, F. Gentili, R. Teschl, and W. Bosch, “Direct Metal Printed 4th order Stepped Impedance Filter in the C/X Band,” in *2018 IEEE/MTT-S International Microwave Symposium - IMS*, 2018, vol. 2018-June, pp. 145–148.
[20] P. A. Booth and E. Valles Lluch, “Realising advanced waveguide bandpass filters using additive manufacturing,” *IET Microwaves, Antennas Propag.*, vol. 11, no. 14, pp. 1943–1948, 2017.
[21] F. Zhang *et al.*, “3-D Printed Slotted Spherical Resonator Bandpass Filters with Spurious Suppression,” *IEEE Access*, vol. 7, pp. 128026–128034, 2019.
[22] B. Yassini and M. Yu, “A novel ka band dual mode super Q Cavity Filter,” *IEEE MTT-S Int. Microw. Symp. Dig.*, pp. 220–222, 2014.

CHAPTER 4: MULTIPHYSICS ANALYSIS OF HIGH POWER 3-D PRINTED INVAR SPHERICAL DUAL-MODE FILTERS

Lu Qian, Abd El-Moez A. Mohamed, Moataz M. Attallah, Talal Skaik, Paul Booth, César Miquel España, Yi Wang

Yi Wang suggested this work, planned, and supervised the entire study, and led the project. Lu Qian conceived the idea of this design and carried out the theoretical modelling, analysis and simulations, and performed the experiment, interpreted the data, and wrote the manuscript. Paul Booth, and César Miquel España provided guidance on the simulation and data interpretation. Abd El-Moez A. Mohamed, Moataz M. Attallah assisted in the fabrication of this filter. All authors contributed to the writing of the paper and reviewed the manuscript.

This chapter is based on the following publication: Multiphysics Analysis of High Power 3-D Printed Invar Spherical Dual-mode Filters, which has been presented in 2023 1st Space Microwave Week, May 2023, ESA/ESTEC, Noordwijk, The Netherlands.

4.1 Introduction

Satellite output filters and multiplexers are one of the most complex and specialized microwave passive components for the on-board communication payloads. Compared to the filter networks in other communication applications, the wider operating temperature range (typically −10 to +85 °C), and the higher channel power level (typically in the range of several hundreds of watts) are usually required [1]–[3]. Therefore, the temperature stability and the power handling capability are key design challenges. For a high-power filter for space application, the following factors may be considered [4]: 1) thermally induced frequency detuning, 2) high-power breakdown, 3) passive intermodulation (PIM) interferences. To reduce the power loss and minimize the self-heating effect due to thermal dissipation, high quality-factor(Q) cavity resonators are usually required for such equipment [5]. Common high-Q resonators include the TE_{011} single mode cylinder resonator, TE_{11N} (N = 1 - 5) and TE_{221} dual mode cylinder resonators. To achieve stable RF performance over a wide operating temperature range, a typical approach is to use a material with low coefficient of thermal expansion (CTE), such as Invar, or to use an external temperature compensation mechanism [6]. The relatively narrow channel bandwidth and the high electric fields inside the high-Q resonators also increase the risk the high-power breakdown. For the satellite OMUXs, multipaction is a main source of the high-power breakdown. It is an RF breakdown in the vacuum or low-pressure environments. Extensive theoretical investigation and verification procedure can be found in [7], [8]. To prevent the occurrence of this breakdown phenomenon, many methods have been invented such as increasing the gap size, adding dielectric filling, and reducing surface potential through surface treatment. In addition, the power handling capability is susceptible to PIM, which is mainly caused by the material imperfection and contact nonlinearity [9]. In principle, PIM can be mitigated by reducing the mechanical interfaces and joints. Recently, we demonstrated the RF design and additive manufacturing of a narrowband (~0.47% fractional bandwidth) channel filter for high-power OMUX applications, using laser powder bed fusion technology of Invar alloy [10]. Spherical dual-mode resonators were used in the design. Due to the low coefficient of thermal expansion of Invar, high thermal stability of the filter has been achieved. It was monolithically 3D-printed in a single piece, significantly reducing the need for assembly and hence reducing the possibility of PIM. An end-to-end process has been developed and implemented, together with a design-for-additive-manufacturing approach. However, the closed structure, as a result, presents the challenge for internal surface treatment (e.g. polishing and coating).

In this paper, the latest measurement results based on the re-coated Invar filter will be presented. To address the internal surface treatment, an electrochemical polishing technique was investigated. A 3D printed monolithic spherical resonator was processed using this novel surface treatment method. Compared to the mechanical polishing method we used before, a significant improvement on the resonator's unloaded quality-factor (Q_u) has been achieved. In addition, multiphysics co-simulation and multipaction analysis on the spherical filter will be presented. The multiphysics simulation was performed to investigate the filter's thermal stability under the practical high-power operation. The result demonstrates that the effective temperature coefficient of less than 1 ppm/K can be achieved. This is in good agreement with the previous thermal-RF measurement. For the multipaction analysis, the numerical simulation tool SPARK3D was used to estimate the breakdown threshold. To ensure the convergency of the simulation, finer local mesh density, and different initial power as well as initial electron number were applied to the base-line case. In order to considering the possible parameter deviation due to the material condition and surface treatment [11], analysis under different secondary emission yield (SEY) parameters was carried out, such as the maximum SEY coefficient and different low crossover electron energy. According to these simulation results, the Invar filter can provide a design margin of greater than 10 dB for the specified channel power of 150 W.

4.2 Spherical Dual-mode Filter

The spherical dual-mode filter is specified with a center frequency of 11.483 GHz, a bandwidth of 54 MHz, and in-band return loss of 20 dB. The detailed discussion about this filter has been reported in [10]. In the previous measurement, the Q_u value extracted from the tunned Invar filter is only 2900 because of the improper processing arrangement and the used un-plated tuning screws. To improve the performance, the tuned invar filter was electroplated again and tunned using the silver-coated brass screws. Figure. 4.1(a) compares all measured results of this Invar spherical filter, where the inset is the enlarged view of S_{21} responses over the passband. As can be observed, the measured insertion loss is improved from 1.5 dB to near 1 dB after the second silver plating. The coupling matrix method is used to reproduce the measured response and to extract the corresponding Q_u. Figure. 4.1(b) shows a comparison between the measured result and the extracted filter response. The two filter responses show a good correlation, and the extracted Q_u is 4900. There is an improvement of near 70% over the first plating. However, it is still much lower than the ideal silver-plated filter with the Q_u of 12500. This discrepancy in insertion loss is mainly due to the higher surface roughness of the 3D printed invar filter.

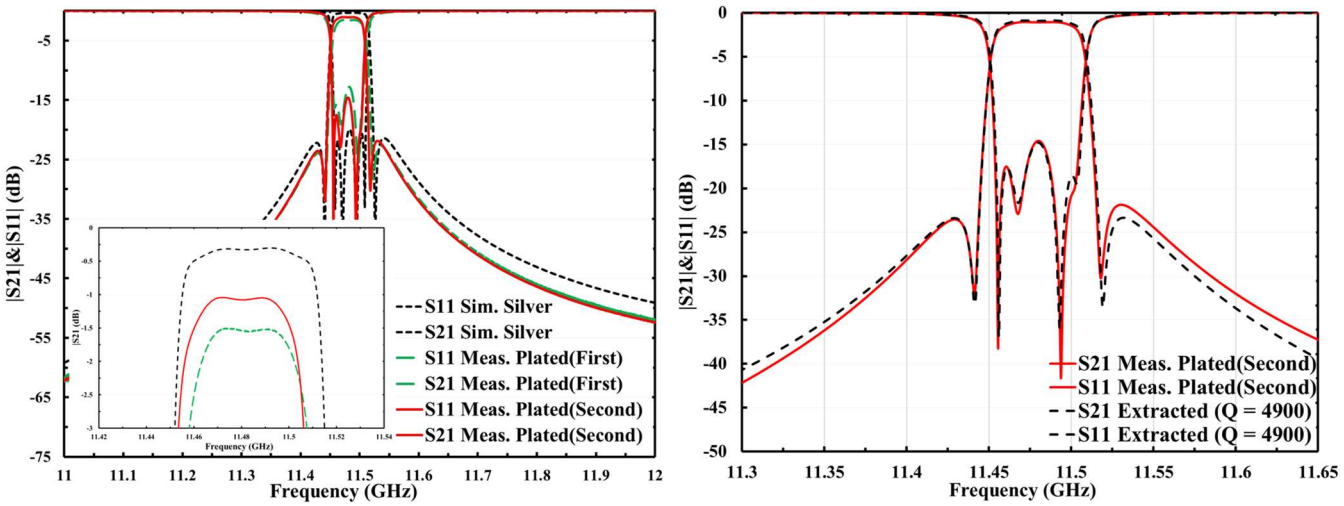

(a) (b)

Figure 4.1 (a) Measured and simulated results of the Invar filter with inset showing the enlarged view of the S21 over the passband. (b) Comparison between the measured results and the filter response from the extracted coupling matrix.

Polishing the Invar surface is nontrivial, especially for the inner surface of monolithically-built closed cavity. We have investigated the effect of different polishing parameters and different methods such as the vibratory grinding technique and the more aggressive but controlled electrochemical technique – Hirtisation®. Figure. 4.2(a) shows the photograph of a 3D printed Invar spherical resonator, used as the experimental prototype. Figure. 4.2(b) shows the measured surface roughness *S*a after different surface treatments. These *S*a values are obtained by averaging several surface roughness measurements taken at different points of Invar resonator using Alicona InfiniteFocusSL microscope. As can be observed, the mechanical polishing technique only has very limited effect on the surface roughness even with long polishing time. The achieved minimum *S*a is 5.3 μm after 12 hrs. In contrast, the electrochemical polishing method has delivered more significant improvement. The surface roughness has been reduced to 2.9 μm. The improvement is also reflected in the Q_u. After silver plating, the electrochemically polished resonator achieves a Q_u of 7995, which is 64% of the ideal silver-plated Invar resonator.

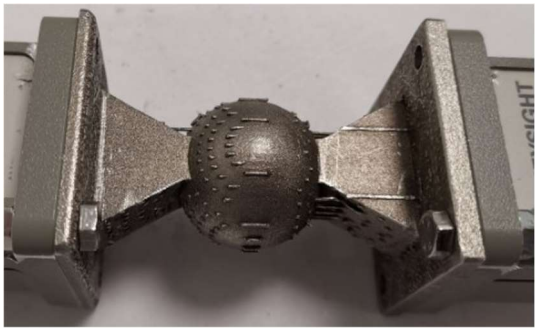

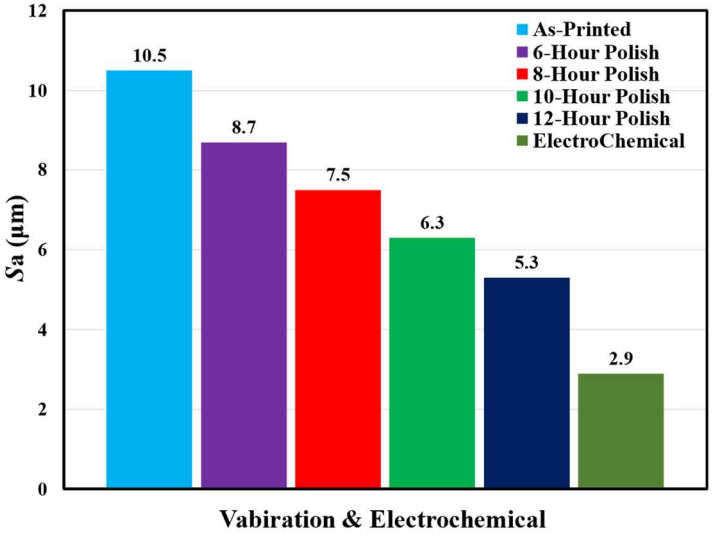

(a) (b)

Figure 4.2 (a) Photo of the 3D printed Invar spherical resonator. (b) Change of surface roughness Sa values with different polishing time and polishing technique.

4.3 Multiphysics Co-Simulation

Table 4.1 Summary of Multiphysics Simulation Results

Filter wall thickness (mm)	Highest Temperature (℃)	Maximum Heat Flux Density (W/cm^2)	Frequency Shift (MHz)	Worst Return Loss (dB)
1.5 (Low Power)				21
1.5 (High Power)	158	1.7	-1	19.6
1 (High Power)	177	1.8	-1	19.5
0.5 (High Power)	221	2.1	-1	18.5

In addition to the variation of the environmental temperature, the heating effect caused by the thermal dissipation also has a significant effect on the power handling capability of the spherical resonator/filter. This problem is further exacerbated in the case of the narrow band filter. To evaluate the stability of the 3D printed Invar filter under high-power operation, multiphysics simulation was performed using the co-simulation capability from CST. Figure. 4.3(a) shows the filter model, where the spherical filter is made up of silver-plated Invar while all external brackets and the baseplate are made of aluminium. An average input power of 150 W is considered in RF simulation. For the thermal analysis, the background related to space environment is defined, and a temperature of 85 ℃ is defined for the baseplate under which the on-board cooling system is mounted. Figure. 4.3(b) shows the temperature distribution of the filter structure where the filter wall thickness is assumed to be1.5 mm. The main hot spot is on the resonators and the coupling irises. The highest temperature on the filter and maximum heat flux density in the contact surface are 158 ℃ and 1.7 W/cm^2, respectively. By feeding the temperature distribution into the mechanical solver we can derive the dimensional deformation and finally obtain the corresponding filter responses through sensitivity analysis, as shown in Figure. 4.3(c). Herein, three different filter wall thicknesses were considered to investigate the trade-off between weight reduction (thinner wall) and the temperature stability. The filter response at low-power operation is used as a reference. A summary of these simulation is given in Table 4.1. As can be seen, both the highest temperature and heat flux density increase as the wall thickness decreases. However, even for the thinnest wall of 0.5 mm, there is no obvious degradation in filter performance. The maximum frequency shift

is only 1 MHz. This indicates the effective temperature coefficient is around 0.5 ppm/K, which is in good agreement with the previous thermal-RF measurement.

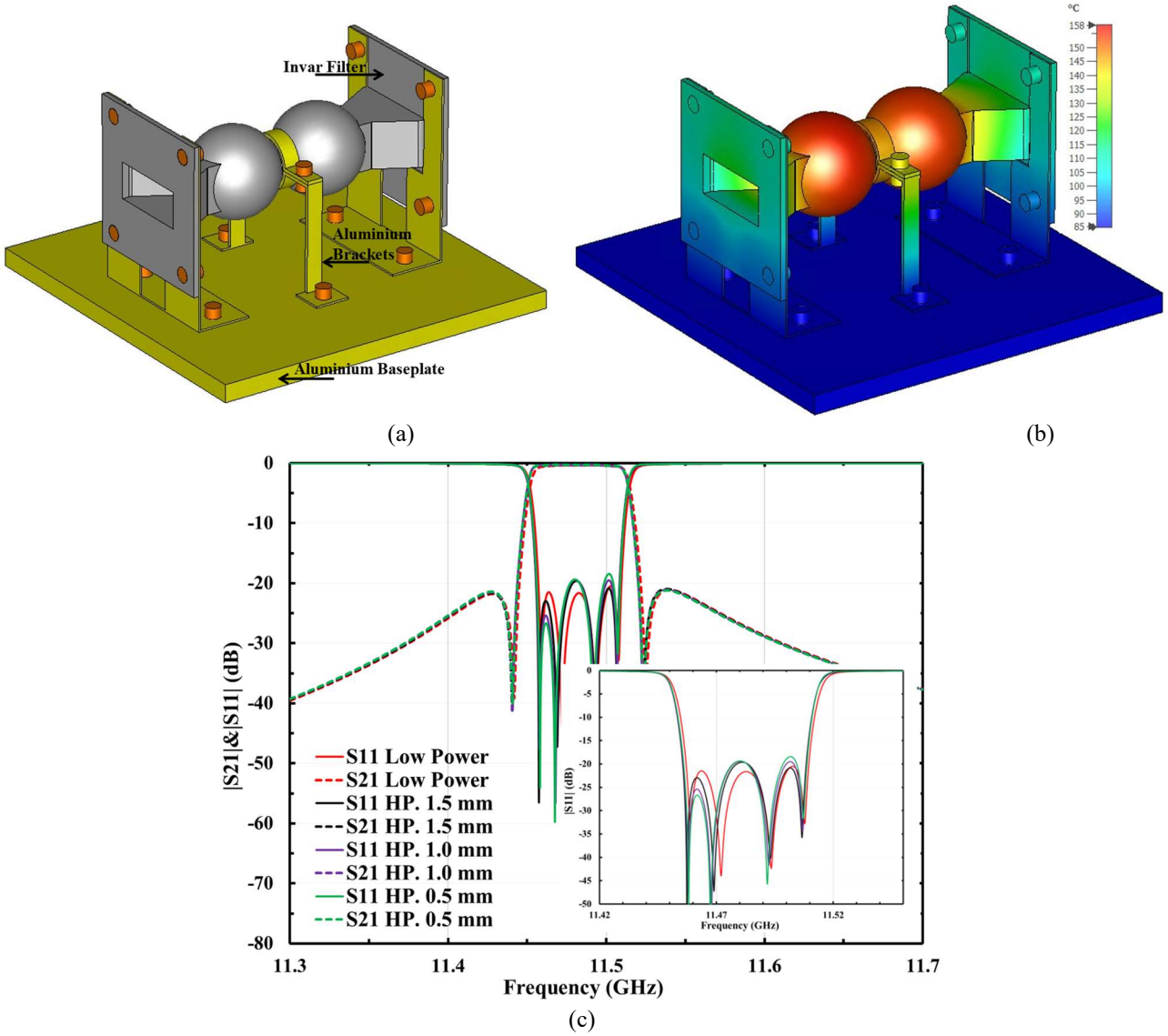

Figure 4.3 Model and simulated results of Multiphysics co-simulation. (a) Simulation model. (b) Temperature distribution. (c) Simulated filter responses under different wall thicknesses.

4.4 Multipaction Analysis

To evaluate the power breakdown threshold, the numerical software tool SPARK3D® was used to perform the multipaction analysis. First, the electrical field distribution in the spherical filter at some salient frequency points was derived using a full-wave electromagnetic (EM) solver. For better accuracy of the electric-field distribution, the maximum mesh step width for the EM solver was set to be 0.5. The selected frequency points include the passband center (11.483GHz), and two passband edges (11.456 GHz and 11.51 GHz). The single-carrier signal without modulation at the above frequency points was used. The secondary emission yield (SEY) parameter was set to the standard ECSS silver. In order to test the convergence, a number of simulation cases

were performed considering different initial power and electron number. Table 4.2 summarises these simulation settings. It has been found that all the simulations have converged to almost the same breakdown threshold around 11900 W. This is a margin of 19 dB compared to the specified 150 W input power. For the following multipaction analysis, the initial power of 50 W and initial electrons number of 1000 are used.

Table 4.2 Summary of Multipaction Analysis Setting

Initial Power (W)	Initial Number of Electrons	Signal	Material
50, 80, 120	500, 1000,4000, 7000, 10000	Single Carrier	ECSS Silver

Although nominal values for the SEY parameters are given in the ECSS standard, in practice the exact value of SEY is hard to obtain. Both surface composition and roughness can affect the practical SEY parameters. For the 3D printed Invar devices with silver plating, the surface condition is significantly different from the conventional silver-plated CNC machined parts. To account for the uncertainty in SEY, different maximum secondary emission coefficient and different low crossover electron energy were considered. The simulated breakdown power thresholds are summarized in Table 4.3. It can be observed that the variation of both parameters reduces the breakdown power. The maximum secondary emission coefficient has a greater effect on the breakdown power than the low crossover electron energy. However, even in the worst-case scenario, the spherical filter can still achieve the breakdown power of 1988 W. The margin is over 11 dB.

Table 4.3 Summary of Multipaction Analysis Results

Maximum secondary emission coefficient	2.2 (ECSS Silver)	3.3	4.4	5.5	6.6
Breakdown power (W)	11900	5150	3375	2475	1988
Low crossover electron energy (ev)	30 (ECSS Silver)	29	28	27	26
Breakdown power (W)	11900	11700	11500	11100	10700

4.5 Conclusion

This paper presents the measurement results of the Invar spherical dual-mode filter after the second plating. A spherical Invar resonator was used to investigate the effect of different surface treatment techniques. Compared to the mechanical polishing method (e.g. vibratory grinding), the electrochemical Hirtisation® process has achieved a significant improvement in the reduction of surface roughness. The thermal stability at high-power operation was shown through the multiphysics simulation. The power breakdown threshold was analyzed using SPARK3D. The results indicate this filter can provide a good design margin against the specified power. The presented 3D printed Invar components can be an attractive alternative solution to some high-power microwave applications in space.

Reference

[1] M. Yu, B. Yassini, A. Panariello, and G. Healy, "Passive components for advanced satellite systems," *IEEE MTT-S Int. Microw. Symp. Dig.*, pp. 1–3, 2012.

[2] F. De Paolis and C. Ernst, "Challenges in the design of next generation ka-band OMUX for space applications," *31st AIAA Int. Commun. Satell. Syst. Conf. ICSSC 2013*, no. October 2013, pp. 1–7, 2013.

[3] V. Singh, P. K. Ambati, S. Soni, and K. Karthik, "Enhancing Satellite Communications: Temperature-Compensated Filters and Their Application in Satellite Technology," *IEEE Microw. Mag.*, vol. 20, no. 3, pp. 46–63, 2019.

[4] M. Yu, “Power-handling capability for RF filters,” *IEEE Microw. Mag.*, vol. 8, no. 5, pp. 88–97, 2007.
[5] B. Yassini and M. Yu, “Ka-Band Dual-Mode Super Q Filters and Multiplexers,” *IEEE Trans. Microw. Theory Tech.*, vol. 63, no. 10, pp. 3391–3397, Oct. 2015.
[6] M. Lisi and E. S. Agency, “A Review of Temperature Compensation Techniques for Microwave Resonators and Filters,” in *Proceedings of the Micro and Millimetre Wave Technology and Techniques Workshop*, 2014.
[7] J. R. M. Vaughan, “Multipactor,” *IEEE Trans. Electron Devices*, vol. 35, no. 7, pp. 1172–1180, Jul. 1988.
[8] European Space Agency, “Multipactor handbook,” European Cooperation for Space Standardisation ESA-ESTEC Document,ECSS-E-HB-20-01A, 2020.
[9] W.-C. Tang and C. M. Kudsia, “Multipactor breakdown and passive intermodulation in microwave equipment for stellite applications,” in *IEEE Conference on Military Communications*, 1990, pp. 181–187.
[10] L. Qian *et al.*, “A Narrowband 3-D Printed Invar Spherical Dual-Mode Filter With High Thermal Stability for OMUXs,” *IEEE Trans. Microw. Theory Tech.*, vol. 70, no. 4, pp. 2165–2173, Apr. 2022.
[11] V. Baglin *et al.*, “The Secondary Electron Yield of Technical Materials and its Variation with Surface Treatments,” in *Proceedings of European Particle Accelerator Conference*, 2000, pp. 1–3.

CHAPTER 5: THERMAL STABILITY ANALYSIS OF 3D PRINTED RESONATORS USING NOVEL MATERIALS

Lu Qian, Sheng Li, Moataz Attallah, Talal Skaik, Paul Booth, Laurent Pambaguian, César Miquel España, Petronilo Martín-Iglesias, Yi Wang

Yi Wang suggested this work, planned, and supervised the entire study, and led the project. Lu Qian conceived the idea of this design and carried out the theoretical modelling, analysis and simulations, and performed the experiment, interpreted the data and wrote the manuscript. Paul Booth, Laurent Pambaguian, César Miquel España, and Petronilo Martín-Iglesias advised and provided guidance on this project. Sheng Li, Abd El-Moez A. Mohamed, Moataz M. Attallah assisted in the fabrication of the experimental samples. All authors contributed to the writing of the paper and reviewed the manuscript.

This chapter is based on the following publication: Thermal Stability Analysis of 3D Printed Resonators Using Novel Materials, which has been published in 2021 51st European Microwave Conference (EuMC), 2022, no. April, pp. 334–337.

Abstract

This chapter presents an investigation into the thermal stability of microwave cavity resonators using several novel alloy materials. Shaped spherical resonators are additively manufactured by Selective Laser Melting (SLM) technology from alloy powders. The manufacturing parameters of each sample is presented, and their thermal stability is experimentally characterized by measuring the RF performance under different temperatures. The Ti64, Zr702 and TNTZ samples show much improved thermal stability as compared with the common aluminium alloy used for space application. A detailed comparison between different samples in terms of their mechanical, thermal and RF performance is presented. This work introduces an expanded range of materials that may be used for microwave filters and opens opportunity for new temperature compensation techniques for high power filters.

Keywords: Additive manufacturing, cavity, filters, new materials.

5.1 Introduction

High-power microwave filters are an important class of components in satellite payloads. They are mostly used in output multiplexers (OMUXs) or antenna feeds handling power levels beyond 100W per channel from L-band up to Ka-band [1], [2]. Above X-band, most of these filters are formed of hollow metal cavity resonators for their low loss requirement. In addition, thermal conduction and lightweight performance are required, making Aluminium the preferred building material. Temperature variation is mainly due to the in-orbit operation (typically 15-85°C for OMUX) and the self-heating from the high-power RF dissipation. Without any compensation mechanism, this temperature variation would cause thermal expansion/contraction of the metal cavity and resulting in a frequency displacement of the filters response. So, most of the high-power filters require temperature compensation mechanisms. Due to its narrow bandwidth and the need to reduce the guard bands (and hence maximise the overall available frequency range utilization while reducing as much as possible the interference to adjacent channels), the channel filters in OMUXs have particularly stringent requirement in terms of thermal stability. It requires either external temperature compensation structures [3] or the use of invar alloy [4] for its extremely low coefficient of temperature expansion (CTE) of 0.5 - 2 ppm/K. The external constraint structures often complicate the assembly and result in a bulkier structure, requiring in most cases complex tuning steps. As for invar, it is not an easy material to work with due to its high density and hardness in machining. Both approaches have been used in the industry for a very long time. This work aims to find new alternative temperature compensation solutions using new materials in combination of suitable manufacturing techniques.

The advent of additive manufacturing technology (also known as 3D-printing) and the increasing adoption of this technology in space industry offer the opportunity to explore this technology together with new materials [5], [6]. 3D printing technology has several advantages: rapid prototyping of new concepts; unique capability of free-form fabrication of complex structures which are difficult or impossible for subtractive techniques; and the versatility of printing with novel materials or even multi-materials. Some tentative work has been reported previously [7], [8] on the thermal performance of 3D printed filters but focusing on polymer-based materials, which does not really address high-power applications.

In this paper, a detailed investigation into several promising alloy materials is presented. Manufacturing parameters of each material sample are discussed. Detailed material characterization and thermal-RF test at different temperatures are reported on a dimpled spherical resonator. Good correlation has been shown between the RF test results and the expected material properties. A comprehensive comparison is made.

5.2 Structure of Experimental Samples

Two types of 3D-printed samples are used in this paper to investigate the mechanical, thermal and RF properties of the different alloy materials. The regular samples are used for mechanical and CTE testing over a wider temperature range. The microwave resonator samples operating at 10 GHz are used to investigate the actual RF temperature stability over the temperature range from room temperature to around +150 °C. This temperature range is limited by the available testing setup.

The microwave resonator employed in this work is a dimpled spherical resonator which is designed for additive manufacture [9]. Figure. 5.1 presents its geometries. Different from a regular spherical resonator, the top and bottom of this spherical cavity are symmetrically squeezed to push the first higher order mode farther away from the dominant mode. Meanwhile, a higher unloaded quality factor (Q_u) than rectangular resonator can be achieved.

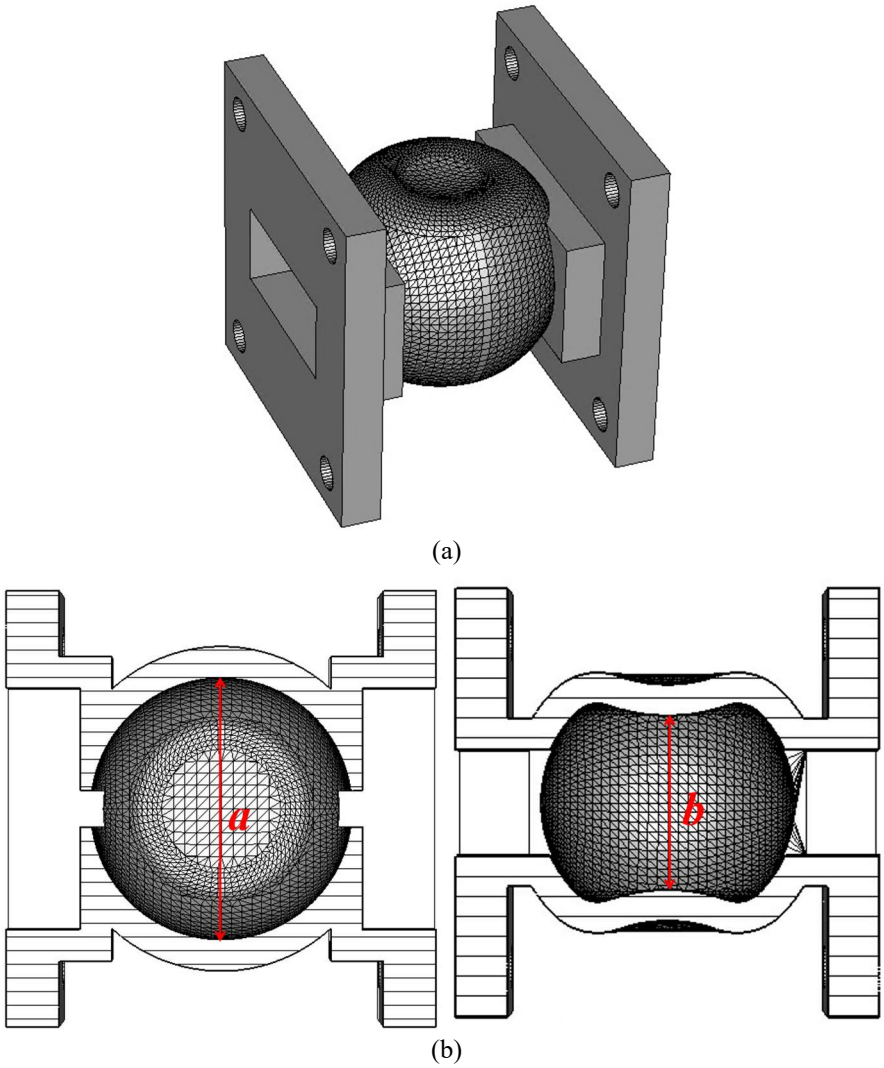

(a)

(b)

Figure 5.1 Dimpled spherical resonator. (a) Resonator geometries. (b) Cross-sections (a = 24.8 mm, b = 16.8 mm).

5.3 Material and Manufacture

5.3.1 Materials

Several promising metallic alloys are selected to manufacture the experimental resonators and regular samples, including invar alloy, Ti-6Al-4V alloy (Ti64), Ti-Nb-Ta-Zr beta-titanium alloy (TNTZ), Zr702, and the aluminium-copper alloy A20X. Among them, TNTZ and Zr702 are novel to the microwave industry. The A20X is used as the reference material, since its property is similar to the common aluminium alloy.

Invar alloy is a widely used low CTE material. However, the density of invar is high (8.1 g/cm3) and the strength-to-density ratio is low. This leads to the high weight of components made from invar, which, together with the very limited thermal conductivity, limits its application especially in payload-sensitive applications. This material is also very hard to machine. So, free-forming additive manufacturing technique offers a high-potential alternative fabrication solution. Although SLM invar [10] has been well studied, there is little work on SLM invar filters reported in the open literature.

Ti64 is a commonly used high strength alloys with high strength-to-weight ratio, which means the components may be formed thin and light weight. Ti64 is also one of the most used materials in additive manufacturing. The CTE of Ti64 is 8.6 ppm/K, much lower than aluminium but higher than Invar. Its electrical conductivity is even poorer than invar.

TNTZ alloy was originally designed and mostly used for orthopaedic implants. It has similar strength and density to Ti64. Literature has shown this alloy promises a CTE as low as 2 ppm/K after special heat treatment [11], [12]. Zr702 is close to pure zirconium. It has similar properties as titanium in many ways. Its CTE is 34% lower than Ti64. One drawback of Zr is its relatively high density but its strength is like titanium.

A20X is a high strength Al-Cu alloys with TiB2 doping. The strength of A20X is about 400 MPa but the density is low, hence the components made from A20X can be light weight. However, the CTE of Al-Cu alloys is much higher than the others.

The general properties of these selected materials are summarised in Table 5.1. The data are mostly from the literature, which will provide a reference for comparison with the actual material characterization and RF experimental results in this paper.

Table 5.1 General Properties of the Selected Materials

	Invar	TNTZ	Zr702	Ti64	A20X
Density (g/cm^3)	8.1	4.5-5	6.5	~4.4	2.85
Young's modulus (GPa)	140	36-52	95	110	75
Elongation (%)	45	10-20	5-18	5-18	>10
CTE (ppm/K)	0.5-2.0	-2.5 - +3.8	8.6	8.6	20.4
Thermal Conductivity (W/(m·K))	12-15	~ 7.8	6.7	6.7	175

5.3.2 Manufacturing Techniques

All samples are additively manufactured using laser powder bed fusion (L-PBF) technique, also known as selective laser melting (SLM). Three different types of machines are used in this study. Table 5.2 summarizes the printers and the main processing parameters.

Table 5.2 Printing Machines and Processing Parameters

	Ti64	Invar, TNTZ, Zr702	Zr702
Printer	RenAM 500 M	Concept Laser M2	SLM500HL
Layer thickness (μm)	30	30	30
Laser power (W)	200	400	360
Scan speed (mm/s)	1500	4000	1500
Hatch distance (mm)	0.105	0.45	0.15
Spot size (μm)	70-75	70-80	70-80

The printing direction is parallel to the longitude of the microwave resonator components as shown in Figure. 5.2. Samples were cut off from the substrate via EDM and the cut surface was mechanically ground. The post polishing was done by Sharmic vibration polishing machine with 3 mm size ceramic particle media. The standard polishing process takes 6 hours, and the samples are ultrasonic cleaned with ethanol for 10 min and dried in oven at 100°C for further testing. Our RF measurements are performed on as-printed samples. Figure 5.3 shows the pictures of the as-printed sample resonators from the five different alloy materials.

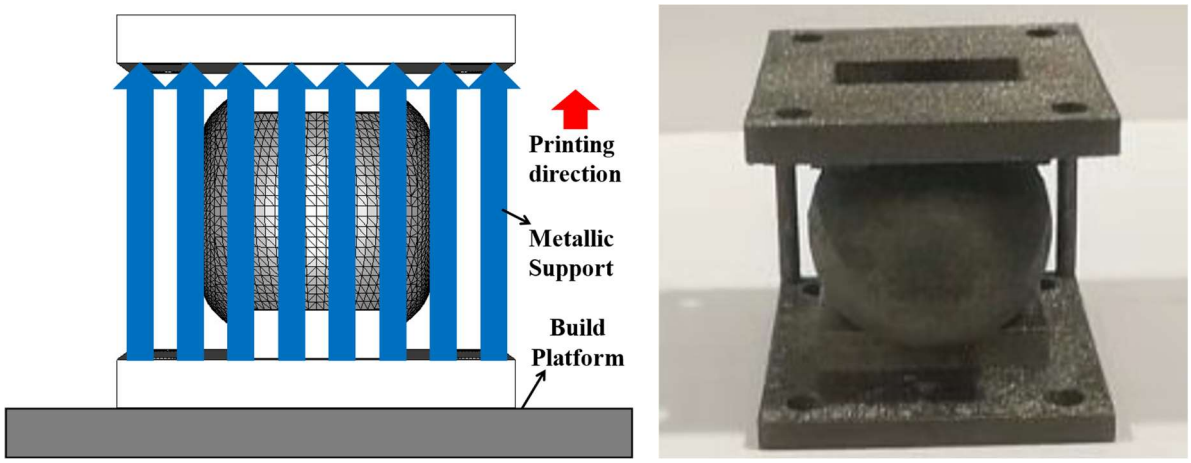

Figure 5.2 (a) Diagram showing the printing direction. (b) Photo of the printed resonator sample with external supporting structures.

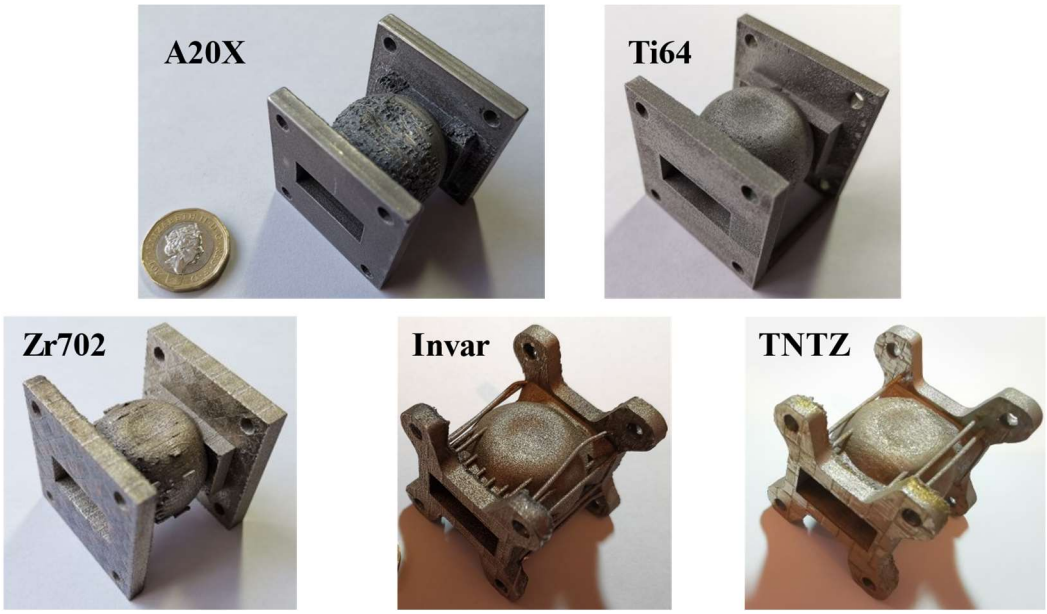

Figure 5.3 Photographs of the as-printed sample resonators.

5.4 Experimental Setup and Results

To accomplish the resonator-based thermal test, an experimental setup was built. It mainly contains four parts: heat source, thermal shielding and thermometer, a pair of thermal isolators, and RF measurement equipment. Figure. 5.4 presents the schematic diagram of the measurement setup.

A Gallenhamp hot plate is employed here as heat source. The thermal shield is made up of a box covered by aluminium foil, while the real-time temperature is monitored by a multimeter (ATP MY-64) through a K-type thermocouple. The functionality of the thermal isolator is to separate the RF measurement equipment from the heat source [13]. Each thermal isolator is composed of two sections of X-band rectangular waveguide that are separated by a 1-2 mm air gap. To avoid the radiation from the gap, periodic bandgap structure is used between the two waveguide flanges. Agilent E8361C network analyser is used. Although the in-house

built setup cannot match the accuracy of a commercial thermal chamber in temperature control, the results are adequately indicative of the thermal performance of the devices.

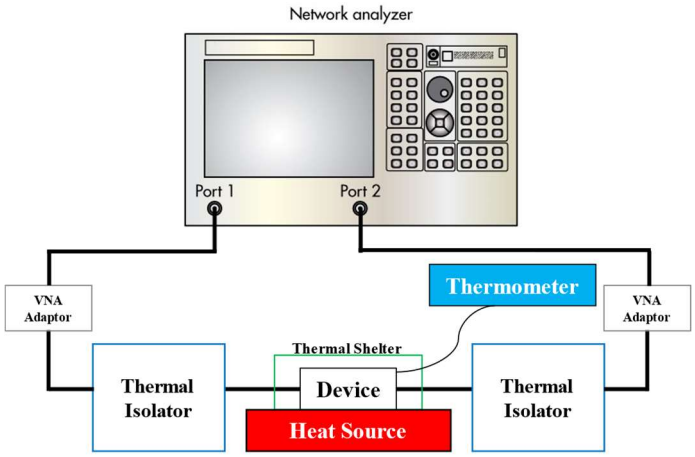

Figure 5.4 Schematic diagram of the thermal measurement setup

During the test, a set of transmission response at room temperature (around 20 ℃) were first taken as a benchmark as shown in Figure. 5.5(a). This serves a first-order indication of the dimensional accuracy of the as-printed resonators. All samples have a slightly higher resonance frequency than expected by simulation. This could be partially alleviated by predesign compensation for the dimension. Figure. 5.5(b) compares the measured quality factors of the samples at room temperature where some samples have been polished. As can be observed, the low CTE materials generally have very low Q_u, which necessitate conductivity-enhancing coating in order to achieve the required RF performance. Polishing has shown some limited positive effect.

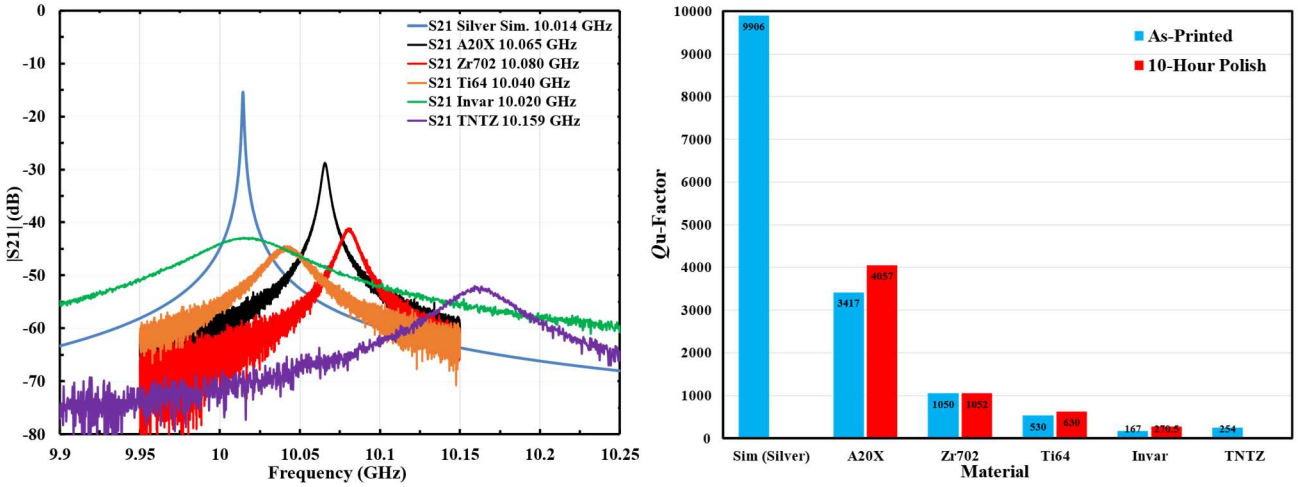

(a) (b)

Figure 5.5 (a) Measured resonance curves at room temperature. (b) Comparison of the measured Q_u of the as-printed resonators.

Temperature was then raised up to around 160 ℃ at an interval of around 20 ℃. The resonator's scattering coefficients were measured at each temperature after a stabilization time of 30 - 40 minutes. Figure. 5.6(a) shows the measured resonance curves as a function of temperature for the A20X sample, where the frequency shift is clear. Theoretically, the percentage frequency shift is approximately equal to the CTE times the

temperature range. That is $\Delta f / f \approx$ - CTE × Temperature-range. However, the CTE of the bulk material is not identical to that of the resonator. We define the 'effective temperature coefficient' of the resonator as $d(\Delta f/f)/dT$. It has the same unit of ppm/K as the CTE of the materials. Shown in Figure. 5.6(b) is an example for A20X sample where the start and end temperature are used to extract the effective temperature coefficient. For comparison, Figure. 5.7 presents the measured resonance curves and calculated effective temperature coefficients of the other four resonator samples formed of lower CTE materials. The improvement in the thermal stability of the resonator is significant.

Table 5.3 Test Result Summary of As-printed Resonator Samples

Materials	Literature	Flat Sample (As-printed)	10 GHz Resonator (As-printed)	
	CTE (ppm/K)	CTE (ppm/K) @25-140°C	Freq. temp. coefficient (ppm/K) @20-150°C	Q_u @20°C
Invar	0.5-2	1.43	1.85	167
TNTZ	-2.5 - +3.8	8.26	7.68	254
Zr702	5.7	7.32	5.95	1050
Ti64	8.6	8.48	7.43	530
A20X	20.39	19.05	21.16	3417

Additionally, the CTE of the materials was measured by the TA Instruments TMA 2940 Thermo-Mechanical Analyzer, generally in accordance with BS ISO 11359-2:1999. Good correlation between the measured CTE of the materials and the measured effective temperature coefficient of the resonators has been shown in Table 5.3. However, the TNTZ samples show much higher CTE than the literature value [11]. It is known the CTE of TNTZ is highly dependent on the manufacture process and heat treatment.

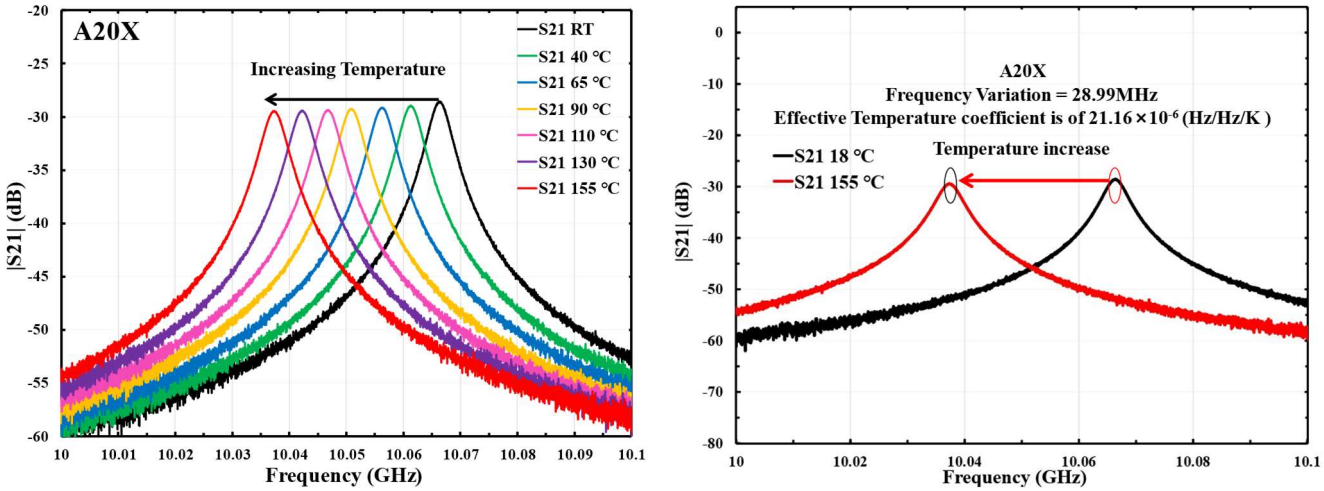

(a) (b)

Figure 5.6 A20X resonator: (a) Measured resonance curves as a function of temperature; (b) Calculated effective temperature coefficient.

5.5 Conclusion

This chapter evaluated the thermal stability of microwave cavity resonators, additively manufactured using several alloy materials with low CTE. Ti64, Zr702 and TNTZ show much improved temperature stability compared with aluminum. Most temperature-dependent RF measurement results show good correlation with

the expected CTE properties of the materials. The TNTZ sample did not reach the lowest CTE reported in the literature, which requires further investigation. The work also demonstrated the printability of monolithic and irregular shaped resonators using these new materials. This increases the range of materials that may be used for microwave filter and opens opportunity for new temperature compensation mechanism for high power filters. Future work is expected for the manufacturing of complex RF functions, making benefit of the selection of highly stable building materials. End-to-end manufacturing methods will be investigated considering, for example, the required metal coating for RF performance improvement.

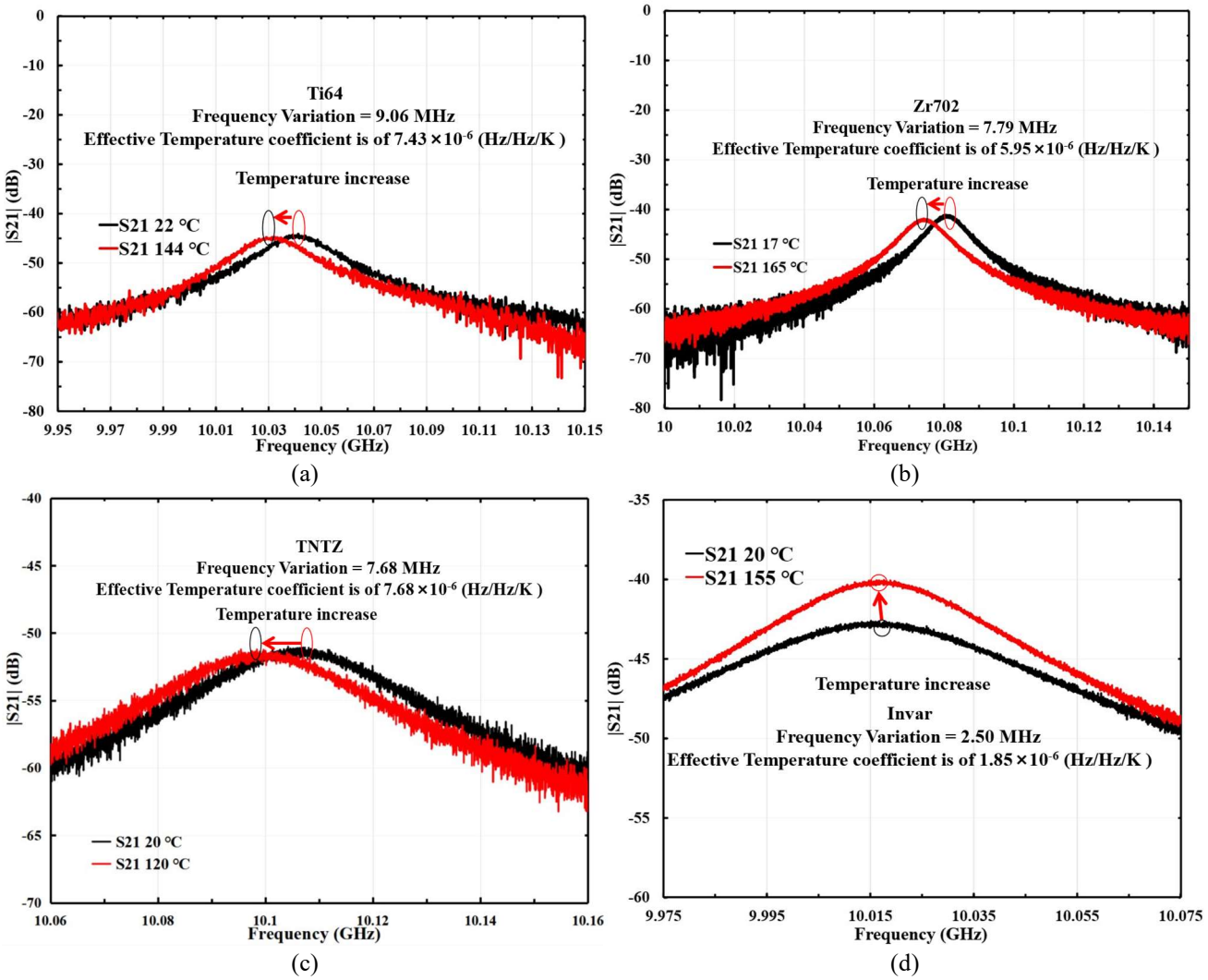

Figure 5.7 Resonance curves used to calculate the effective temperature coefficients for the as-printed sample resonators with low CTE materials. (a) Ti64, (b) Zr702, (c) TNTZ, (d) Invar.

Reference

[1] V. E. Boria and B. Gimeno, "Waveguide filters for satellites," *IEEE Microw. Mag.*, vol. 8, no. 5, pp. 60–70, 2007.

[2] C. Kudsia, T. Stajcer, and M. Yu, "Evolution of Microwave Technologies for Communications Satellite Systems," in *34th AIAA International Communications Satellite Systems Conference*, 2016.

[3] Ming Yu, D. J. Smith, A. Sivadas, and W. Fitzpatrick, "A dual mode filter with trifurcated iris and reduced footprint," in *2002 IEEE MTT-S International Microwave Symposium Digest (Cat. No.02CH37278)*, 2002, vol. 3, pp. 1457–1460.

[4] B. Yassini and M. Yu, "Ka-Band Dual-Mode Super Q Filters and Multiplexers," *IEEE Trans. Microw. Theory Tech.*, vol. 63, no. 10, pp. 3391–3397, Oct. 2015.

[5] P. Booth, J. Gilmore, E. V. Lluch, and M. Harvey, "Enhancements to satellite feed chain performance, testing and lead-times using additive manufacturing," *2016 10th Eur. Conf. Antennas Propagation, EuCAP 2016*, 2016.

[6] P. Booth, R. Roberts, M. Szymkiewicz, and C. Hartwanger, "Using additive manufacturing for feed chain and other passive microwave components," *2017 11th Eur. Conf. Antennas Propagation, EUCAP 2017*, pp. 558–562, 2017.

[7] C. Guo, J. Li, D. D. Dinh, X. Shang, M. J. Lancaster, and J. Xu, "Ceramic filled resin based 3D printed X-band dual-mode bandpass filter with enhanced thermal handling capability," *Electron. Lett.*, vol. 52, no. 23, pp. 1929–1931, 2016.

[8] G. P. Le Sage, "Thermal frequency drift of 3d printed microwave components," *Metals (Basel).*, vol. 10, no. 5, p. 580, Apr. 2020.

[9] C. Guo *et al.*, "Shaping and Slotting High-Q Spherical Resonators for Suppression of Higher Order Modes," *IEEE MTT-S Int. Microw. Symp. Dig.*, vol. 2019-June, pp. 1205–1208, 2019.

[10] C. Qiu, N. J. E. Adkins, and M. M. Attallah, "Selective laser melting of Invar 36: Microstructure and properties," *Acta Mater.*, vol. 103, pp. 382–395, 2016.

[11] M. Nakai, M. Niinomi, T. Akahori, H. Tsutsumi, X. Feng, and M. Ogawa, "Anomalous thermal expansion of cold-rolled Ti-Nb-Ta-Zr alloy," *Mater. Trans.*, vol. 50, no. 2, pp. 423–426, 2009.

[12] M. A.-H. Gepreel, M. Niinomi, M. Nakai, and M. Morinaga, "Invar Properties in Ti-Alloys Achieved Through Alloy Design and Thermomechanical Treatments," *JOM*, vol. 71, no. 10, pp. 3631–3639, Oct. 2019.

[13] J. Hesler, A. R. Kerr, and N. Horner, "A broadband waveguide thermal isolator," *14th Int. Symp. Sp. Terahertz Technol.*, pp. 148–154, 2003.

CHAPTER 6: LIGHTWEIGHT, HIGH-Q AND HIGH TEMPERATURE STABILITY MICROWAVE CAVITY RESONATORS USING CARBON-FIBER REINFORCED SILICON-CARBIDE CERAMIC COMPOSITE

Lu Qian, Yeshodhara Baskaran, Matthias Krödel, César Miquel España, Laurent Pambaguian, Talal Skaik, Yi Wang

Yi Wang suggested this work, planned, and supervised the entire study, and led the project. Lu Qian conceived the idea of this design and carried out the theoretical modelling analysis and simulations, and performed the experiment, interpreted the data, and wrote the manuscript. Laurent Pambaguian and César Miquel España advised and provided guidance on this project. Yeshodhara Baskaran, Matthias Krödel assisted in the fabrication of the experimental samples. All authors contributed to the writing of the paper and reviewed the manuscript.

This chapter is based on the following publication: Lightweight, High-Q and High Temperature Stability Microwave Cavity Resonators Using Carbon-Fiber Reinforced Silicon-Carbide Ceramic Composite, which has been accepted by IEEE J. Microwaves, no. August, pp. 1–7, 2023, Doi: 10.1109/JMW.2023.3305180.

Abstract

This chapter for the first time presents a high-Q cavity resonator manufactured using carbon-fiber reinforced silicon carbide (SiC) ceramic composite material HB-Cesic®. This composite has attractive properties of low coefficient of thermal expansion comparable to Invar, low density similar to aluminum, and high thermal conductivity. Its manufacturing process enabled by machining and joining renders useful design flexibility. A high-Q spherical resonator has been used as an example in this investigation. Two resonators, one monolithic version and the other one based on split-block structure have been experimented. The end-to-end processes from machining, assembly or joining, to high-conductivity coating for both structures, have been demonstrated. The RF performance of the resonators and their variation with temperature have been measured. A quality factor of over 10000 has been achieved for both resonators at 11.483 GHz. The measured high thermal stability of the resonator correlates very well with the prediction. This work establishes the feasibility of using HB-Cesic® in microwave resonators and paves the way for further development and verification programme for more complex passive microwave devices such as filters and multiplexers for space applications.

Keywords: High-power microwave, invar alloy, novel materials, silicon carbide, spherical resonators, space technology, thermal stability.

6.1 Introduction

The development of satellite communication technology, especially the advent of high-throughput-satellite (HTS) systems has spurred increasing demand for high-performance microwave devices [1]. Among them, output multiplexers (OMUXs) are one of the most complex and specialized passive components. An OMUX usually consists of a set of narrowband output filters and is placed after high-power amplifier to combine multiple amplified signals into a common transmission antenna. As a result, the low insertion loss and high power-handling capacity are key design parameters. Additionally, OMUXs requires very stable RF performance over a wide temperature range. Both the self-heating effect induced by power dissipation and the operating temperature range pose significant challenge to maintaining good thermal stability of the overall filter [2], [3]. Therefore, the high quality-factor (Q) and high temperature-stability filters are a crucial component for satellite communication systems.

To achieve the low insertion-loss, high-Q resonators are needed. Many cavity resonators have been invented, such as the TE_{011} single mode cylinder resonator, TE_{11N} (N = 1 - 5) and TE_{221} dual-mode cylinder resonators [4]. Enabled by the emerging additive manufacture (AM) technology, some irregular shaped resonators, such as super-ellipsoid and spherical cavity resonator, were also reported [5]–[11].

For the stringent thermal stability requirement, two methods have been widely adopted. The first method relies on the temperature-invariant material like Invar, which has very low coefficient of thermal expansion (CTE) of 1-2 ppm/K [12]. However, its poor manufacturability due to hardness, high density, and low thermal conductivity are significant barriers to their widespread application, particularly as more microwave components are required in emerging satellite internet constellation systems. The second method uses external temperature compensation [13], [14]. Often external fixture or additional compensation structures are required. This can complicate the assembly. A lot of the compensation fixtures are made from Invar. To address the manufacturability issue with Invar, 3-D printing has been used to manufacture Invar filter and diplexer [15]–[17]. Recently, we have reported some investigative work on using novel low-CTE alloy materials to manufacture thermally stable microwave components [18]. However, so far none of the metal materials can match the low CTE of Invar.

Non-metal materials that can match the CTE of Invar are some ceramic based materials and carbon-fibre-reinforced polymers (CFRPs). CFRP is an interesting material for high power applications. It has low density, high specific stiffness and a very low CTE down to -0.4 ~ 0.76 ppm/K. However, its anisotropic properties often complicate the microwave design. This material has been used in antennas for space applications, as well as in circuit packaging. One major challenge with this material is the metal coating. CFRP is conductive but has a very low conductivity. CFRPs have been reported for filters applications [19]. One other high-power filter based on a similar material was originally reported in 1974 [20] and reviewed in 2016 [21]. The material used was Graphite Fiber Epoxy Composite (GFEC), with a CTE similar to Invar but a ~50% weight reduction. The work also highlighted the anisotropic issue of the material and consequentially the restriction on the design.

Silicon carbide (SiC) is a family of compound semiconductor consisting of silicon and carbon. Because of its unique crystalline structures, SiC has excellent physical properties such as high electric field breakdown strength, high maximum current density, and high thermal conductivity. It has been used in electronic industry including power electronics [22], photonics [23] and is regarded as a promising substrate for high-temperature quantum devices [24]. Carbon-fiber reinforced silicon carbide is a ceramic composite material. This material has high hardness and stiffness, high thermal conductivity, and low coefficient of thermal expansion. It also overcomes the anisotropic issue with CFRP, capable of producing uniform and isotropic structures. HB-Cesic® is such a material developed by ECM - Engineered Ceramic Material GmbH [25]. Its low CTE, light weight and high thermal conductivity offer almost a perfect combination for high temperature-stability

microwave components. Table 6.1 summarises the comparison of the thermal and mechanical property between HB-Cesic® and Invar alloy as well as the aluminum alloy (A20X).

This work, for the first time, investigated the feasibility of HB-Cesic® in microwave passive components. The manufacturing process for microwave components will be explored. Both the material itself and the manufacturing processes are a novelty for the microwave community. A spherical resonator has been used as an example in this investigation. Compared with rectangular cavity resonators, the spherical resonators have higher quality factor and wider spurious-free window, while the curved surface presents a demanding test structure to verify the feasibility of the proposed manufacturing approach. Two resonators, one based on a single-piece (monolithic) build and the other on a two-piece (split-block) structure, have been experimented. The end-to-end manufacturing process has been demonstrated. Experimental characterization is performed to investigate the RF performance and thermal stability. The measurement result exhibits a good correlation with the theoretical prediction.

Table 6.1 Mechanical and Thermal Properties

Mechanical & Thermal Properties	HB-Cesic® [25]	Invar [15]	A20X [18]
Density (g/cm^3)	2.96	8.1	2.85
Young's modulus (GPa)	350	140	75
CTE (ppm/K)	2.3	0.5-2	20.4
Thermal Conductivity (W/(m·K))	200	15	175

6.2 Spherical Resonator

Figure. 6.1 illustrates the configuration of the spherical resonator, where both the monolithic and the split-block version are shown. The resonator consists of a spherical cavity and two WR-90 waveguide ports. The dominant mode TM_{101}, resonating at 11.483 GHz, is weakly coupled through the narrow coupling iris. The unloaded quality-factor (Q_u) value is calculated to be 11075, assuming the conductivity of perfectly smooth gold (4.56×10^7 S/m).

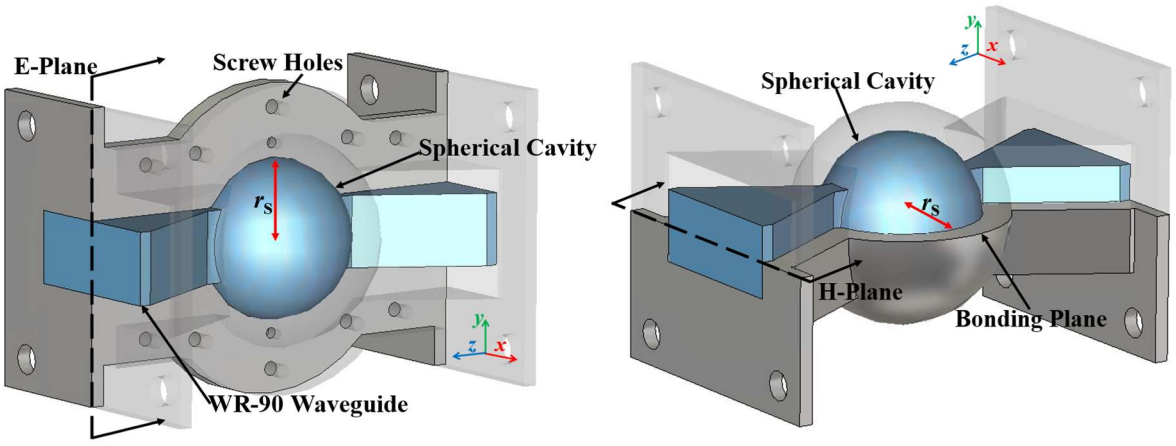

(a) (b)

Figure 6.1 Configuration of two spherical resonators, where half of the metallic wall is rendered with translucent colour to aid visualization. The blue colour represents the air cavity. (a) Split-block resonator, (b) Monolithic resonator.

For the split-block spherical resonator (see Figure. 6.1(a)), the resonator is formed of two identical parts that are bolted together, along the E-plane of the rectangular waveguide port to reduce the disturbance to the surface current and therefore its sensitivity to assembly. Figure. 6.1(b) shows the monolithic spherical resonator. It should be noted that it was glued together from two identical parts along the H-plane. In this structure, H-plane is not normally the preferred cut. However, the bonding technique used for the HB-Cesic® material promises to eliminate the usual problem associate with imperfect contacts between two parts. This monolithic resonator structure serves to test the robustness of the manufacture technology, which will be discussed in more detail later.

6.3 Fabrication

Figure. 6.2 presents the flowchart outlining the manufacturing process of HB-Cesic® parts. The process is divided into several sequential steps, as follows: (1) Preparation of carbon fiber (CF) mixtures. In this step, CF will be mixed with resin and other carbon powders. (2) Fabrication of carbon/carbon (C/C) raw material. The C/C raw material is formed by pressing CF mixtures to a solid block. (3) CNC machining the C/C blocks to form the desired structure (greenbody) using diamond tools. (4) Liquid silicon infiltration. The greenbody parts are infiltrated by liquid silicon and then fired at high-temperature furnace to form the final HB-Cesic® parts. (5) Final machining of interfaces or functional surfaces. The manufacturing process offers several advantages over conventional ceramic materials. For instance, the C/C greenbody is not fragile, allowing for the production of very thin walls and the creation of ribs with a diameter of 1 mm and height of 100 mm. The infiltration is a solid-to-solid process resulting in no shrinkage. Consequently, it helps to mitigate geometry inaccuracies caused by sintering. Furthermore, the manufacturing process facilitates the formation of complex monolithic closed structures by joining separately machined greenbody parts using glues prior to silicon infiltration. The joining technology uses a non-commercial adhesive, which has a very similar microstructure as the C/C material. At the stage of applying, the adhesive is a pasty material and curing will get hard. In the following high temperature process the adhesive will be converted with silicon to the same material as the bulk C/C material showing no difference in mechanical and thermal properties. Micrographic analysis also indicates no discontinuity in the joining area.

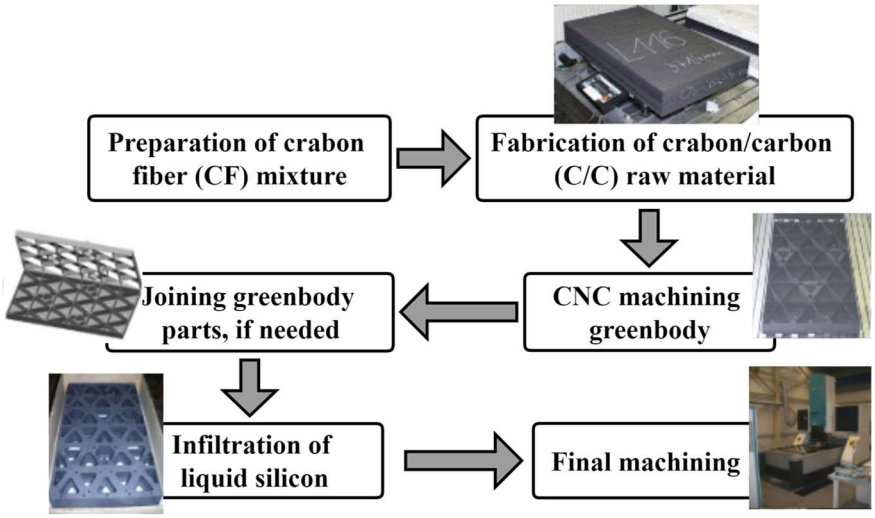

Figure 6.2 Flowchart of the manufacturing process of HB-Cesic® parts.

HB-Cesic® has a very low electrical conductivity of 28.7 S/m. So, metal coating is imperative. This material has been used in antenna reflectors [26]. Copper coating was applied by magnetron sputtering on the open structures. For the closed structures like the resonator, there is no established coating process reported in the open literature. We have experimented and applied electroless copper plating to both the open structure split-block and the closed monolithic resonator. The measured RF performance (discussed in the next section) has indicated full coverage and good quality of the coating. The electroless process is limited in achievable thickness. Only 1 - 2 mm coating was achieved. This has been thickened up by electroplating copper and passivated with a thin gold finishing. The as-fired surface roughness of HB-Cesic® parts is typically less than 8 µm. This is higher than CNC machined surface, but comparable to 3D printed metal surfaces. For the two resonators, the measured average surface roughness before and after plating is 2.1 µm and 1.7 µm. The measured RF performance again indicates the impact on the losses is not significant for the X-band resonator. Figure. 6.3 shows the pictures of both HB-Cesic® spherical resonators, as-manufactured and after gold plating respectively. The wall thickness of both resonators is 4 mm except that the flange thickness of the monolithic resonator is reduced to 2 mm.

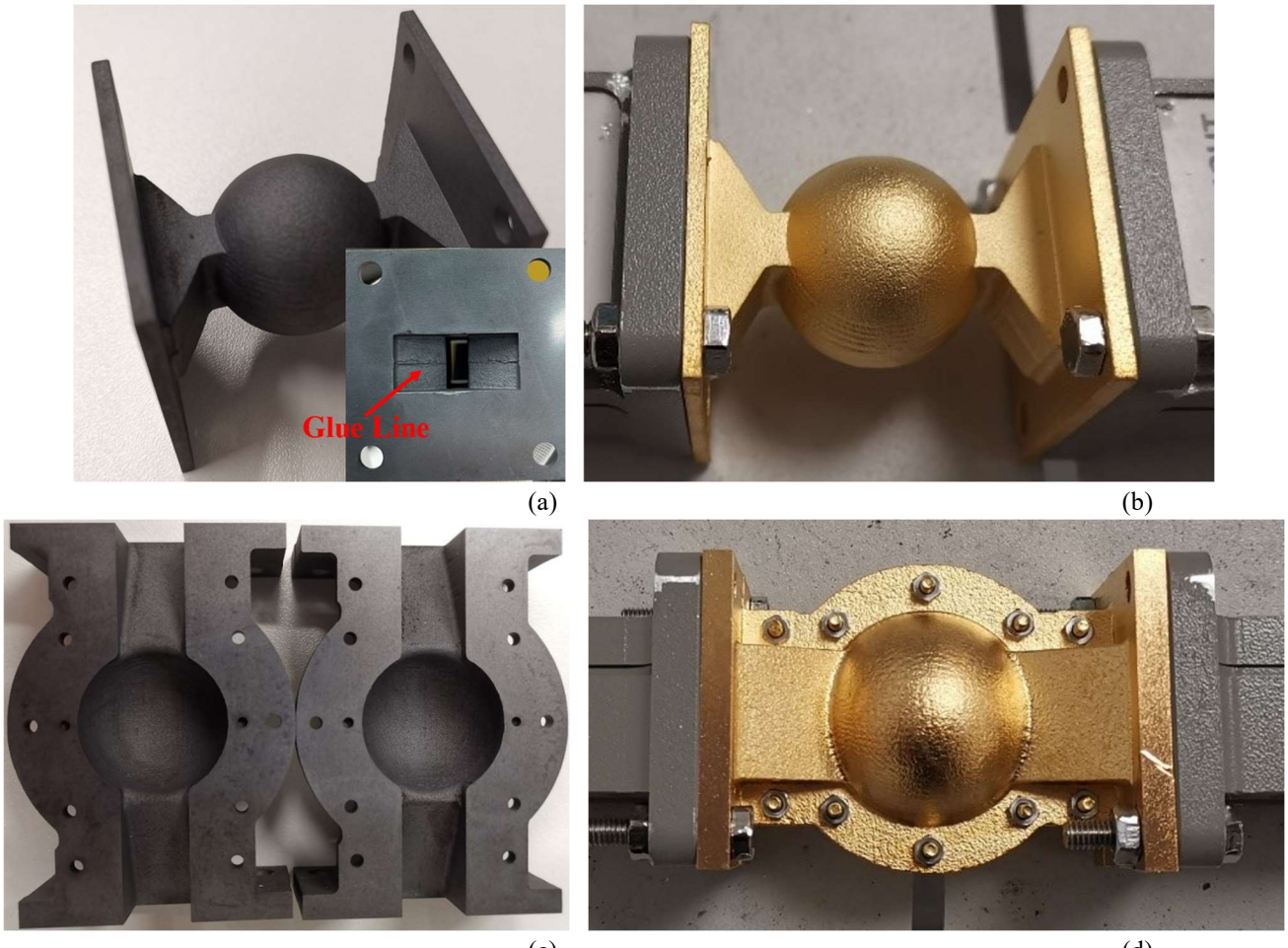

Figure 6.3 Photograph of the two HB-Cesic resonators. (a) Monolithic resonator (before coating), (b) Monolithic resonator (after coating), (c) Split-block resonator (before plating). (d) Split-block resonator (after plating).

6.4 Measurement and Discussion

To validate the material and manufacturing technology for high-power microwave components, both RF and thermal-RF tests were carried out.

6.4.1 RF Measurement

All RF measurements were performed on Agilent E8361C PNA network analyser. The analyser was calibrated using TRL (Thru, Reflect, Line) method. To achieve accurate Q measurements, the intermediate frequency of the sweep was set to be 100 Hz. Figure. 6.4 shows the measured and simulated transmission response (S_{21}) of the resonators. The measured Q_u, extracted using 3-dB method, of the monolithic resonator is 10664. This is 10436 for the split-block resonator. Both values are very close to the simulated Q_u of 11075 based on a perfect conductivity of gold. This means the hybrid plating techniques can achieve very good electrical conductivity. This also indicates the assembly plane of the split-block resonator has very small impact on Q_u. It should be noted that the Q extracted using 3-dB method is practically the loaded quality-factor (Q_L), but it nearly equals to Q_u for the very weakly coupled resonators. To improve the accuracy of the extraction, the bandwidth of the frequency sweep is limited to only 3 to 5 times of the 3-dB bandwidth. For the split resonator, the resonance frequency is shifted downward by 117 MHz to 11.336 GHz. There is a spurious spike at 11.2 GHz. For the monolithic resonator, the resonance only shifts slightly up by 7 MHz. Two spurious spikes appear at 11.2 GHz and 11.58 GHz. Because the spherical resonator supports three degenerate modes and high-order modes, the spurious spikes are mostly likely a result of geometry deviation that breaks the symmetry and excites the unwanted modes. This has been investigated using simulation analyses next.

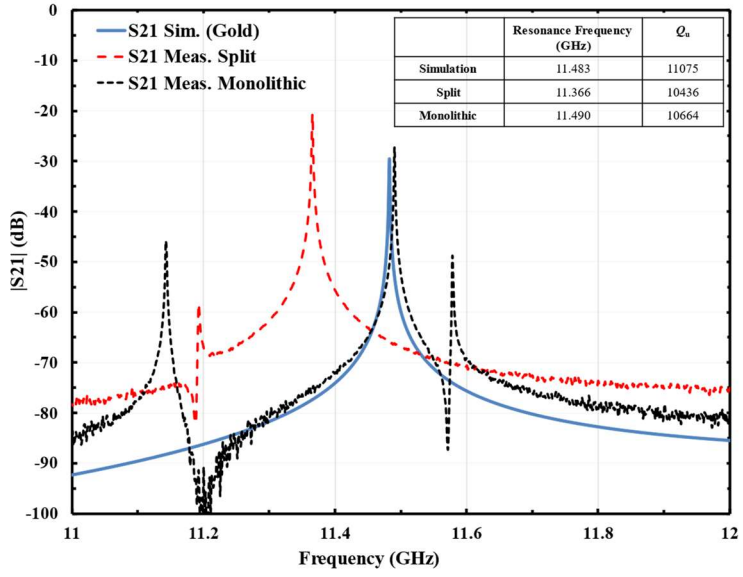

	Resonance Frequency (GHz)	Q_u
Simulation	11.483	11075
Split	11.366	10436
Monolithic	11.490	10664

Figure 6.4 Measured and simulated result of the two resonators with inset showing the comparison of resonance frequency and Q_u.

Figure. 6.5 presents the main results from this investigation where several possible manufacturing and assembling errors were considered. For the split-block resonator, we first look at the displacement between the two halves as shown in Figure. 6.5(a), along the Y-axis (denoted by d_Y), while the spherical radius r_S is increased from 11.34 mm to 11.425 mm to account for the frequency shift. It is clear the intended resonance frequencies agree well after this modification, while a spurious spike can be observed in the lower band. The simulated Electric-field (E-field) distribution at the resonance and the spike frequency are presented in the

inset. It shows the dominant and the spurious mode correspond to the degenerate TM_{101} mode. The small frequency difference between the simulated and measured spikes might be caused by other asymmetries of the spherical resonator such as the unequal radius along *X*-axis or *Y*-axis. It is expected the spurious spikes can be mitigated by reducing the displacement d_Y during assembly.

For the monolithic resonator, three possible cases are considered. As illustrated in the inset of Figure. 6.5(b), the first is a bulge along the bonding plane (denoted by r_B) from the glue line as shown in the inset of Figure. 6.2(a). The other two are the displacement along *X*-axis (d_x) and *Z*-axis (d_z). The simulation responses from the modified resonator model show an excellent consistency with the measurement results. According to simulation analysis, the slight upper shift of the intended resonance frequency is mainly caused by the bonding bulge (r_B). Looking at the simulated E-field pattern, we can find the lower spike is derived from the degenerate TM_{101} mode due to the displacement in *X*-axis while the higher spike resembles the degenerate TM_{101} mode due to the displacement in *Z*-axis. It is expected these spurious modes can be suppressed by improving the accuracy of the joining and eliminating the glue line. Changing the bonding plane to the E-plane could also reduce the risk of spurious spikes.

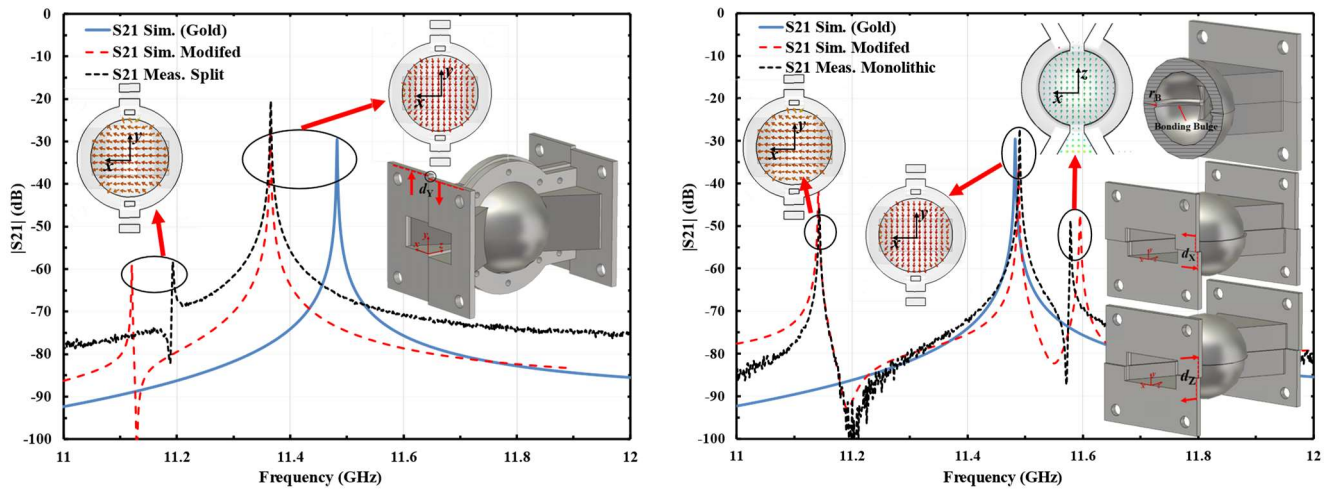

(a) (b)

Figure 6.5 Comparison between the measured and simulated transmission responses with inset showing the modified resonator model considering the manufacturing and assembling errors, and the simulated E-field cross-section at the resonator centre. (a) Split resonator, d_Y = 0.05 mm. (b) Monolithic resonator, r_B = 0.85 mm, d_X = 0.09 mm, and d_Z = 0.17 mm.

6.4.2 Temperature-dependent RF Measurement

To verify the thermal stability of the HB-Cesic® microwave components, the temperature-dependent RF measurement was performed. The experiment process is similar to that in [18]. However, as shown in Figure. 6.6(a), a 3D-printed Invar waveguide spacer was inserted between the HB-Cesic® resonator and the aluminium test port to mitigate the thermal stress that could be induced by the mismatched CTE of the ceramic part and aluminium ports. Figure. 6.6(b) presents the comparison of measured effective temperature coefficient (ETC) [17] between the two resonators, where the inset is the measured transmission responses as a function of temperature for both resonators. The ETC is calculated using the frequency shift and temperature interval between two consecutive temperature points. During the measurement, 5 MHz frequency-sweep bandwidth is applied to all temperature points to ensure accuracy of the extracted resonance frequency. Both resonators show good thermal stability (ETC < 3 ppm/K) up to 80 °C, the typical maximum operating temperature of common OMUXs. The ETC of the monolithic resonator is less than 2 ppm/K. These results are comparable to the measured CTE of 2.3 ppm/K of the bulk Cesic material. The monolithic resonator has

an ETC below 3 ppm/K up to 160 °C. The ETC of the split-block resonator is higher and rises to 6 ppm/K at 160 °C. The considerable increase of its ETC above 100 °C is believed to be attributed to the aluminium screws used to bolt the two halves. This effect may be reduced by using Invar or Cesic screws. Figure. 6.6(c) shows the variation of Q_u versus the temperature. A decreasing trend can be observed, but the Q_u is still great than 9000 up to 160°C for both resonators. This still leaves adequate design margin for the channelizing filters in OMUXs, where the desired Q_u is usually around 6000.

For comparison, a 3-D printed Invar spherical resonator with identical internal dimensions and 2 mm wall thickness was manufactured and measured. The Invar resonator was plated with silver. Table 6.2 summarises the comparison. The HB-Cesic® resonators exhibit a clear advantage in terms of the weight and the achievable Q_u. The monolithic resonator realizes 74% mass reduction while achieving 39% increase in Q_u. Even in the case of the split resonator, the improvements in weight and Q_u are 62% and 31%, respectively. Considering the thermal stability, we find that the HB-Cesic® resonators can achieve slightly higher ETC values than Invar resonator. These values are still competitively low and can be used to meet the typical thermal-stability requirement for high-power devices like OMUXs.

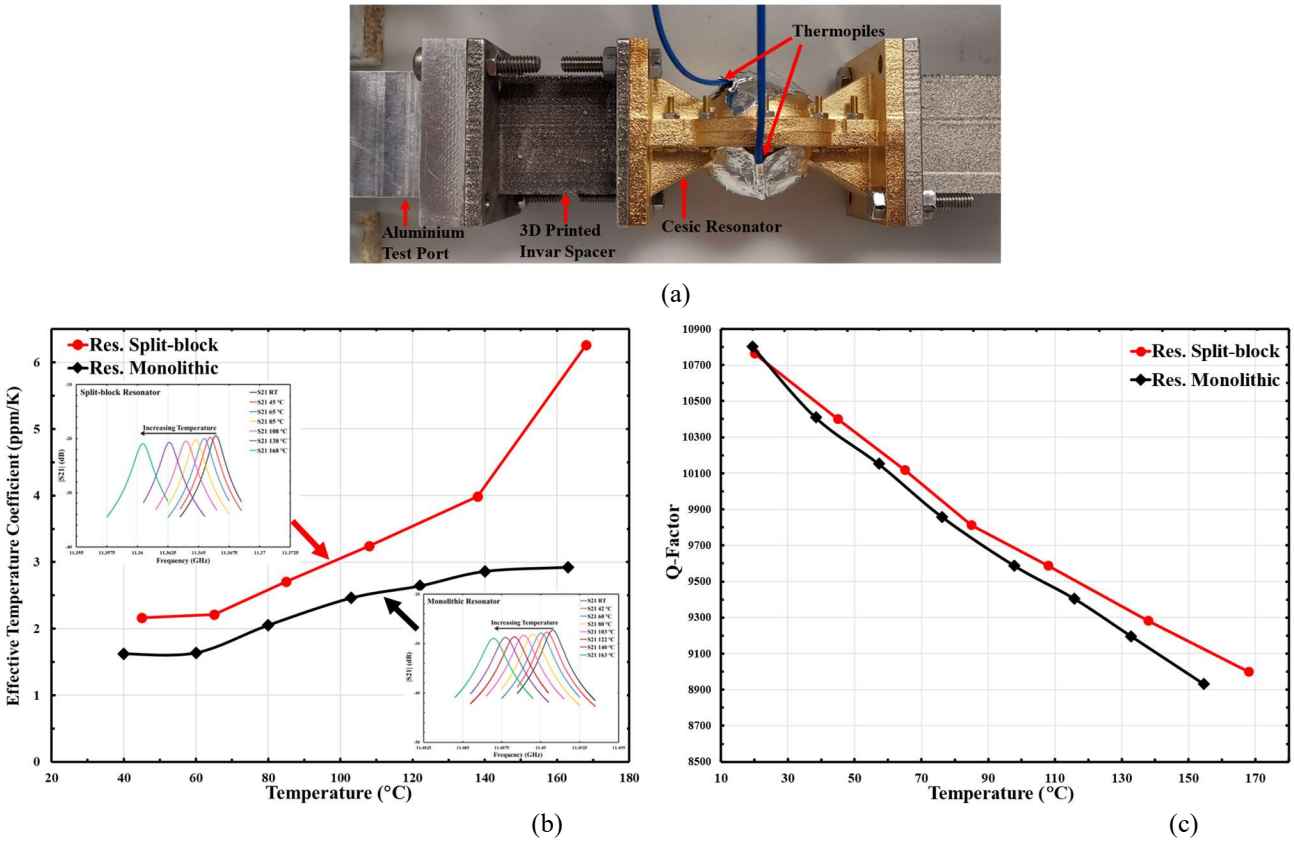

Figure 5.6 Thermal-RF measurement results as a function of temperature. (a) Resonator under test; (b) Effective temperature coefficient with inset showing the measured transmission responses at different temperatures for both resonators; (c) Unloaded quality factor (Q_u).

Table 6.2 Comparison of the HB-Cesic and Invar Resonators

	Weight (g)	Q_u (R.T. / 85°C)	Freq. temp. coefficient (ppm/K)
Monolithic Cesic	31	10664 / 10131	1.77
Split-block Cesic	45	10436 / 9483	2.36
3-D Printed Invar	117	7995 / 7454	1.01

Table 6.3 provides a comparison with published high-Q spherical resonators. As can be observed, the HB-Cesic® spherical resonators achieve the highest Q_u among all measurement results. While higher-order resonance modes could potentially achieve even higher Q_u than the dominant mode used in this work, spurious modes nearby would limit their practical application, particularly when wide stopband is required. Moreover, the novel HB-Cesic® material not only improves thermal stability but also reduces weight compared with Invar and many other metallic materials.

Table 6.3 A Comparison with Published High-Q Spherical Resonators

Ref.	Resonator Type	Resonance Mode	f_c (GHz)	Q_u (Sim./Meas.)	Manufacture Technology	Material
[7]	Spherical resonator	TM101 (Dominant Mode)	10	14450/-	3-D Printing	Polymer (Copper plating)
[8]	Squeezed spherical resonator	TM101 (Dominant Mode)	10	6820/3728	3-D Printing	Al-Cu alloy
[5]	Depressed super-ellipsoid resonator	TM101 (Dominant Mode)	12.875	6102/4300	3-D Printing	Scalmalloy aluminium alloy
[9]	Spherical resonator	TM211 (Higher-order Mode)	31	7393/493	3-D Printing	AlSi10Mg alloy
[10]	Spherical resonator	TE101 (Higher-order Mode)	10	23000/4500	3-D Printing	AlSi10Mg alloy
[11]	Spherical resonator	TE101 (Higher-order Mode)	10	23000/1200	3-D Printing	Polymer (Copper plating)
[17]	Spherical resonator	TM101 (Dominant Mode)	11.483	12500/5800	3-D Printing	Invar alloy (Silver plating)
T.W.	Spherical resonator	TM101 (Dominant Mode)	11.483	11075/10664 11075/10436	CNC	HB-Cesic® (Gold plating)

Ref: reference, f_c: central frequency, Q_u: unloaded quality-factor; CNC: computer numerical control; T. W.: this work.

6.5 Conclusion

A lightweight, high-Q and high temperature stability spherical resonator manufactured from HB-Cesic® composite has been reported. To the best of authors' knowledge, this is the first SiC-ceramic-based microwave resonator reported in the open literature. The material properties and end-to-end manufacturing approach are introduced. Detailed experimental characterization and verification have been performed. The causes for the frequency discrepancy and spurious spikes have been analysed. The former is mainly caused by spherical radius variation whereas the latter is due to the discontinuity introduced by the assembly errors and the glue line. It is expected these spurious modes can be mitigated by optimising the manufacture process, increasing assemble accuracy and choosing appropriate bonding plane. The advantage of the HB-Cesic® resonators in Q_u and weight reduction have been demonstrated. Both resonators achieved the Q_u of over 10000 and 60% mass reduction, while achieving comparable thermal stability to Invar resonator. This work confirms the feasibility of using HB-Cesic® in microwave resonators and provide a new technology for highly thermal-stable microwave devices, paving the way for further development and verification programme for more complex passive microwave devices such as filters and multiplexers for space applications.

Reference

[1] Y. Vasavada, R. Gopal, C. Ravishankar, G. Zakaria, and N. BenAmmar, "Architectures for next generation high throughput satellite systems," *Int. J. Satell. Commun. Netw.*, vol. 34, no. 4, pp. 523–546, 2016.

[2] P. Martin-Iglesias, M. Van Der Vorst, J. Gumpinger, and T. Ghidini, "ESA's recent developments in

the field of 3D-printed RF/microwave hardware," *2017 11th Eur. Conf. Antennas Propagation, EUCAP 2017*, pp. 553–557, 2017.
[3] F. De Paolis and C. Ernst, "Challenges in the design of next generation ka-band OMUX for space applications," *31st AIAA Int. Commun. Satell. Syst. Conf. ICSSC 2013*, no. October 2013, pp. 1–7, 2013.
[4] R. J. Cameron, C. M. Kudsia, and R. R. Mansour, *Microwave Filters for Communication Systems*. Hoboken, NJ, USA: John Wiley & Sons, Inc., 2018.
[5] P. Booth and E. V. Lluch, "Enhancing the Performance of Waveguide Filters Using Additive Manufacturing," *Proc. IEEE*, vol. 105, no. 4, pp. 613–619, 2016.
[6] F. Zhang *et al.*, "3-D Printed Slotted Spherical Resonator Bandpass Filters with Spurious Suppression," *IEEE Access*, vol. 7, pp. 128026–128034, 2019.
[7] C. Guo, X. Shang, M. J. Lancaster, and J. Xu, "A 3-D Printed Lightweight X-Band Waveguide Filter Based on Spherical Resonators," *IEEE Microw. Wirel. Components Lett.*, vol. 25, no. 7, pp. 442–444, 2015.
[8] C. Guo *et al.*, "Shaping and Slotting High-Q Spherical Resonators for Suppression of Higher Order Modes," *IEEE MTT-S Int. Microw. Symp. Dig.*, vol. 2019-June, pp. 1205–1208, 2019.
[9] F. Zhang *et al.*, "A 3-D Printed Bandpass Filter Using TM-Mode Slotted Spherical Resonators with Enhanced Spurious Suppression," *IEEE Access*, vol. 8, pp. 213215–213223, 2020.
[10] E. Lopez-Oliver *et al.*, "Very High Q-Factor Bandpass Filter Using Additive Manufacturing," in *2021 IEEE MTT-S International Microwave Filter Workshop (IMFW)*, 2021, pp. 243–245.
[11] E. Lopez-Oliver and C. Tomassoni, "Stereolithography Additive Manufacturing of Overmoded Spherical Filters," *Mediterr. Microw. Symp.*, vol. 2022-May, pp. 1–4, 2022.
[12] B. Yassini and M. Yu, "Ka-Band Dual-Mode Super Q Filters and Multiplexers," *IEEE Trans. Microw. Theory Tech.*, vol. 63, no. 10, pp. 3391–3397, Oct. 2015.
[13] B. L. Steven, "Temperature compensated microwave filter," US5867077A, 1999.
[14] F. William, M. Yu, D. Smith, and A. Sivadas, "Microwave resonator having an external temperature compensator," US6535087B1, 2003.
[15] C. Qiu, N. J. E. Adkins, and M. M. Attallah, "Selective laser melting of Invar 36: Microstructure and properties," *Acta Mater.*, vol. 103, pp. 382–395, 2016.
[16] X. Wen *et al.*, "An Invar Alloy SLM Printed Diplexer with High Thermal Stability," *IEEE Trans. Circuits Syst. II Express Briefs*, vol. PP, no. c, pp. 1–1, 2021.
[17] L. Qian *et al.*, "A Narrowband 3-D Printed Invar Spherical Dual-Mode Filter With High Thermal Stability for OMUXs," *IEEE Trans. Microw. Theory Tech.*, vol. 70, no. 4, pp. 2165–2173, Apr. 2022.
[18] L. Qian *et al.*, "Thermal Stability Analysis of 3D Printed Resonators Using Novel Materials," in *2021 51st European Microwave Conference (EuMC)*, 2022, no. April, pp. 334–337.
[19] S. Liberatoscioli, M. Mattes, M. Guglielmi, D. Schmitt, and C. Ernst, "Innovative manufacturing technology for RF Passive devices combining electroforming and CFRP application," in *2008 IEEE MTT-S International Microwave Symposium Digest*, 2008, pp. 743–746.
[20] C. M. Kudsia and M. V. O'Donovan, "A Light Weight Graphite Fiber Epoxy Composite (GFEC) Waveguide Multiplexer for Satellite Application," in *4th European Microwave Conference, 1974*, 1974, pp. 585–589.
[21] C. Kudsia, T. Stajcer, and M. Yu, "Evolution of Microwave Technologies for Communications Satellite Systems," in *34th AIAA International Communications Satellite Systems Conference*, 2016.
[22] C. R. Eddy and D. K. Gaskill, "Silicon Carbide as a Platform for Power Electronics," *Science (80-.).*, vol. 324, no. 5933, pp. 1398–1400, Jun. 2009.
[23] D. M. Lukin *et al.*, "4H-silicon-carbide-on-insulator for integrated quantum and nonlinear photonics," *Nat. Photonics*, vol. 14, no. 5, pp. 330–334, May 2020.
[24] F. Reis *et al.*, "Bismuthene on a SiC substrate: A candidate for a high-temperature quantum spin Hall

material," *Science (80-.).*, vol. 357, no. 6348, pp. 287–290, Jul. 2017.
[25] "HB-Cesic Data Sheet." [Online]. Available: https://www.cesic.de/galerie.
[26] P. Noschese, M. Herbellau, A. T. Fossdal, R. Harper, and others, "X/Ka High Temperature High Gain Antenna for the Mission Bepi Colombo to the Planet Mercury," in *The European Conference on Antennas and Propagation: EuCAP 2006*, 2006, vol. 626, p. 685.

CHAPTER 7: COMPACT MONOLITHIC 3D-PRINTED WIDEBAND FILTERS USING POLE-GENERATING RESONANT IRISES

Lu Qian, Rafael Martinez, Milan Salek, Talal Skaik, Moataz Attallah, Yi Wang

Yi Wang suggested this work, planned, and supervised the entire study, and led the project. Lu Qian conceived the idea of this design and carried out the theoretical modelling, analysis and simulations, and performed the experiment, interpreted the data and wrote the manuscript. Rafael Martinez and Moataz Attallah assisted in the fabrication of the experimental samples. All authors contributed to the writing of the paper and reviewed the manuscript.

This chapter is based on the following publication: Compact Monolithic 3D-Printed Wideband Filters Using Pole-Generating Resonant Irises, which has been published in IEEE Journal of Microwave, vol. PP, no. April, pp. 1–12, 2023. Doi: 10.1109/JMW.2023.3271433

Abstract

The design concept of a pole-generating resonant iris is demonstrated in rectangular waveguide filters in this chapter. Different from conventional reactive iris, the resonant iris can generate an extra transmission pole without increasing the number of resonant cavities. As a result, several design advantages can be gained: (i) a more compact filter structure; (ii) an ability to realize strong coupling and therefore wide bandwidth; and (iii) a new polarization rotation capability. Two third-order Chebyshev filters are designed and implemented, demonstrating the miniaturization and polarization rotation feature. A fifth-order Chebyshev filter with 20% fractional bandwidth is presented to show the capability of realizing wideband. This also demonstrates the realization of asymmetric coupling between the resonant iris and the cavity resonator on either side. An approach to control and extract the coupling between the iris and the cavity resonator has also been presented. To manufacture the intricate asymmetric iris structure, all the presented filters are printed monolithically using selective laser melting technique. Excellent agreement between the measurements and simulations has been achieved, verifying the design concept as well as the additive manufacturing capability in microwave waveguide devices.

Keywords: Additive Manufacturing (AM), evanescent mode, J-inverter, K-inverter, resonant iris, selective laser melting (SLM), waveguide filters, waveguide twists, wideband filter.

7.1 Introduction

Waveguide cavity filters have been widely used in satellite and base station applications because of their excellent performance in terms of low loss and high-power handling capacity. The rapid development of wideband communication and carrier aggregation has spurred the growing research activity in wideband waveguide filters [1], [2]. Typical filter requirements for 5G sub-6 GHz system are wideband (around 10%), compact in size, and low profile. In satellite communication transponders, wideband filters are often an indispensable part of the transmit–receive diplexers.

For waveguide filters, there are two typical approaches to realize wideband filtering performance. The first one requires cascading several coupled single-mode resonators [3]–[6]. However, the increasing size and mass is a well-known concern as the order of waveguide filter rises. Wider bandwidth usually needs stronger coupling. The irises that enable strong coupling strength are often associated with the degradation of out-of-band performance due to the higher-order modes and iris resonances. To address this drawback, one method is to push the iris resonance to higher frequency by dividing the single iris to multiple smaller apertures [7], but the coupling strength will decrease. Another approach to realizing wideband filter is to use multi-mode resonators [1], [8], [9], where multiple resonance modes were excited in a single resonator. The overall filter size can hence be reduced while the filter bandwidth can be increased. However, it is often difficult to implement the high-order filters because of the complicated coupling scheme. Filters with multi-mode resonators are also more sensitive to manufacturing tolerances and often suffer from poor temperature stability [10]. In practical filter applications, waveguide filters with explicit coupling schemes and in-line configurations are still highly desirable.

Waveguide cavity filters usually use coupling irises (thin metallic diaphragms containing a concentric opening) to realize the coupling between cavities. From the circuit point of view, the irises can be normally represented as coupling capacitor or inductor. In the past decades, researchers have modified the coupling irises for new or enhanced functionalities in filters. In [11]–[13], capacitive and inductive irises were combined to implement a resonator to replace the waveguide cavity resonators, but the coupling between resonators relies on additional quarter wavelength waveguide inverters, which increases the size of the filter. In [14]–[17], the frequency-dependent coupling irises were used to generate transmission zeros (TZs). More recently, iris structures have been used to realize multiple passbands or enhance the bandwidth of waveguide filters [18], [19]. However, it should be noted that all above function-enhancing irises rely on complex iris structures. Therefore, a capable and reliable fabrication solution will be the critical enabler to exploit the potential of the resonant iris and new iris structures.

These novel irises structures are traditionally manufactured in separate piece-parts by computer numerical control (CNC) machine and then bolted together [11]–[13], [17]. They could also be integrated into the filter, and the entire filter is machined out of multiple parts [15], [16], [19]. However, assembly error is an important source of performance degradation. The passive intermodulation (PIM) product generated at mechanical interconnections could reduce the power handling capacity. Moreover, the low manufacture freedom of conventional subtractive process severely limits the design flexibility of iris structures. Most previous work only look at rectangular resonant irises or non-centered resonant apertures.

In recent years, additive manufacture (AM) technology (known also as 3-D printing) becomes an increasingly popular method to construct microwave devices, because of its high freedom of rapid prototyping and the unique capability of forming complex geometric structures [20]–[24]. For instance, microwave filters based on non-conventional geometries have been designed and manufactured [25]–[27]. Monolithic waveguide subsystems that integrate several RF functionalities were reported [28]–[30]. Work to explore the printing of novel materials such as Invar can also been found in [31], [32].

We have recently proposed a 3-D printed waveguide filter using pole-generating resonant iris structure in [33]. By replacing the conventional reactive irises with resonant irises, an extra transmission pole (TP) can

be implemented within the space previously occupied by the coupling iris. This allows a higher-order filter without excessive size increase. Selective laser melting (SLM) technique was employed to manufacture the unconventional resonant iris structures. Here we have extended the work in [33] in several areas: (1) Asymmetric coupling resonant iris was implemented, only enabled by the manufacturing capability of 3D printing. A new geometrical freedom was introduced to realize the asymmetric coupling on either side of the resonant iris, which is often impractical for traditional machining methods due to the limited lateral space within the iris. (2) Circuit analysis of the pole-generating resonant iris structure was presented. The frequency dependance of the iris coupling and the iris resonance feature were discussed. An intuitive design procedure was introduced. (3) The wideband capability was explored. A filter with 20% fractional bandwidth is demonstrated. (4) The polarization rotation capability, enabled by the symmetry in the resonant iris structure, was demonstrated. This allows a 90° twist to be easily embedded into the filter. Compared with traditional waveguide twists [34]–[36], this design feature eases the fabrication and provides a compact configuration. (5) The reproducibility of the SLM manufacture solution was investigated. Several designed filters were reproduced and measured. Measurement results show a good correlation with the tolerance analysis. This work also gives an assessment to the surface finish, by providing surface roughness measurements and showing the impact on insertion losses.

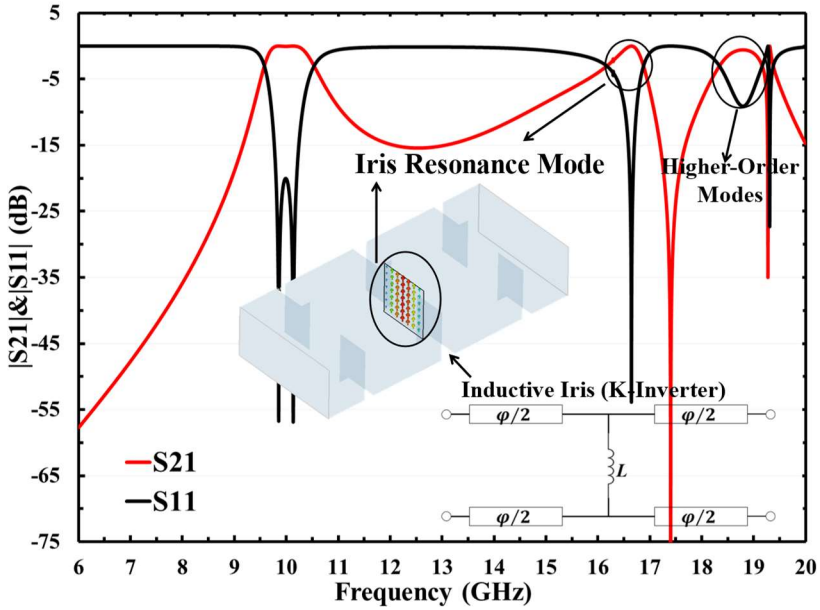

Figure 7.1 Frequency response of a two-pole coupled cavity filter using inductive irises, with inset showing the E-field pattern at the iris projected on the middle cross-section.

7.2 Pole-generating Resonant Iris

7.2.1 A Concept of pole-generating Resonant Iris

The initial idea of this design concept comes from a common phenomenon. The inductive coupling irises often accompany by a spurious resonance above the passband, deteriorating the out-of-band rejection, especially for wideband filters. Figure. 7.1 shows the frequency response of a waveguide filter with inductive irises and the TE_{101}-like electric field pattern of the iris when it resonates. In this work, we try to leverage the iris resonance and propose the pole-generating resonant iris structure. Figure. 7.2(a) shows the initial L-shaped resonant iris proposed in [33]. To form the resonant iris, an extra metallic diaphragm was added next to the

symmetric inductive iris. Since the diaphragm introduces discontinuity into both the H-plane and E-plane, an L-shaped resonant aperture is realized. For comparison, the classic rectangular resonant iris is also presented in Figure. 7.2(b). From the simulated electric field (E-field) distributions, it is clear that both field patterns are like the TE_{101} mode, but the pattern of the L-shaped aperture is folded. Hence, the L-shaped resonant iris has a longer electrical length than the classic rectangular resonant iris. The iris resonance mode can be readily lowered into the passband, while the condensed E-field also enables the stronger coupling. Nevertheless, the above L-shaped iris can only realize basic pole-generating feature. To implement higher-order filters, a design methodology is needed. Therefore, the circuit analysis and electromagnetic optimization will be discussed next.

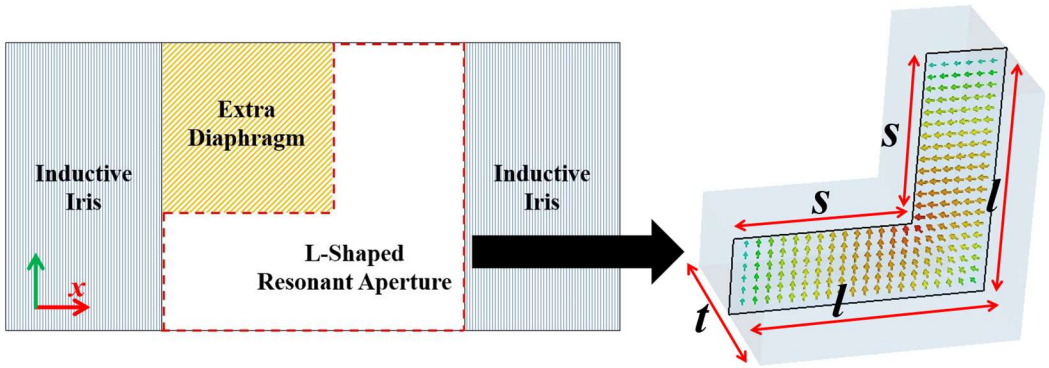

(a)

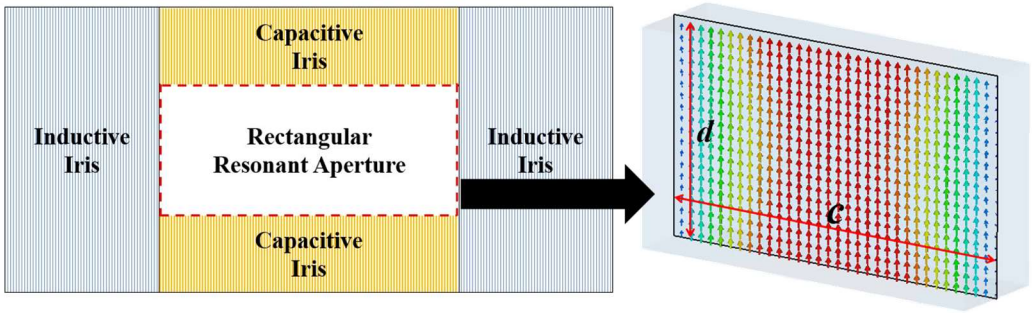

(b)

Figure 7.2 (a) L-shaped resonant iris. (b) Rectangular resonant iris. Front view of the structure (the left). E-field pattern of its resonance mode projected on the E-plane (the right).

7.2.2 Circuit Model and Analysis

The circuit model will be first illustrated to help understand the operation mechanism of the resonant iris. This circuit analysis will focus on the pole-generating feature. The inductive iris in Fig. 1 works as an impedance inverter (K-inverter) between two resonators and usually is represented as a shunt inductor as shown in the inset. However, the iris is a distributed physical structure. Its intrinsic frequency dependence will lead to unintended transmission feature. Herein, its embodiment is the extra transmission pole (TP) generated by the iris resonance mode on the upper stopband. To investigate the pole- generating feature, a resonant equivalent circuit was used, as presented in Figure. 7.3. The shunt inductor in the classical K-inverter is replaced by a parallel LC circuit, and its resonance frequency is determined by

$$\omega_P = 1/\sqrt{L_P C_P} \tag{7.1}$$

We will consider the following two cases:

1) CASE I: ($\omega_p \neq \omega_0$ where ω_0 is the center frequency of the filter)

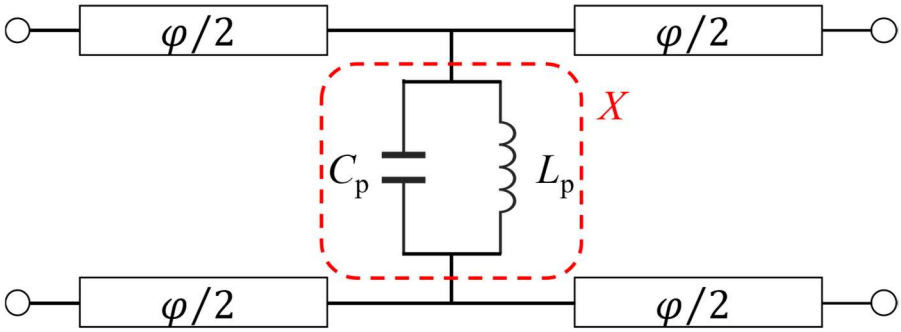

Figure 7.3 Equivalent circuit for the resonant iris.

In this case, the resonant iris amounts to a frequency-variant coupling element, which can offer the required coupling at the centre frequency while generate an extra transmission pole on the upper stopband. Considering the circuit in Figure. 7.3, the parallel LC can be regarded as a shunt reactance, X at ω_0, and the two-port network acts as a K-inverter. Two conditions can be imposed: 1) The parallel LC circuit resonates at ω_p ($\omega_p > \omega_0$); 2) At ω_0, the transmission matrix of the iris must be the same as that of the K-inverter. i.e.

$$\begin{bmatrix} A & B \\ C & D \end{bmatrix} = \begin{bmatrix} 0 & -jK \\ 1/jK & 0 \end{bmatrix} \tag{7.2}$$

The elements of this matrix can be respectively calculated [37]:

$$A = D = cos\varphi + \frac{Z_0}{2X} sin\varphi$$
$$B = jZ_0 sin\varphi + j\frac{Z_0^2}{X} sin^2(\frac{\varphi}{2})$$
$$C = \frac{j}{Z_0} sin\varphi + \frac{cos^2(\frac{\varphi}{2})}{jX} \tag{7.3}$$

where Z_0 is the characteristic impedance and X is the equivalent reactance of the parallel LC circuit at ω_0.

$$X = \frac{\omega_0 L_P}{1 - \omega_0^2 L_P C_P} \tag{7.4}$$

Combining (6.1) - (6.4), we can find

$$K = Z_0 tan|\frac{\varphi}{2}|, \varphi = -\arctan\frac{2X}{Z_0}$$
$$|X| = \frac{K}{1-\left(\frac{K}{Z_0}\right)^2}, X = \frac{\omega_p^2 \omega_0 L_P}{\omega_p^2 - \omega_0^2} \tag{7.5}$$

Therefore, for waveguide iris filters, once the passband specification is specified, we can predict the position of the transmission pole from the iris resonance, which can also provide insight for the achievable bandwidth of the designed waveguide filter. The corresponding shunt capacitor and inductor values can be further calculated using the following equation.

$$C_P = \frac{\omega_0(1-(K/Z_0)^2)}{K(\omega_P^2-\omega_0^2)}, X = \frac{\omega_p^2\omega_0 L_P}{\omega_p^2-\omega_0^2} \tag{7.6}$$

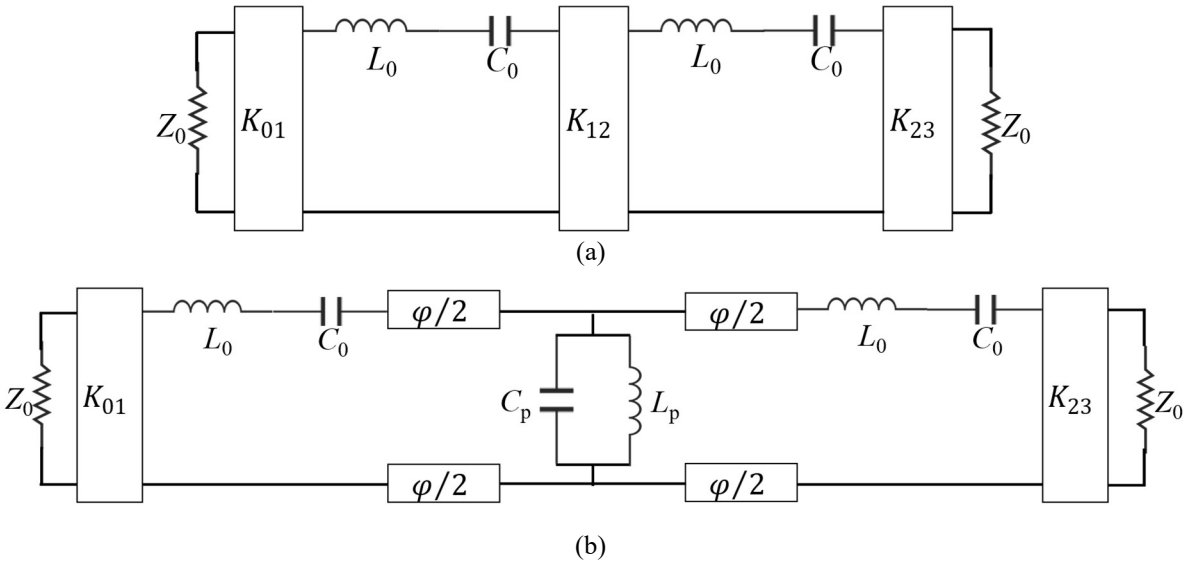

Figure 7.4 Equivalent circuit model for the two-pole Chebyshev filter, based on (a) the ideal *K*-inverter and (b) the resonant iris.

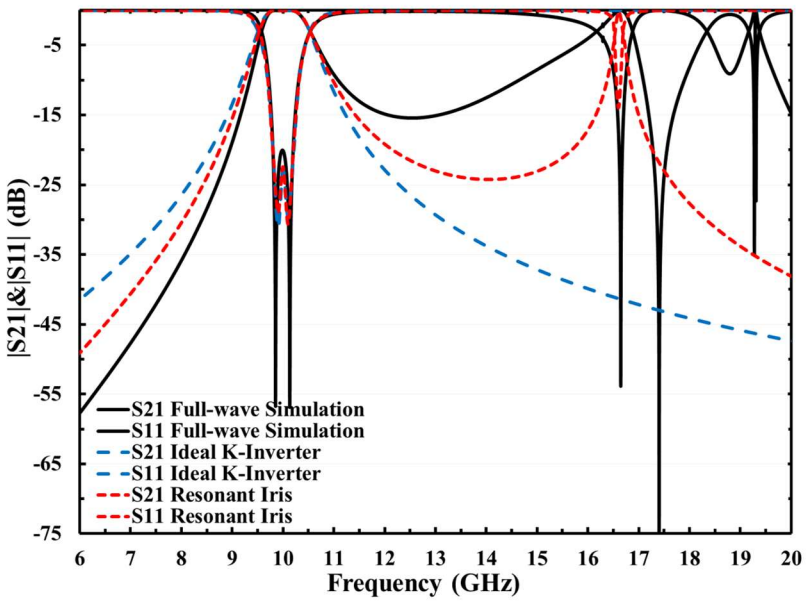

Figure 7.5 Comparison of filter performance of full-wave EM simulation, circuit simulation based on ideal *K*-inverter and resonant iris.

To verify the circuit model, we consider the two-pole Chebyshev waveguide iris filter in Figure. 7.1. Its centre frequency and bandwidth with 20 dB return loss is 10 GHz and 400 MHz, respectively. Figure. 7.4 presents two schematic circuits for this filter, respectively based on the ideal *K*-inverter and the resonant inverter model, where $\omega_0 = 1/\sqrt{L_0C_0}$. The circuit elements can be calculated to be: C_0 = 0.151 pF, L_0 = 1.671 nH, $K_{01} = K_{23}$ = 18.748, K_{12} = 7.548, φ = 16.71°, L_p = 0.071 nH, and C_p = 1.601 pF. A comparison of

their responses (simulated using AWR Design Environment) and the full-wave EM model response (from CST Microwave Studio) is shown in Figure. 7.5. It is apparent that the equivalent circuit with the resonant iris better represents the full-wave EM model in terms of the in-band response as well as the position of the transmission pole at 16.6 GHz.

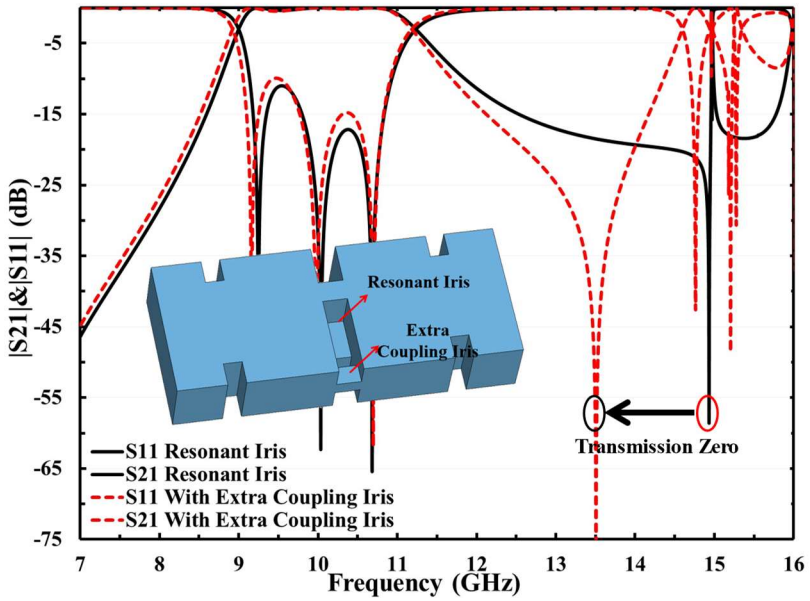

Figure 7.6 Comparison of simulated third-order resonant iris filter responses between filters with and without extra coupling iris.

2) CASE II: ($\omega_p = \omega_0$)

In this case, the resonant iris can be regarded as a singlet which produce a pole-zero pair in the frequency response. As demonstrated in [33], when the L-shaped resonant iris is sandwiched between two waveguide TE_{101} resonators, the TP generated by the resonance iris can be moved into the passband, as shown in Figure. 7.6 (the black solid curves) from a three-pole filter with one resonant iris. The transmission zero appears at 15 GHz. If an extra coupling aperture (See the inset of Figure. 7.6) is added next to the L-shaped iris, the TZ can be further controlled as shown in Figure. 7.6 (the red dash curves). Three TPs are generated within the passband, while the TZ can be manipulated using the extra coupling iris. Therefore, the equivalent circuit in Figure. 7.3 is no longer applicable for the filter in this case.

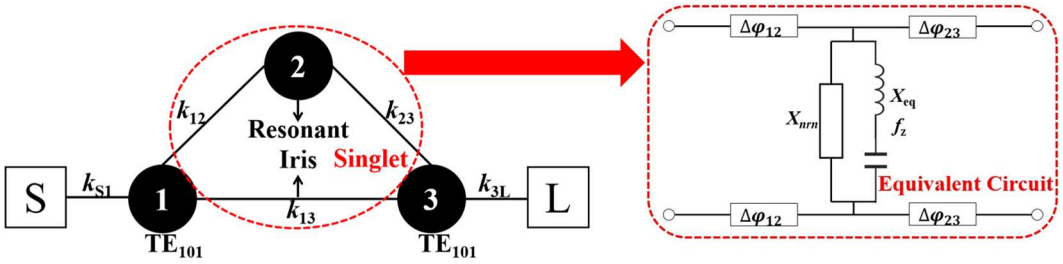

Figure 7.7 Coupling topology of the filter in Figure. 7.6 and the equivalent circuit of the singlet. X_{eq} and f_z are the equivalent slope parameter and the resonating frequency, respectively, of the series resonators determining the transmission zero; X_{nrn} is frequency-invariant reactance; and all $\Delta\varphi$ are the parameters of ideal phase shifters.

Considering its coupling topology (see Figure. 7.7), we can find the resonant iris not only provides the additional resonance node, but also allows the cross coupling k_{13}. The core pole-zero block (marked out by the red circle) is equivalent to a singlet. From the circuit perspective, the singlet can be more explicitly represented by the alternative equivalent circuit, as illustrated in Figure. 7.7 [38]. The shunt branch (series LC circuit) is added to account for the extra transmission zero. The synthesis-based approach to design filters with cascaded singlets has been well established [38], [39]. However, most methods are developed for narrowband filter and rely on circuit extraction process for physical implementation.

Herein, we focus on the pole-generating feature of the resonant iris and use it to enhance the wideband capability of waveguide iris filters. In addition, the extra coupling iris allows us to control the cross-coupling. Thus, a more intuitive design approach is used to link the coupling coefficient to the real geometric dimensions of the resonant iris. Figure. 7.8 shows the EM simulation model and the simulated S_{21} response used to extract the coupling coefficient. According to [40], the frequencies of two peaks of S_{21} (f_{p1} and f_{p2}) represent the magnetic and electric frequency f_m and f_e. The corresponding coupling coefficient k can be calculated by

$$k = \pm \frac{f_{p1}^2 - f_{P2}^2}{f_{p1}^2 + f_{P2}^2} \tag{7.7}$$

where the plus-minus sign represents the different nature of the coupling, whether magnetic or electric. This can be further determined from the phase information of S_{21}. In each iteration of the simulation, both resonances should be adjusted to keep the average of the two peaks ($f_{p1} + f_{p2}$) / 2 at the specified centre frequency. In the simulation model, two SMA connectors are inserted into the resonators to provide the weak coupling. The open end of the resonant iris is approximated by a perfect magnetic wall to account for the loading effect from the adjacent resonator. It should be noted the model in Figure. 7.8 is simplified to illustrate the extraction process. More detail on the design of the resonant iris will be discussed in the next section.

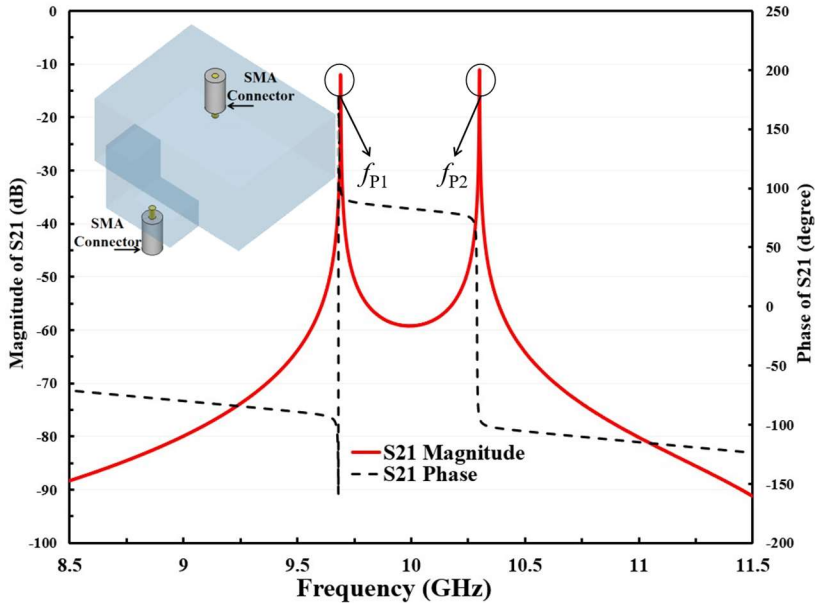

Figure 7.8 EM model used to extract coupling coefficient and the typical simulated transmission coefficient S21.

7.2.3 Optimization of the L-Shaped Resonant Iris

It is often desired that the frequency and the coupling in a resonator can be adjusted seperately. However, for the primitive L-shpaed resonant iris (see Figure. 7.2(a)) proposed in [33], only two design parameters (*t*

and s) can be used. The parameter l is largely fixed to fit the connected waveguide resonators. The degree of freedom in the design is very limited. New degree of freedom is needed for the resonant iris structure. Observing the simulated E-field distribution in Figure. 7.2, the E-field concentrates in the central area of the resonant structure and decays along to both sides. Therefore, the resonance frequency of the resonant iris is more sensitive to the dimensional changes of the structure in the central area. If we mitre the two end edges of the resonant iris, a taper transformation along the Z-axis can be formed, as shown in Figure. 7.9. As a result, an additional degree of freedom to control the frequency can be realized. This also facilitates the tuning of inter-resonator coupling with the adjacent resonators and the realization of asymmetric coupling. Figure. 7.9(b) shows the tapered resonant iris with asymmetric coupling, where the two end sides have different cross-sections. It should be noted that such intricate structures would present significant difficulty with conventional machining. In contrast, they can be easily formed by 3-D printing.

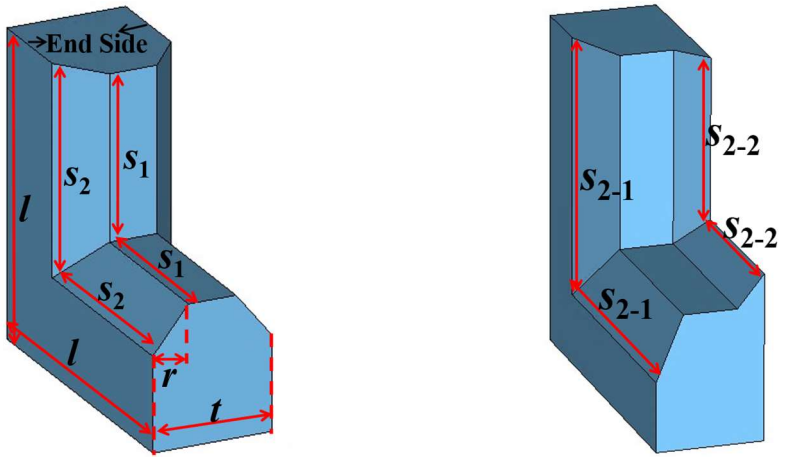

(a) (b)

Figure 7.9 Modified resonant iris structure and key dimension parameters. (a) Resonant iris with symmetric couplings. (b) Resonant iris with asymmetric couplings.

Figure. 7.10 illustrates a few crucial dimensions of the modified resonant iris. The dimensions s_1 and s_2 are used to separately control the size of the middle and end cross-sections whereas the parameter r is used to control the angle of the mitred edges. It is important to note that the two mitered end sides can be different from each other to allow for asymmetric coupling. An example will be demonstrated later. Parametric studies were carried out to understand the behavior of the resonant iris. Both end sides are set as a perfect magnetic wall to imitate the loading effect, to some extent, from cascaded resonators. The parameter l is fixed to 10.16 mm to be compatible with the X-band waveguide. Figure. 7.10(a) shows the variation of the resonance frequency of the resonant iris versus s_1 or s_2, where the inset shows the air models of resonant iris at three representative cases. When s_1 equals to s_2, the modified resonant iris degenerates into the initial version. It is apparent that the resonance frequency is more sensitive to s_1, especially when s_2 is smaller than s_1. Further control can be applied by changing the parameter r. Shown in Figure. 7.10(b) is the variation of the resonance frequency versus s_2 under different ratio of r/t. As the ratio decreases, the frequency curve exhibits less variation, which means the ratio of r/t can mitigate the influence of s_2 on the resonance frequency.

In addition, Figure. 7.11 shows the simulated resonance frequency and the unloaded quality factor Q_u versus the thickness of the resonant iris t. As can be observed, while the frequency change is almost negligible, the Q_u can be considerably improved with the increased thickness t. Still the Q_u of the resonant iris is smaller than the standard X-band rectangular waveguide resonator at 10 GHz (usually on the order of 8000) due to the condensed E-field. The electrical conductivity of silver (6.3×10^7 S/m) was assumed for the extraction of the Q_u.

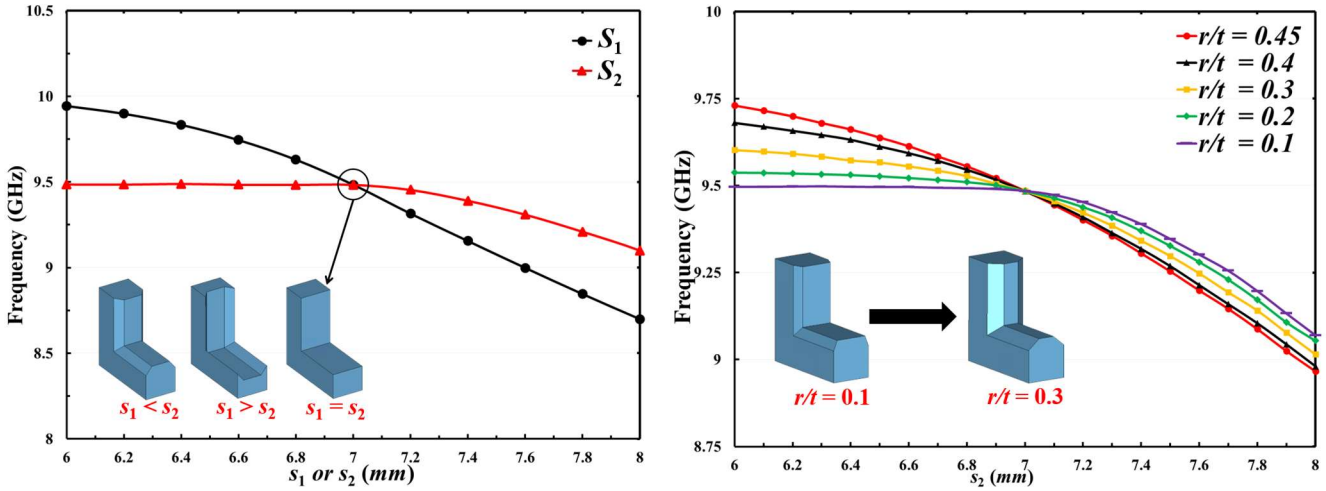

Figure 7.10 Parametric study of the resonant iris. (a) Frequency variation versus s_1 or s_2, where one parameter is kept constant (7 mm) while the other is varied. (b) Frequency variation versus s_2 under different r/t.

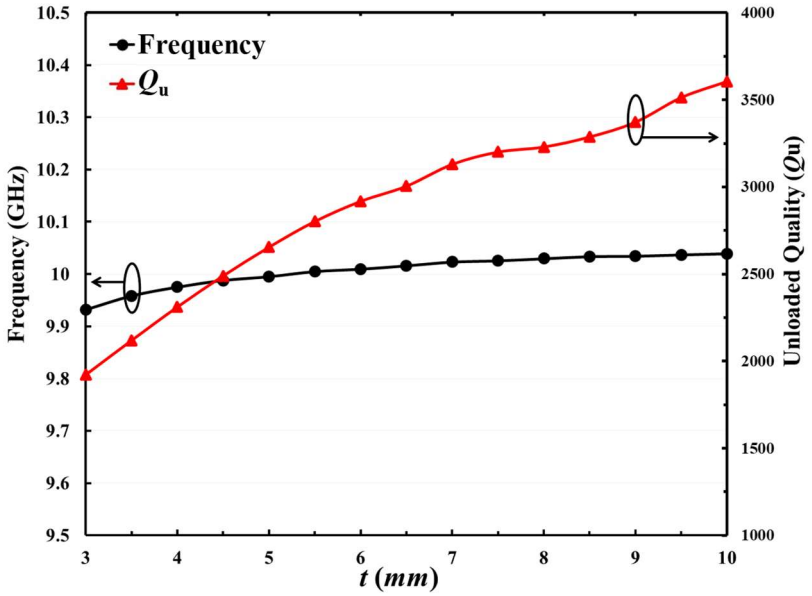

Figure 7.11 Simulated resonance frequency and Q_u versus the thickness of the resonant iris t.

Next, we consider the control of the coupling associated with the resonant iris, using the parameters s_2 and t. Figure. 7.12 shows the coupling coefficient curves, extracted using the method shown in Figure. 7.8. The coupling increases with the rising s_2 and decreases with t, while both parameters have comparable effect on the coupling strength. Therefore, the effective control of the coupling can be achieved by adjusting the two parameters. Estimated from the achievable coupling strength, if we consider a common 4th-order Chebyshev filter, the achievable fractional bandwidth can readily reach at least 20%. Moreover, because of the field distribution of the L-shaped folded TE$_{101}$ mode is rotationally symmetric (see Figure. 7.2(a)), an additional polarization rotation feature can be realized. A filter with the rotation feature will be demonstrated later. It is

worth noting that the resonant iris concept could work with other waveguide resonators than the rectangular cavity resonators used here.

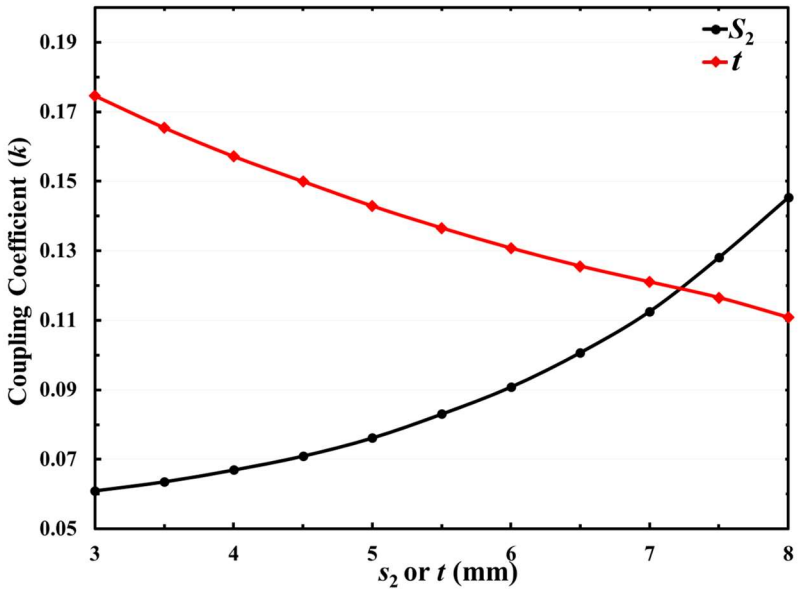

Figure 7.12 Simulated coupling coefficient versus the parameters s_2 and t.

Now that both the resonance frequency and coupling associated with the resonant iris are shown to be adjustable, the design procedure of the filter using resonant irises can be summarized as follows: 1) change the parameter s_1 to obtain the specified resonant frequency. In this step, s_2 equals to s_1; 2) adjust parameters s_2 and t to obtain the required coupling while fine-tuning s_1 and r to modify the resonance frequency; 3) construct the initial filter using the obtained dimensional parameters and then perform full-wave optimization.

7.3 Design Examples

In this section, three filter prototypes are designed as demonstrators.

7.3.1 Two Third-order Chebyshev Filters

Figure. 7.13 illustrates two third-order waveguide filters based on the pole-generating resonant iris, where an L-shaped resonant iris is sandwiched between two conventional TE_{101} resonators. To aid visualization, the metallic wall of the filters is rendered with translucent yellow color. The first filter in Figure. 7.13(a) is with a traditional in-line configuration, whereas the filter in Figure. 7.13(b) is similar but with a polarization rotation feature where only the first resonator is rotated by 90°. All other dimensions are kept the same.

The first filter is specified with a centre frequency of 9 GHz, a fractional bandwidth of 9.5% and in-band return loss of 20 dB. The detailed discussion about this filter has been reported in [33]. Compared to the common rectangular waveguide filters, this filter has a footprint reduction of 20% while showing an improvement on the out-of-band rejection. The second example in Figure. 7.13(b) is to demonstrate the polarization rotation feature of the resonant iris. The same design specification as the first example is adopted. Figure. 7.14 compares the response before and after polarization rotation. Little effect on the performance is shown, due to the rotation symmetry of the resonant iris.

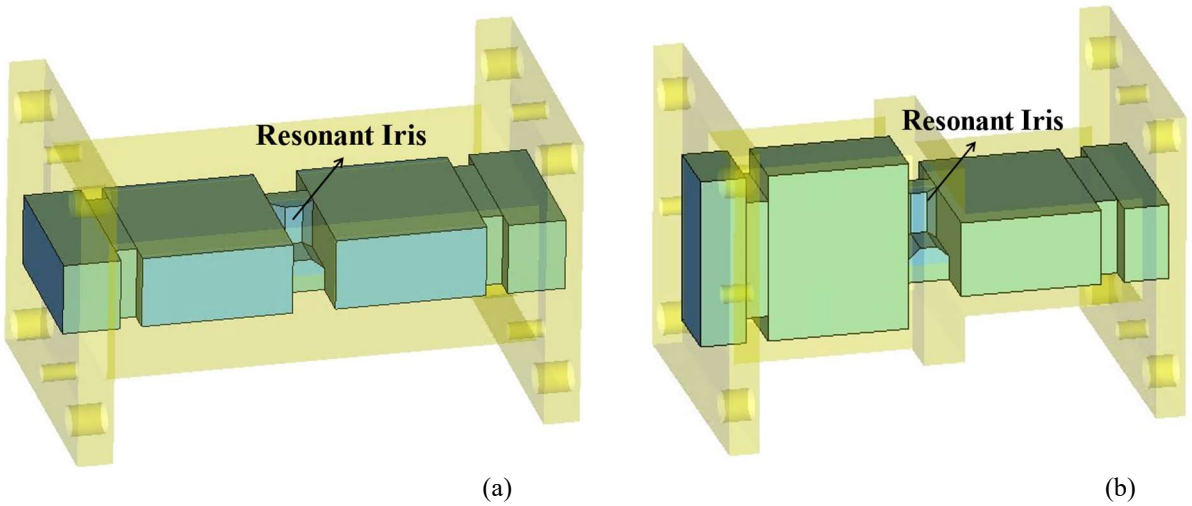

Figure 7.13 Internal structures of the third-order waveguide filters based on the pole-generating resonant iris. (a) In-line configuration. (b) In-line configuration with polarization rotation.

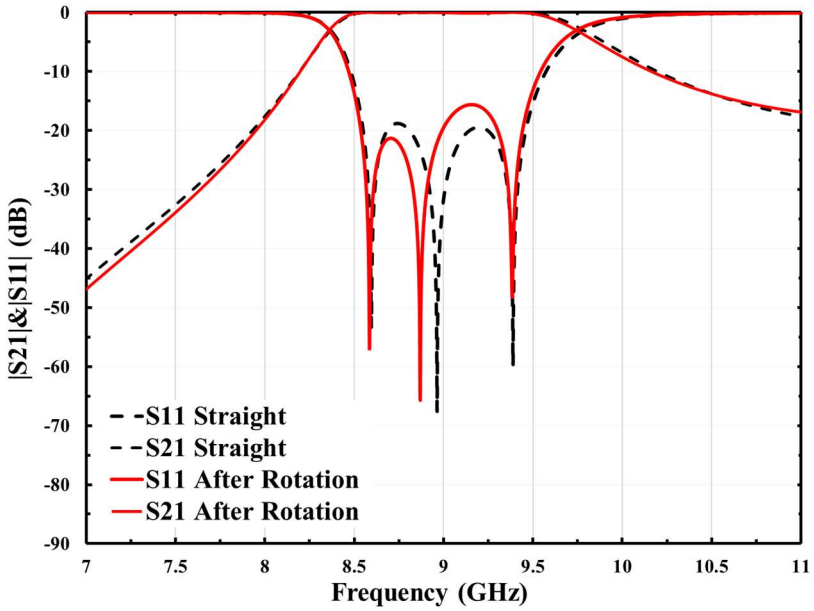

Figure 7.14 Simulation response of the third-order resonant iris filter with and without polarization rotation.

7.3.2 A Fifth-Order Chebyshev Filter

The third example is to demonstrate the wideband capability and the implementation of asymmetric coupling using the resonant iris. It is designed to operate at 10 GHz with the equal-ripple passband fractional bandwidth of 20% and a return loss of 20 dB. The design parameters can be calculated to be $k_{S1} = k_{5L} = 1.01$, $k_{12} = k_{45} = 0.86$, and $k_{23} = k_{34} = 0.63$. Figure. 7.15(a) shows the filter structure, where a tapered resonant iris was used to realize the asymmetric coupling on either side of the iris (i.e., $k_{12} \neq k_{23}$). Note that the mitred angle of the resonant iris in this example has been adjusted to provide a smoother transition between the two end faces. A comparison between the simulated and the ideal response calculated from coupling matrix is presented in Figure. 7.15(b). The response of the initial design from physical dimensioning (or coupling

extraction) provided a reasonably good starting point for the following full-wave optimization. The filter response after optimization agrees well with the ideal response.

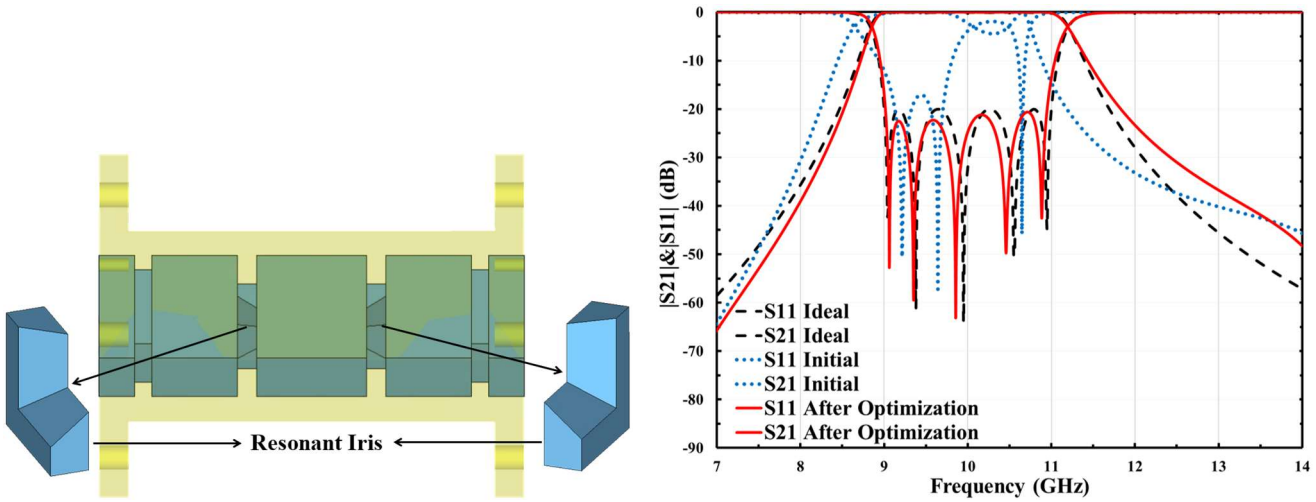

Figure 7.15 (a) Internal structure of a fifth-order waveguide filter based on the pole-generating resonant iris. (b) Comparison of filter responses: from extracted initial dimensions, after optimization, and from the ideal response determined by the coupling matrix.

Figure. 7.16 compares the simulated wideband responses between the resonant iris filter and the conventional fifth-order waveguide iris filter, with the inset showing their internal structure and the enlarged view of the in-band S_{21} responses. The 28% reduction in the overall length of the filter has been achieved. From Figure. 7.16(a), we can observe that the attenuation floor of the lower stopband is slightly worse than the rectangular waveguide filter. However, the upper stopband rejection is improved considerably over the waveguide iris filters as the spurious resonance mode is moved into the passband. The simulated insertion loss is 0.06 dB for the traditional and 0.15 dB for the resonant iris filter. The slightly higher loss is a result of the lower Q_u of the resonant iris. Another common concern about the low-Q resonant structure is the passband distortion, such as degraded passband flatness or rounded passband shoulder. To recover the sharp passband selectivity, common methods include predistortion [41] and the use of nonuniform Q-values [42]. Connecting the external ports with a high-Q resonator is also an effective approach [43] in the practical application. For the proposed resonant iris filters, the low-Q resonant irises are sandwiched between two higher-Q rectangular waveguide resonators. There is some intrinsic balancing effect. From the expand view of the in-band S_{21} response (see Figure. 7.16(b)), we can see the variation in insertion loss are similar, around 0.2 dB, for the resonant iris filter and the conventional one. Therefore, it is reasonable to believe the resonant iris structure has a small impact on the in-band transmission response, especially for the wideband applications.

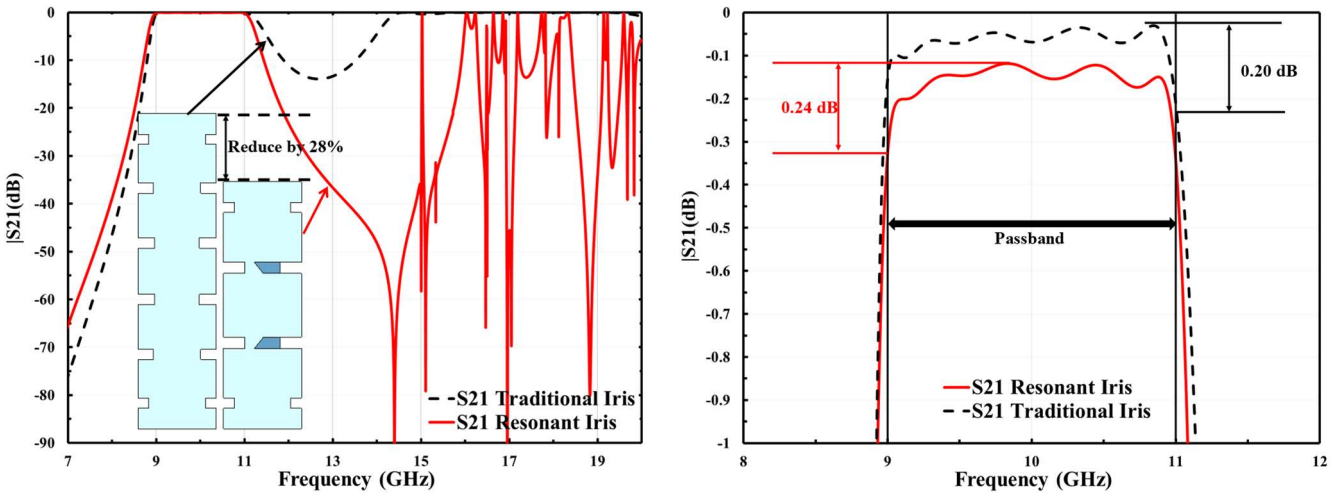

Figure 7.16 Comparison of filter response between the traditional fifth-order waveguide filter and the filter based on pole-generating resonant iris. (a) Wideband response. (b) Enlarged view of the in-band response.

7.4 Manufacture and Measurement

7.4.1 Manufacturing Process

The resonant iris structure increases the manufacture complexity for traditional milling techniques, and even makes it impractical as far as the tapered resonant iris is concerned (Figure. 7.15). With this in mind, AM technique is chosen to manufacture the intricate tapered iris structure because of its unique capability of allowing monolithic fabrication of complex microwave components. More specifically, the selective laser melting (SLM) technique was employed on the twin-laser SLM500HL system. All three prototype designs were printed monolithically using A20X. It is an aluminium-copper-based alloy powder, containing 92% aluminium, 5% copper, and 3% other materials. To examine the reproducibility of the manufacturing process, the 2nd and the 3rd design were printed twice. It should be noted they were printed in different batches to test the practical repeatability.

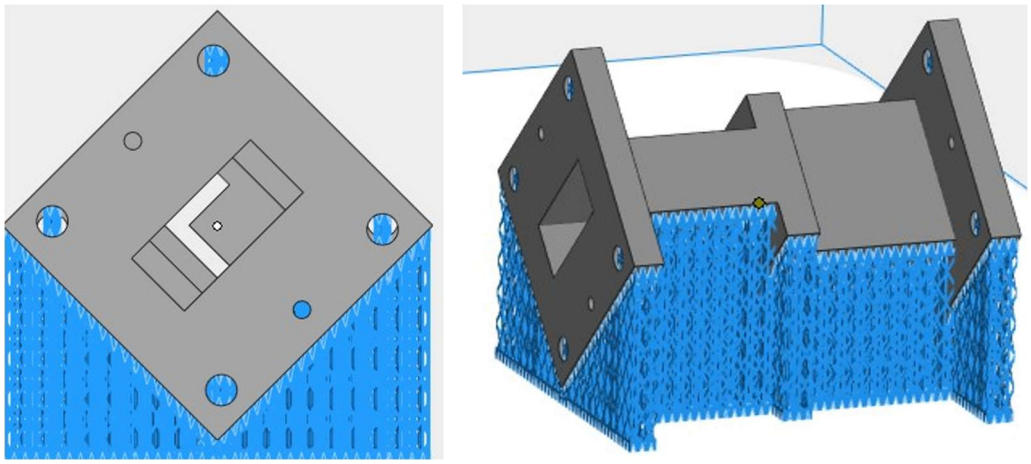

Figure 7.17 CAD model and external supporting structure (indicated in blue) used in the 3-D printing process.

Figure. 7.17 illustrates the printing direction where the blue-coloured material represents the scaffold supporting structure. In printing, all the filters are tilted 45° to avoid any overhang structures inside the filter, while the downskin surface with the worst surface finish can be moved away from the electrical current concentrating area (top surface of rectangular waveguide). Table 7.1 summarizes the laser processing parameters and layer thickness. No surface treatment was applied on these samples except for the flange interfaces. Figure. 7.18 shows the photograph of the three monolithically printed filters. The small difference between the two third-order filters is caused by the length of feeding waveguide and wall thickness.

Table 7.1 Processing Parameters of All Filters

Powder Size (μm)	Layer Thickness (μm)	Laser power/P (W)	Scan speed/V (mm/s)	Spot size/h (μm)	Energy density/*E* (J/mm^2)
15-53	30	360	1500	70-80	1.6

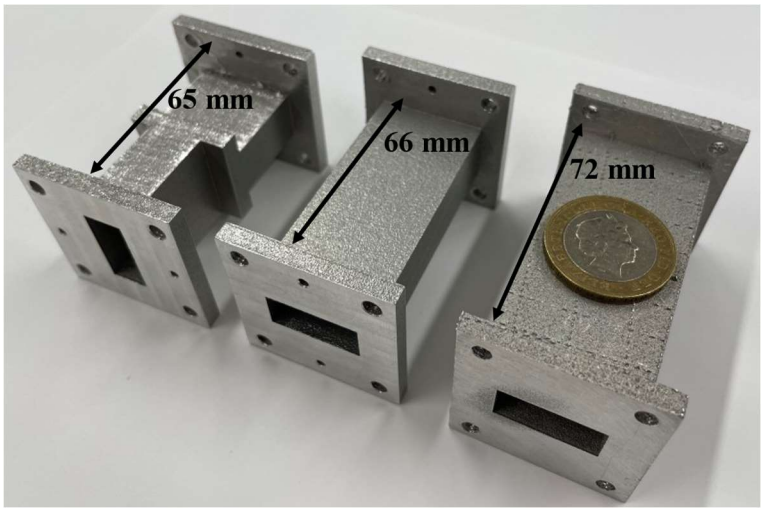

Figure 7.18 Photographs of three monolithically printed filters. From left to right, they are the third-order filter with polarization rotation, the third-order filter, and the fifth-order filter.

7.4.2 Measurement Results

S-parameter measurements of all filters were performed on Agilent E8361C PNA network analyser. The analyser was calibrated using TRL (Thru, Reflect, Line) method prior to the measurements.

For 3-D printed devices, the effective electrical conductivity is significantly affected by the surface roughness. The first third-order filter was used to evaluate the effective conductivity of A20X alloy used in 3-D printing. Its nominal electrical conductivity has been reported to be 1.9×10^7 S/m [44]. Herein, the Hammerstad-Bekkadal (HB) method [45] is used to calculate the effective conductivity:

$$\sigma_e = \sigma_0 \times (K_{SR})^{-2} \tag{7.8}$$

where σ_0 is the electrical conductivity of the conductor with a smooth surface and K_{SR} is the Hammerstad correction factor, given by

$$K_{SR} = 1 + \frac{2}{\pi} \times tan^{-1}\left(1.4 \times \left(\frac{\Delta}{\delta}\right)^2\right) \tag{7.9}$$

Here, δ is the skin depth of the conductor and Δ is the root mean square surface roughness. Δ of the printed filter in this work was measured to be 3.5 μm using Alicona InfiniteFocusSL microscope. It is larger than the skin depth (1.2 μm for the A20X alloy at 9 GHz). The effective conductivity can be calculated to be 0.56×10^7 S/m.

To verify the calculated effective conductivity, Figure. 7.19 shows a comparison between the simulated results and the measured filter response, where the inset is the expanded view of S_{21}. It can be observed the surface roughness introduces an additional insertion loss of 0.07 dB. The measured insertion loss agrees well with that predicted from the effective conductivity, so the conductivity of 0.56×10^7 S/m will be applied in the following simulations to account for the impact of the surface roughness。

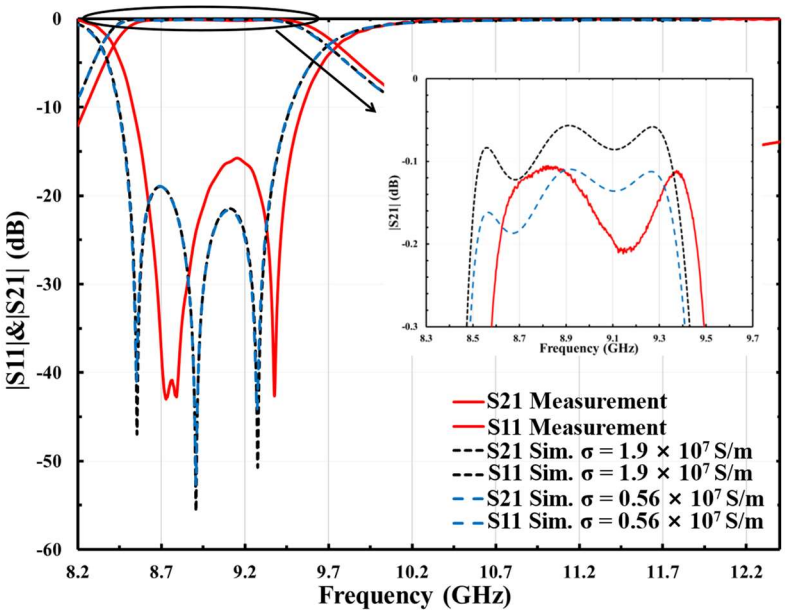

Figure 7.19 Comparison of the third-order resonant iris filter between the measured result and simulation response with different electrical conductivities.

Figure. 7.20 shows the measured and simulated results of other two designs. No tuning was applied. As can be observed, all the measured passbands agree with the simulated results very well. For the third-order filter with polarization rotation, two samples were printed and measured (see Figure. 7.20(a)). The measured centre frequency is 8.91 GHz (Sample 1), shifted down by 1.0% and 9.05 GHZ (Sample 2), shifted up by 0.6%. Within the passband, the measured minimum return losses are around 15 dB whereas the measured average insertion loss is around 0.17 dB. The simulated insertion loss is 0.16 dB. Figure. 7.20(b) illustrates the in-band and wideband performance of the fifth-order waveguide filter. An excellent agreement is achieved between the simulated and measured in-band response, especially for the second sample. The measured centre frequency is 10.05 GHz and 9.97 GHz, respectively. The average insertion loss is better than 0.18 dB for both samples, which is close to the simulated 0.15 dB. The wideband performance is also as expected, with the rejection of 20 dB up to 15.3 GHz. It should be noted that 'response calibration' is used for the wideband measurement, so the evident ripple can be observed in the transmission response. Overall, very good agreement between the theoretical and measured results has been demonstrated.

A reduced-Q resonant structure will set a lower bound on achievable minimum bandwidth. To evaluate this limit, we first extract the Q_u using coupling matrix method from the measurement responses of the two samples of the fifth-order filters. All resonators are assumed to be uniform for simplicity. The Q_u can be extracted to be 1700 (Sample 1) and 2100 (Sample 2). The average Q value of 1900 was then used to evaluate

the insertion loss for filters with different bandwidths. If we consider the 1 dB threshold of insertion loss, the achievable bandwidth can be estimated to be 140 MHz. For typical filters in satellite payload around X-band, the resonant iris filters could be used for the wideband feeding filters (e.g. with a bandwidth of 250 or 500 MHz), but may not be suitable for the narrowband channel filters (e.g. with a bandwidth of 54 or 72 MHz).

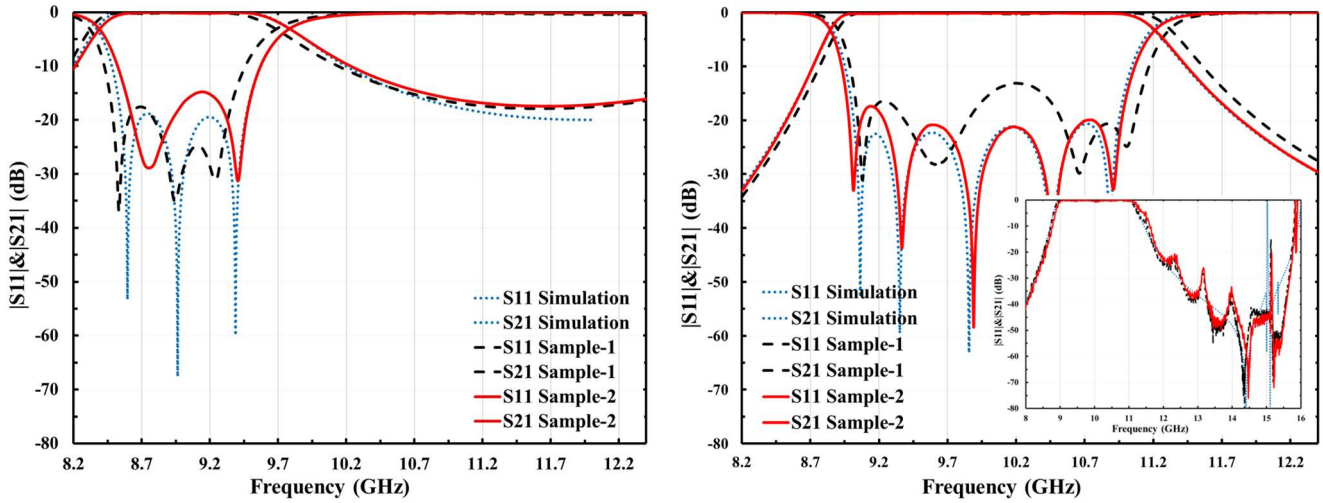

Figure 7.20 Measured and simulated results of all three examples. (a) Third-order filter with polarization rotation. (b) Fifth-order filter.

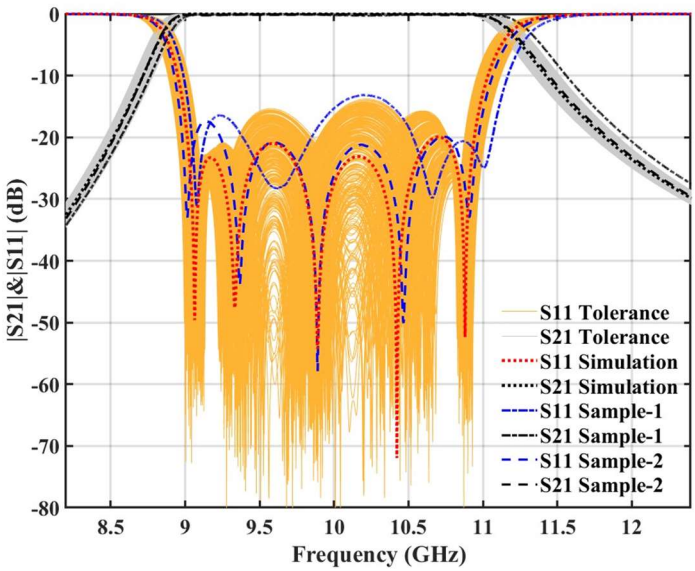

Figure 7.21 Sensitivity analysis of the fifth-order filter based on pole-generating resonant iris.

To further investigate the reproducibility of the resonant iris structure using AM fabrication solution, a tolerance sensitivity analysis is carried out. Different from conventional CNC techniques where the tolerance is related to the practical milling process, the geometric error from 3-D printing is independent from the specific milling direction. Therefore, a tolerance sensitivity analysis based on Monte Carlo sampling method [46], [47] was performed on the fifth-order resonant iris filter. Six key dimensional parameters with ±100 μm (resolution of printing) tolerance were considered. 300 simulation samples with uniformly random distributed

dimensions were taken. Figure. 7.21 shows the results of the sensitivity analysis, where the biggest frequency shift and worst return loss are 50 MHz and 15 dB, respectively. Both measurement results are within the envelope of the simulation samples. For the wideband application, we believe the 3-D printing technique is a reliable manufacture solution for the intricate pole-generating resonant iris structure.

Table 7.2 provides a comparison with published wideband filters. As can be observed, the resonant iris filter shows a wide bandwidth with competitive performance in insertion loss, out-of-band rejection, and miniaturization. The polarization rotation feature gives it more design flexibility.

7.5 Conclusion

In this chapter, the design concept of a pole-generating resonant iris has been demonstrated using rectangular waveguide filters. By introducing the capacitive and inductive discontinuity simultaneously, a transmission pole can be generated by the L-shaped iris. A circuit analysis was performed to represent the operating mechanism. The prototype filters have demonstrated the capability of realizing a wider bandwidth of 20% while maintaining a compact footprint due to the miniature resonant iris. Improved out-of-band performance has also been shown. The polarization rotation feature has been shown in a 3rd-order filter. The major challenge associated with the resonant iris is its intricate structure and the almost inseparable feature from the cavity resonator, which makes it difficult to control the coupling. An approach to control and extract the coupling has been proposed. An intuitive design procedure was presented. The implementation of the filters is facilitated by 3-D printing technique. Very importantly, this allows the asymmetric coupling on either side of the resonant iris by using the tapered iris structure. The Q_u of the resonant iris is lower than traditional waveguide resonator, but in the wideband application this has limited impact on the insertion loss. All three filters were printed monolithically using SLM process. Excellent agreements between the simulated and measured results were achieved, which verifies the resonant iris concept, the design and manufacturing approach. The pole-generating resonant iris structure is not limited to rectangular waveguides and may be used for miniaturization or wideband applications. 3-D printing has proved to be a capable fabrication method for the resonant iris structures. Future work is expected on the design of more complex RF components, benefiting from the proposed resonant iris structure and the 3-D printing technique. The circuit synthesis method will be further developed.

Table 7.2 A Comparison with Some Wideband Filters

Ref.	Resonator Type	f_c (GHz)	FBW (%)	Average In-band Insertion loss (dB)	Spurious-free window (Rejection > 20dB)	Size (λ is the wavelength at the centre frequency f_c)	Number of Separate Blocks	Manufacture Technology
[1]	Multiple-mode cavity resonator	3.3	31	0.5	1.5 × f_c	(0.5×0.5×0.6)λ	4	CNC
[2]	Single-mode dielectric resonator	3.9	13	0.14	1.5 × f_c	(0.4×0.2×0.2)λ	9	CNC
[6]	Single-mode waveguide resonator	32.2	13.6	0.36	N/A	(0.8×0.4×6.4)λ	1	3-D Printing
[9]	Multiple-mode cavity resonator	25	20	0.67	1.76 × f_c	(1.8×1.8×1.3)λ	2	3-D Printing
[18]	Single-mode resonant iris resonator	29.9	13	1	1.4 × f_c	(0.9×0.4×6.3)λ	N/A	CNC
[19]	Single-mode resonant aperture resonator	7.6	19	0.19	1.6 × f_c	(0.6×2.0×5.2)λ	2	CNC
[33]	Single-mode pole-generating iris resonator	9	10	0.15	1.5 × f_c	(0.7×0.3×1.8)λ	1	3-D Printing
T.W.	Single-mode pole-generating iris resonator	10	20	0.17	1.5 × f_c	(0.8×0.3×2.4)λ	1	3-D Printing

Ref: reference, f_c: central frequency, FBW: fractional bandwidth; CNC: computer numerical control; T. W.: this work.

Reference

[1] S. Wong, S. Feng, L. Zhu, and Q.-X. Chu, "Triple- and Quadruple-Mode Wideband Bandpass Filter Using Simple Perturbation in Single Metal Cavity," *IEEE Trans. Microw. Theory Tech.*, vol. 63, no. 10, pp. 3416–3424, Oct. 2015.

[2] J. Jiang and R. R. Mansour, "Wideband dielectric substrate-loaded cavity filter," *IEEE Trans. Microw. Theory Tech.*, vol. 68, no. 1, pp. 111–120, 2020.

[3] B. Theron, S. Vigneron, and H. Baudrand, "A Two-Step Synthesis of Broadband Ridged Waveguide Bandpass Filters with Improved Performances," *IEEE Trans. Microw. Theory Tech.*, vol. 39, no. 12, pp. 2192–2197, 1991.

[4] Q. Zhang and Y. Lu, "Dimensional synthesis of symmetric wideband waveguide cross-coupled filters without global full-wave optimization," *IEEE Trans. Microw. Theory Tech.*, vol. 58, no. 12 PART 1, pp. 3742–3748, 2010.

[5] Z. Li, P. Zhao, and K. L. Wu, "An I/O coupling multiplier circuit and its application to wideband filters and diplexers," *IEEE Trans. Components, Packag. Manuf. Technol.*, vol. 8, no. 5, pp. 858–866, 2018.

[6] J. Li, C. Guo, J. Xu, and L. Mao, "Lightweight low-cost Ka-band 3-D printed slotted rectangular waveguide bandpass filters," *2017 IEEE Antennas Propag. Soc. Int. Symp. Proc.*, vol. 2017-Janua, pp. 2647–2648, 2017.

[7] C. Tomassoni, M. Dionigi, and R. Sorrentino, "Strategies for the improvement of the out of band behavior of TM dual-mode filters," *2015 IEEE 1st Int. Forum Res. Technol. Soc. Ind. RTSI 2015 - Proc.*, pp. 90–93, 2015.

[8] S. F. Feng, S. W. Wong, L. Zhu, and Q. X. Chu, "A Triple-mode Wideband Bandpass Filter Using Single Rectangular Waveguide Cavity," *IEEE Microw. Wirel. Components Lett.*, vol. 27, no. 2, pp. 117–119, 2017.

[9] P. Vaitukaitis, K. Nai, J. Rao, M. S. Bakr, and J. Hong, "Technological Investigation of Metal 3D Printed Microwave Cavity Filters Based on Different Topologies and Materials," *IEEE Trans. Components, Packag. Manuf. Technol.*, pp. 1–1, 2022.

[10] I. C. Hunter, L. Billonet, B. Jarry, and P. Guillon, "Microwave filters - Applications and technology," *IEEE Trans. Microw. Theory Tech.*, vol. 50, no. 3, pp. 794–805, 2002.

[11] T. S. Chen, "Characteristics of Waveguide Resonant-Iris Filters," *IEEE Trans. Microw. Theory Tech.*, vol. 15, no. 4, pp. 260–262, Apr. 1967.

[12] M. Piloni, R. Ravenelli, and M. Guglielmi, "Resonant aperture filters in rectangular waveguide," in *1999 IEEE MTT-S International Microwave Symposium Digest (Cat. No.99CH36282)*, 1999, vol. 3, pp. 911–914.

[13] T. S. Chen, "Waveguide Resonant-iris Filters with very Wide Passband and Stopbands," *Int. J. Electron.*, vol. 21, no. 5, pp. 401–424, 1966.

[14] U. Rosenberg, S. Amari, and F. Seyfert, "Pseudo-elliptic direct-coupled resonator filters based on transmission-zero-generating irises," *Eur. Microw. Week 2010, EuMW2010 Connect. World, Conf. Proc. - Eur. Microw. Conf. EuMC 2010*, no. September, pp. 962–965, 2010.

[15] M. Politi and A. Fossati, "Direct coupled waveguide filters with generalized Chebyshev response by resonating coupling structures," *Eur. Microw. Week 2010, EuMW2010 Connect. World, Conf. Proc. - Eur. Microw. Conf. EuMC 2010*, no. September, pp. 966–969, 2010.

[16] U. Rosenberg and S. Amari, "A Novel Band-Reject Element for Pseudoelliptic Bandstop Filters," *IEEE Trans. Microw. Theory Tech.*, vol. 55, no. 4, pp. 742–746, Apr. 2007.

[17] Y. Zhang, H. Meng, and K. L. Wu, "Direct Synthesis and Design of Dispersive Waveguide Bandpass Filters," *IEEE Trans. Microw. Theory Tech.*, vol. 68, no. 5, pp. 1678–1687, 2020.

[18] R. M. Barrio-Garrido, S. Llorente-Romano, M. Salazar-Palma, A. Oñoro-Navarro, and I. Hidalgo-Carpintero, “Design, construction and experimental characterization of a broadband highly selective filter in waveguide technology in Ka Band,” *IEEE MTT-S Int. Microw. Symp. Dig.*, pp. 250–253, 2006.
[19] J. F. Valencia Sullca, S. Cogollos, V. E. Boria, and M. Guglielmi, “Compact Dual-Band and Wideband Filters With Resonant Apertures in Rectangular Waveguide,” *IEEE Trans. Microw. Theory Tech.*, vol. 70, no. 6, pp. 3125–3140, Jun. 2022.
[20] R. Sorrentino and O. A. Peverini, “Additive manufacturing: A key enabling technology for next-generation microwave and millimeter-wave systems [point of view],” *Proc. IEEE*, vol. 104, no. 7, pp. 1362–1366, 2016.
[21] C. Tomassoni, O. A. Peverini, G. Venanzoni, G. Addamo, F. Paonessa, and G. Virone, “3D Printing of Microwave and Millimeter-Wave Filters: Additive Manufacturing Technologies Applied in the Development of High-Performance Filters with Novel Topologies,” *IEEE Microw. Mag.*, vol. 21, no. 6, pp. 24–45, Jun. 2020.
[22] P. Booth, J. Gilmore, E. V. Lluch, and M. Harvey, “Enhancements to satellite feed chain performance, testing and lead-times using additive manufacturing,” *2016 10th Eur. Conf. Antennas Propagation, EuCAP 2016*, 2016.
[23] P. Martin-Iglesias, M. Van Der Vorst, J. Gumpinger, and T. Ghidini, “ESA’s recent developments in the field of 3D-printed RF/microwave hardware,” *2017 11th Eur. Conf. Antennas Propagation, EUCAP 2017*, pp. 553–557, 2017.
[24] C. Guo, J. Li, X. Shang, M. J. Lancaster, and J. Xu, “Progress on microwave devices fabricated using stereolithography 3-D printing technique,” *2017 Int. Appl. Comput. Electromagn. Soc. Symp. China, ACES-China 2017*, no. 2, pp. 2–3, 2017.
[25] M. Salek, X. Shang, and M. J. Lancaster, “Compact S-Band Coaxial Cavity Resonator Filter Fabricated by 3-D Printing,” *IEEE Microw. Wirel. Components Lett.*, vol. 29, no. 6, pp. 382–384, 2019.
[26] P. Vaitukaitis, K. Nai, J. Rao, and J. Hong, “On the Development of Metal 3D Printed Bandpass Filter With Wide Stopband Based on Deformed Elliptical Cavity Resonator With an Additional Plate,” *IEEE Access*, vol. PP, pp. 1–1, 2022.
[27] P. Booth and E. V. Lluch, “Enhancing the Performance of Waveguide Filters Using Additive Manufacturing,” *Proc. IEEE*, vol. 105, no. 4, pp. 613–619, 2016.
[28] O. A. Peverini *et al.*, “Integration of an H -Plane Bend, a Twist, and a Filter in Ku/K-Band Through Additive Manufacturing,” *IEEE Trans. Microw. Theory Tech.*, vol. 66, no. 5, pp. 2210–2219, 2018.
[29] P. Booth, R. Roberts, M. Szymkiewicz, and C. Hartwanger, “Using additive manufacturing for feed chain and other passive microwave components,” *2017 11th Eur. Conf. Antennas Propagation, EUCAP 2017*, pp. 558–562, 2017.
[30] C. Guo *et al.*, “A 3-D Printed E-Plane Waveguide Magic-T Using Air-Filled Coax-to-Waveguide Transitions,” *IEEE Trans. Microw. Theory Tech.*, vol. 67, no. 12, pp. 4984–4994, 2019.
[31] L. Qian *et al.*, “Thermal Stability Analysis of 3D Printed Resonators Using Novel Materials,” in *2021 51st European Microwave Conference (EuMC)*, 2022, no. April, pp. 334–337.
[32] X. Wen *et al.*, “An Invar Alloy SLM Printed Diplexer with High Thermal Stability,” *IEEE Trans. Circuits Syst. II Express Briefs*, vol. PP, no. c, pp. 1–1, 2021.
[33] L. Qian, R. Martinez, M. Salek, M. Attallah, Y. Wang, and M. J. Lancaster, “Compact Monolithic SLM 3D-Printed Filters using Pole-Generating Resonant Irises,” in *2021 51st European Microwave Conference (EuMC)*, 2022, no. April, pp. 118–121.
[34] C. Lopez, V. Desmaris, D. Meledin, A. Pavolotsky, and V. Belitsky, “Design and Implementation of a Compact 90° Waveguide Twist with Machining Tolerant Layout,” *IEEE Microw. Wirel. Components Lett.*, vol. 30, no. 8, pp. 741–744, 2020.

[35] L. Zeng, C. E. Tong, S. N. Paine, and P. K. Grimes, “A Compact Machinable 90° Waveguide Twist for Broadband Applications,” *IEEE Trans. Microw. Theory Tech.*, vol. 68, no. 7, pp. 2515–2520, 2020.
[36] J. Q. Ding, Y. Zhao, and S. C. Shi, “A Full WR-3 Band and Low-Loss 90° Waveguide Twist Based on CNC,” *IEEE Trans. Terahertz Sci. Technol.*, vol. 10, no. 1, pp. 93–96, 2020.
[37] G. Barué, *Microwave Engineering*. Hoboken, NJ, USA: John Wiley & Sons, Inc., 2008.
[38] G. Macchiarella, G. G. Gentili, C. Tomassoni, S. Bastioli, and R. V. Snyder, “Design of Waveguide Filters with Cascaded Singlets through a Synthesis-Based Approach,” *IEEE Trans. Microw. Theory Tech.*, vol. 68, no. 6, pp. 2308–2319, 2020.
[39] G. Macchiarella *et al.*, “Accurate Modeling of Stubs Used as Resonant Coupling Elements in SIW Filters,” *IEEE Microw. Wirel. Components Lett.*, vol. 30, no. 12, pp. 1125–1128, 2020.
[40] J.-S. Hong and M. J. Lancaster, *Microstrip Filters for RF/Microwave Applications*. New York, USA: John Wiley & Sons, Inc., 2001.
[41] M. Dishal, “Design of Dissipative Band-Pass Filters Producing Desired Exact Amplitude-Frequency Characteristics,” *Proc. IRE*, vol. 37, no. 9, pp. 1050–1069, Sep. 1949.
[42] A. C. Guyette, I. C. Hunter, and R. D. Pollard, “The design of microwave bandpass filters using resonators with nonuniform Q,” *IEEE Trans. Microw. Theory Tech.*, vol. 54, no. 11, pp. 3914–3921, 2006.
[43] Jiasheng Hong, J. NI, and M.-I. Petronilo, “A radio frequency pass-band filter,” WO2020057722A1, 2018.
[44] A. M. Howatson, P. G. Lund, and J. D. Todd, *Engineering Tables and Data*. Dordrecht: Springer Netherlands, 1972.
[45] E. Hammerstad and O. Jensen, “Accurate Models for Microstrip Computer-Aided Design.,” *IEEE MTT-S Int. Microw. Symp. Dig.*, vol. 1, no. 12, pp. 107–409, 1980.
[46] Z. Zhang, H. Chen, Y. Yu, F. Jiang, and Q. S. Cheng, “Yield-Constrained Optimization Design Using Polynomial Chaos for Microwave Filters,” *IEEE Access*, vol. 9, pp. 22408–22416, 2021.
[47] X. Wen *et al.*, “SLM Printed Waveguide Dual-Mode Filters with Reduced Sensitivity to Fabrication Imperfections,” *IEEE Microw. Wirel. Components Lett.*, vol. 31, no. 11, pp. 1195–1198, 2021.

CHAPTER 8: 3-D PRINTED MONOLITHIC DIELECTRIC WAVEGUIDE FILTER USING LCM TECHNIQUE

Lu Qian, Emelia Hayward, Milan Salek, Zhifu Liu, Jorma Vihinen, Yi Wang

Yi Wang suggested this work, planned, and supervised the entire study, and led the project. Lu Qian conceived the idea of this design and carried out the theoretical modelling and numerical simulations, and performed the experiment, interpreted the data and wrote the manuscript. Jorma Vihinen assisted in the fabrication of the experimental sample. Zhifu Liu advised on the coating process. All authors contributed to the writing of the paper and reviewed the manuscript.

This chapter is based on the following publication: 3-D Printed Monolithic Dielectric Waveguide Filter Using LCM Technique, which has been published in 2022 IEEE MTT-S International Microwave Workshop Series on Advanced Materials and Processes for RF and THz Applications (IMWS-AMP), 2022, pp. 1–3. Doi: 10.1109/IMWS-AMP54652.2022.10106895.

Abstract

A 3-D printed monolithic dielectric waveguide filter is presented in this chapter. The proposed filter is constructed by a single piece of 3D printed dielectric puck with silver plated outer surface. To facilitate the fabrication of the monolithic dielectric filter, a lithography-based ceramic 3-D printing technology is employed. In this way, the mould required in conventional ceramic forming technologies is eliminated and the higher design freedom can be obtained. The detailed manufacturing parameters and post-processing methods are described. To demonstrate feasibility of the proposed solution, one prototype filter operating at 11.5 GHz with 850 MHz bandwidth is designed, fabricated, and measured. The measurement result shows reasonable agreement with the simulation.

Keywords: Additive Manufacturing (AM), 3D-printed dielectric filter, dielectric ceramic, dielectric waveguide filter, monolithic dielectric filter

8.1 Introduction

Dielectric resonator filters are a class of widely employed microwave components in wireless communication systems because of their excellent performance in terms of miniature and power-handling capacity. Since the dielectric resonator was first introduced in microwave filter design, enormous advances have been achieved in the design and fabrication of the microwave dielectric filter [1], [2]. Depending on the structure and the assembly approach of dielectric resonators, dielectric filters can be categorized as two types: (i) dielectric-loaded filters, and (ii) monolithic dielectric filters. The former usually comprises dielectric pucks, mounting fixture and metallic housing. However, the extra support structures and adhesive materials may cause degradation in insertion loss and thermal stability. Monolithic dielectric filters are constructed by a dielectric puck with a metal coated surface. Compared with the dielectric loaded filter, this family of filters offers advantages in terms of the reduction in volume and weight. However, the fabrication of the filters is challenging. Special mould is often required to manufacture the dielectric puck, which is only cost-effective for large scale production and the practical design freedom is usually limited. On the other hand, binding and soldering separate dielectric blocks together requires high assembling accuracy. A minor misalignment could lead to considerable degradation in filter performance.

Additive manufacturing, also referred to as 3-D printing, has started to change the ways that microwave components are designed and fabricated. Polymer and metal-based 3-D printed microwave components have been reported [3], [4]. Advances in ceramic 3-D printing, a current trend in 3-D printing technology, have motivated researchers to apply it to microwave component design and fabrication. Some 3-D printed dielectric resonator filters were reported in [5], [6]. Manufacturing issues such as limited geometry freedom and misalignment can be alleviated to some extent. However, most of them are dielectric-loaded filter, operating in TE mode and still require custom-made metallic enclosures. Recently, 3-D printed monolithic dielectric filters operating in TM mode were reported [7], [8], where the whole filter is printed off a single piece of dielectric puck. The outer surface of the dielectric block is metallized to mimic the short-circuited contact between the dielectric resonator and metallic housing. In this way, the metallic housing can be eliminated. Compared to TM mode dielectric filters, dielectric waveguide filters can achieve further reduction of filter volume and weight. However, there is little reported work on 3-D printed dielectric waveguide filters. To fully leverage the unique free-form fabrication capability of 3-D printing and to explore the new solution for the dielectric filters, a 3-D printed monolithic dielectric waveguide filter has been designed and implemented.

In this work, the Lithography based Ceramic Manufacturing (LCM) technique [9] was used to fabricate the dielectric waveguide filter. Unlike the common stereolithography (SLA) technology, LCM is a mask-based SLA method, in which an integral image is projected to the photopolymerisable slurry surface through a special optical system. This system includes an LED light source and a digital micromirror device array. Because of the ultra-fast light switching and integral projection, LCM technology moves away from the conventional point-line-layer scanning process. Hence, the printing time can be reduced dramatically, and better feature resolution can be obtained [10].

8.2 Monolithic Dielectric Waveguide Filter

A fourth-order dielectric waveguide filter is presented. It is centred at 11.5 GHz with a specified passband return loss of 20 dB and equal ripple bandwidth (BW) of 850 MHz. The normalized non-zero coupling coefficients m_{ij} and the external quality factor Q_{ex} are calculated to be $m_{12} = m_{34} = 0.9105$, $m_{23} = 0.6999$, $Q_{ex} = 12.68$. These design parameters can be converted to the practical filter structure by following the standard dimensioning procedure.

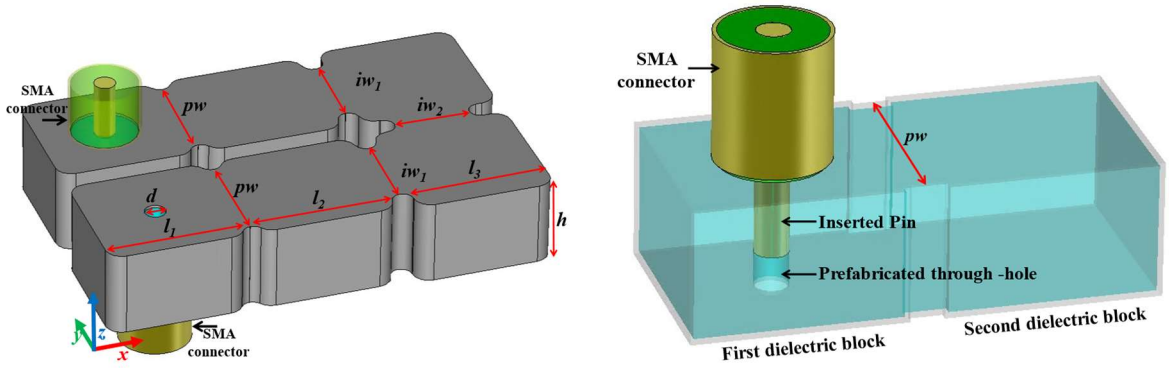

(a) (b)

Figure 8.1 (a) Illustration of a fourth-order dielectric waveguide filter; (b) 3-D perspective view of the input/output coupling structure.

Figure. 8.1 presents the configuration of the dielectric waveguide filter, where six rectangular dielectric blocks are cascaded. The external surface of the dielectric block is fully covered by silver. Two SMA connectors located on the top and bottom surfaces are input/output ports. Figure. 8.1(b) shows the perspective view of the feeding ports. Unlike the common feeding structures, the first dielectric block and the standard SMA connector work as the coaxial to dielectric waveguide adapter. The length of the inserted pin is fixed for ease of assembly. The external coupling strength is controlled by the width of the inductive coupling window *pw*. The TE_{101} mode in the second block is used as the first resonator. The inter-resonator coupling is realized by the inductive coupling window. Also, the round chamfer of 0.5 mm in radius is added to each upright edge of the dielectric filter model to reduce the stress accumulated at sharp corners/edges during heat treatment after printing.

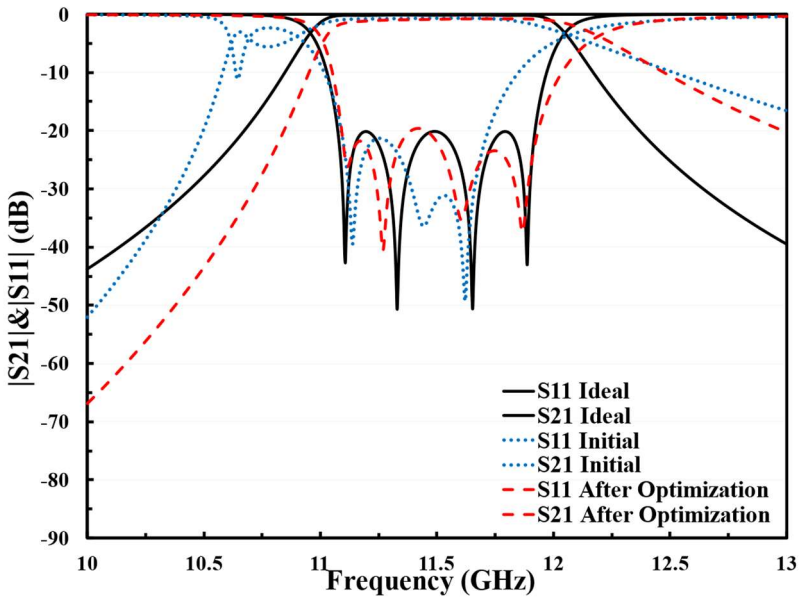

Figure 8.2 Comparison between simulated filter responses and the ideal response.

Figure. 8.2 shows the simulated filter responses in comparison with the ideal response from the coupling matrix. As can be observed, the initial response from physical dimensioning is close to the ideal response while the response after optimization agrees well with the ideal response over the passband. The slight frequency shift and the discrepancy in out-of-band rejection are due to the higher-order spurious modes.

8.3 Fabrication

8.3.1 3-D Printing

To produce the dielectric waveguide filter, LCM technology was used. LCM is a slurry-based photopolymerization ceramic 3-D printing process. The chosen ceramic slurry is the LithaLox HP500 alumina ceramic. Its solid loading and dynamic viscosity are 49% and ~12 Pa·s at room temperature, respectively. The employed printer is the Lithoz CeraFab 7500 system. It has a maximum building envelope of 76 mm × 43 mm × 150 mm, and the nominal lateral pixel size is 40 μm. The layer thickness in printing is 25 μm.

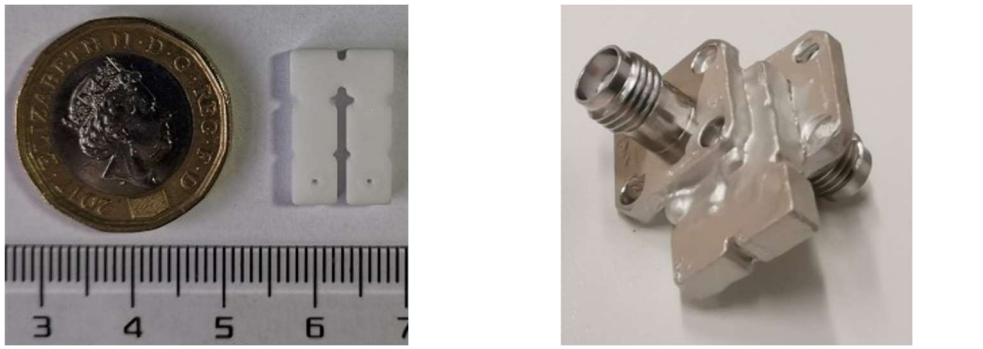

(a) (b)

Figure 8.3 Photograph of the 3-D printed dielectric waveguide filter: (a) Dielectric block after sintering; (b) Dielectric waveguide filter after silver plating with assembled SMA connectors.

The manufacturing cycle can be split into two main steps: printing the green body and thermal post-processing. In the first step, the filter model was printed in a layer-by-layer fashion along the *Z*-axis (see Figure. 8.1(a)). No support structures are required. After printing, the green body of filter was constructed, mainly composed of weakly bound ceramic materials. Next, two thermal post-processing steps (debinding and sintering) were applied to the as-printed green body with the purpose of removing the polymer binder and achieving densification. The debinding process is the most time-consuming and critical stage since the binder and other pyrolyzed organic substances needs to be slowly removed to prevent cracking. Finally, the binder-removed sample was sintered to achieve adequate material density. The printing model needs to be scaled up to pre-compensate the shrinkage caused by thermal processes. According to previous experience, the shrinkage coefficient can be found to be 24.5% in *XY*-plane and 27.5% in *Z*-axis for the used alumina ceramic. Figure. 8.3(a) shows a photograph of the as-sintered dielectric puck. At this point, the dielectric component should achieve the desired electrical properties of $\varepsilon_r = 9.9$ and $\tan\delta = 0.0018$.

Table 8.1 Comparison Between the Measured and Designed Dimensions

Dimensions	Designed (mm)	Measured (mm)	Discrepancy (+/-%)
l_1	4.79	4.84	+1.0%
l_2	4.79	4.83	+0.8%
l_3	4.98	5.07	+1.8%
pw	3.84	3.80	-1.0%
iw_1	3.05	3.00	-1.6%
iw_2	2.68	2.76	+3.0%
h	3	3.10	+3.3%
d	0.8	0.73/0.94	-8.8%/+17.5%

To evaluate the quality of the manufacture, crucial physical dimensions of the as-sintered dielectric puck (see Figure. 8.1(a)) were measured using the Vision Engineering Hawk inspection microscope. A comparison between the measured and designed dimensions is given in Table 8.1. It can be found that the average dimensional variation of the dielectric puck is around 0.04~0.1 mm. This is within the manufacturing accuracy of 0.1 mm. It should be noted there are two values given for the diameter of the prefabricated through-hole, which correspond to the diameter before/after laser processing. As the prefabricated hole is smaller than the design, a laser micromachining workstation was used to expand the prefabricated holes.

8.3.2 Metallization Process

In this work, Sunchemical C2060217P3 silver paste is used to accomplish the metallization of the dielectric waveguide filter. The nominal electrical conductivity of the selected silver paste is 2.9×10^7 *S/m*. The corresponding skin depth at 11.5 GHz can be calculated to be 0.9 μm. Therefore, the thickness of the coated layer should be at least 4.5 μm (five times of the skin depth) to ensure good surface conductivity.

During the metallization process, the as-sintered dielectric block was first cleaned using acetone and deionized water in an ultra-sonic bath to remove surface contaminants. The cleaned sample was then brushed with the silver paste and was dried using a hotplate at 130 ℃ for 15 minutes. To obtain the desired coating layer thickness, the brushing and drying cycle needed to be repeated three to five times. After that, the coated sample was fired in the laboratory furnace to remove the organic solvent and binder within the silver paste and improve the adhesion between the ceramic and coating layer. The firing process was performed at 600 ℃ with a heating rate of 3 ℃/min. The sample was kept at peak temperature for 30 minutes and cooled to room temperature naturally. Figure. 8.3(b) shows a photograph of the dielectric waveguide filter after silver plating, where two SMA connectors were assembled using RS conductive paint 186-3600.

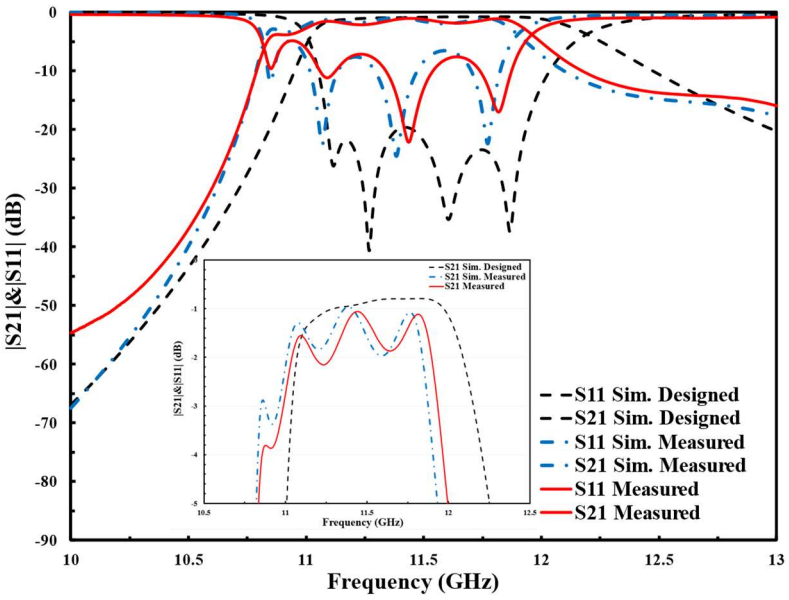

Figure 8.4 Comparison between measured filter responses and simulated results based on the designed and the measured physical dimensions, with inset showing the expanded view of S_{21} over the passband.

8.4 Measurement and Discussion

The *S*-parameter measurement results and simulated filter responses are compared in Figure. 8.4, where the two simulated results are derived from the designed and measured physical dimensions, respectively. The inset is the expanded view of S_{21} over the passband. As can be observed, the measured filter passband is shifted down by 40 MHz (0.35% of the simulated centre frequency) against the designed response. Within the passband, the average measured insertion loss is 1.98 dB, which is 1 dB higher than the simulated result. The evident discrepancy in the insertion loss is believed to be due to the degraded effective conductivity and worse-than-simulated S_{11}. From experience, the latter observation, along with the frequency shift, is mainly caused by the dimensional inaccuracy of the manufactured prototype. To verify this point, the filter was simulated again using the measured physical dimensions in Table 8.1. From Figure. 8.4, the simulated filter response based on measured dimensions shows good agreement with the measured result. The remaining difference could be attributed to assembly error, such as a gap between SMA connectors and the dielectric filter. To improve the consistency with the design, it is believed that the dimension errors can be corrected by pre-compensating the manufacture model.

8.5 Conclusion

A 3-D printed monolithic dielectric waveguide filter has been reported in this chapter. To the best of authors' knowledge, this is the first demonstrated 3-D printed monolithic dielectric waveguide filter. The complete design and manufacturing process was illustrated. A filter prototype was fabricated using LCM ceramic 3-D printing technology. Detailed manufacturing parameters and post-processing methods were presented. The discrepancy between the measurement results and simulation results were discussed. The feasibility of manufacturing the monolithic dielectric waveguide filter using LCM technology is verified. An end-to-end manufacturing approach was demonstrated. This work opens new opportunities for the design and fabrication of dielectric resonator filters. Future work is expected to focus on improving the manufacturing accuracy through pre-compensation and implementing more complex microwave components.

Reference

[1] M. Memarian and R. R. Mansour, "Quad-mode and dual-mode dielectric resonator filters," *IEEE Trans. Microw. Theory Tech.*, vol. 57, no. 12, pp. 3418–3426, Dec. 2009.

[2] Y. Jang, J. Kim, S. Kim, and K. Lee, "Design and fabrication of a compact 3-dimensional stacked type dielectric ceramic waveguide bandpass filter," *IEEE Microw. Wirel. Components Lett.*, vol. 24, no. 10, pp. 665–667, 2014.

[3] C. Guo, J. Li, X. Shang, M. J. Lancaster, and J. Xu, "Progress on microwave devices fabricated using stereolithography 3-D printing technique," *2017 Int. Appl. Comput. Electromagn. Soc. Symp. China, ACES-China 2017*, no. 2, pp. 2–3, 2017.

[4] L. Qian *et al.*, "A Narrowband 3-D Printed Invar Spherical Dual-Mode Filter With High Thermal Stability for OMUXs," *IEEE Trans. Microw. Theory Tech.*, vol. 70, no. 4, pp. 2165–2173, Apr. 2022.

[5] Y. Marchives, N. Delhote, S. Verdeyme, and P. M. Iglesias, "Wide-band dielectric filter at C-band manufactured by stereolithography," *Eur. Microw. Week 2014 Connect. Futur. EuMW 2014 - Conf. Proceedings; EuMC 2014 44th Eur. Microw. Conf.*, pp. 187–190, 2014.

[6] A. Perigaud, O. Tantot, N. Delhote, S. Verdeyme, S. Bila, and D. Baillargeat, "Bandpass Filter Based on Skeleton-like Monobloc Dielectric Pucks Made by Additive Manufacturing," *2018 48th Eur.*

Microw. Conf. EuMC 2018, pp. 296–299, 2018.
[7] C. Carceller, F. Gentili, D. Reichartzeder, W. Bösch, and M. Schwentenwein, “Development of monoblock TM dielectric resonator filters with additive manufacturing,” *IET Microwaves, Antennas Propag.*, vol. 11, no. 14, pp. 1992–1996, Nov. 2017.
[8] D. Miek *et al.*, “Ceramic Additive Manufactured Monolithic X-Shaped TM Dual-Mode Filter,” *IEEE J. Microwaves*, vol. 2, no. 3, pp. 496–506, 2022.
[9] U. K. F. M. R. W. Homaw. Längle, “Light-curing ceramic slips for the stereolithographic preparation of high-strength ceramics,” US9403726B2, 2014.
[10] Z. Chen *et al.*, “3D printing of ceramics: A review,” *J. Eur. Ceram. Soc.*, vol. 39, no. 4, pp. 661–687, 2019.

CHAPTER 9: CONCLUSIONS AND FUTURE WORK

9.1 Conclusions

This thesis addresses the challenges in the design and implementation of high-power microwave filters through the combination of AM technology and novel materials. It proposes solutions to the thermal-induced frequency detuning problems and innovative filter structures.

In Chapter 3, a fourth-order 0.47% bandwidth spherical dual-mode filter designed for OMUX has been reported. To the best of our knowledge, this is the first demonstrated narrowband filter additively manufactured from Invar alloy in the open literature. This work demonstrates the possibility of using complex resonator structures in Invar filter design (without being limited to the rectangular and cylindrical cavities), and opens more design opportunities for optimal RF, mechanical and thermal properties for narrowband filters. The improvement in the thermal stability demonstrates the capability of the 3-D printed Invar filter. The end-to-end manufacturing methods and the detailed experimental investigation have been discussed. The design concept, manufacturing parameters, and material characterization may find useful applications in the design of future high-power filters.

In Chapter 4, the measurement results of the Invar spherical filter introduced in Chapter 3 after further post-processing is discussed. It also investigates the effect of different surface treatment techniques through a spherical Invar resonator. It is found that compared to the mechanical polishing method, such as vibratory grinding, the electrochemical Hirtisation® process reduces surface roughness more effectively without aggressively altering the internal fine features. The thermal stability of the filter under high-power operation is demonstrated through Multiphysics simulation. The power breakdown threshold is analysed using SPARK3D, revealing that this filter can provide a robust design margin against the specified power requirements. The 3D printed Invar components discussed here offer a promising alternative for high-power microwave applications.

In Chapter 5, the thermal stability of microwave cavity resonators, additively manufactured using several alloy materials with low CTE, is evaluated. Ti64, Zr702 and TNTZ show much improved temperature stability compared with aluminium. Most temperature-dependent RF measurement results show good correlation with the CTE properties of the materials. The TNTZ sample did not reach the lowest CTE reported in the literature. The work also demonstrated the printability of monolithic and irregular shaped resonators using these new materials. This increases the range of materials that may be used for microwave filter and opens opportunity for new temperature compensation mechanism for high power filters.

In Chapter 6, a lightweight, high-Q and high temperature stability spherical resonator manufactured from HB-Cesic® composite has been reported. To the best of authors' knowledge, this is the first SiC-ceramic-based microwave resonator reported in the open literature. The material properties and end-to-end manufacturing approach are described. Detailed experimental characterization and verification have been performed. The causes for the frequency discrepancy and spurious spikes have been analysed. The former is mainly caused by spherical radius variation whereas the latter is due to the discontinuity introduced by the assembly errors and the glue line. It is expected these spurious modes can be mitigated by optimising the manufacture process, increasing assemble accuracy and choosing appropriate bonding plane. The advantage of the HB-Cesic® resonators in Qu and weight reduction have been demonstrated. Both resonators achieved the Qu of over 10000 and 60% mass reduction, while achieving comparable thermal stability to Invar resonator. This work confirms the feasibility of using HB-Cesic® in microwave resonators and provide a new technology for highly thermal-stable microwave devices, paving the way for further development and verification programme for more complex passive microwave devices such as filters and multiplexers for space applications.

In Chapter 7, the design concept of a pole-generating resonant iris has been demonstrated using rectangular waveguide filters. By introducing the capacitive and inductive discontinuity simultaneously, a transmission pole is generated by the L-shaped iris. A circuit analysis was performed to represent the operating mechanism. The prototype filters have demonstrated the capability of realizing a wider bandwidth of 20% while maintaining a compact footprint due to the miniature resonant iris. Improved out-of-band performance has also been shown. The polarization rotation feature has been shown in a 3rd-order filter. The major challenge associated with the resonant iris is its intricate structure and the almost inseparable feature from the cavity resonator, which makes it difficult to control the coupling. An approach to control and extract the coupling has been proposed. An intuitive design procedure was presented. The implementation of the filters is facilitated by 3-D printing technique. Very importantly, this allows the asymmetric coupling on either side of the resonant iris by using the tapered iris structure. The Qu of the resonant iris is lower than traditional waveguide resonator, but in the wideband application this has limited impact on the insertion loss. All three filters were printed monolithically using SLM process. Excellent agreements between the simulated and measured results were achieved, which verifies the resonant iris concept, the design and manufacturing approach. The pole-generating resonant iris structure is not limited to rectangular waveguides and may be used for miniaturization or wideband applications. 3-D printing has proved to be a capable fabrication method for the resonant iris structures.

Finally, in Chapter 8, a 3-D printed monolithic dielectric waveguide filter has been reported. To the best of authors' knowledge, this is the first demonstrated 3-D printed monolithic dielectric waveguide filter. The complete design and manufacturing process was illustrated. A filter prototype was fabricated using LCM ceramic 3-D printing technology. Detailed manufacturing parameters and post-processing methods were presented. The discrepancy between the measurement results and simulation results were discussed. The feasibility of manufacturing the monolithic dielectric waveguide filter using LCM technology is verified. An end-to-end manufacturing approach was demonstrated. This work opens new opportunities for the design and fabrication of dielectric resonator filters.

9.2 Future Work

Possible future work based on what has been presented in this thesis is given as follows:

(1) Improvement for High-Power Filters in terms of PIM Interference and High-Power Breakdown.

In Chapters 3, 4 and 5, we have presented a viable end-to-end fabrication solution made possible by AM technology and novel low CTE materials. Several high-power microwave filters with enhanced thermal stability have been proposed, leveraging weight reduction features and optimized thermal management. Future research could help further harness the advantages of advanced manufacturing techniques to address other two power-limiting factors: PIM interference and high-power breakdown. To mitigate PIM interference, the development of a monolithic RF front module integrated with the multiplexer and antenna feeding system could be a promising solution. For the high-power breakdown concerns, the potential of using 3D printing techniques to improve the breakdown threshold may be investigated.

(2) Novel Resonator Structures and Filter Configurations

In Chapter 6, we introduced a pole-generating resonant iris and designed compact monolithic waveguide wideband filters with Chebyshev responses. The proposed resonator iris is equivalent to a singlet, generating a zero-pole pair. Future work will focus on designing filters with more complex quasi-elliptic or elliptic filtering responses using the proposed resonant iris structure. Additionally, more novel resonator structures and filter topologies may be explored through the proposed end-to-end fabrication solutions.

(3) Reliable Ceramic 3D Printing for Microwave Components

Chapter 7 showcased a monolithic dielectric waveguide filter based on LCM ceramic 3D printing technology. However, a noticeable deterioration was observed in the manufactured filter prototype, primarily

attributed to manufacturing tolerance and assembly errors. Future work will concentrate on establishing a more reliable end-to-end manufacturing solution for microwave dielectric filters. Potential approaches include (1) manufacturing iterations and pre-compensation, (2) exploration of other high-precision ceramic 3D printing techniques, and (3) the design of novel dielectric filter structures with reduced sensitivity to manufacturing and assembly tolerance.